Fermilab

FERMILAB-THESIS-1998-62

INAUGURAL-DISSERTATION
zur
Erlangung der Doktorwürde
der
Naturwissenschaftlich-Mathematischen Gesamtfakultät
der
Ruprecht-Karls-Universität
Heidelberg

vorgelegt von

Dipl.-Phys. Ivo Eschrich

aus Bonn

Tag der mündlichen Prüfung: 3. Juni 1998

Measurement of the Σ^- Charge Radius at the Fermilab Hyperon Beam

Gutachter: Prof. Dr. Bogdan Povh
Prof. Dr. Klaus Tittel

Zusammenfassung

Messung des Σ^--Ladungsradius am Hyperonenstrahl des Fermilab.
Der Σ^--Ladungsradius wurde im Rahmen des SELEX (E781) Experimentes durch elastische Streuung von Σ^--Teilchen an Hüllenelektronen bestimmt.
Dabei stand dem Experiment am Fermilab ein 600 GeV/c Σ^-/π^--Strahl zur Verfügung. Das Spektrometer verfügte über Detektoren zur präzisen Spurrekonstruktion und Teilchenidentifikation über einen weiten Impulsbereich. Ein spezieller Trigger für elastische Hadron-Elektron-Streuung wurde entwickelt und in den SELEX Trigger integriert.
Aus den 1997 aufgezeichneten Daten wurden 12000 elastische Σ^--Elektron Streuereignisse isoliert und für die vorliegende Analyse verwendet.
Der lorentzinvariante quadratische Impulsübertrag Q^2 wurde aus dem Strahlimpuls und dem Elektronenstreuwinkel berechnet. Durch Anpassung des differentiellen Wirkungsquerschnittes für elastische Streuung von Σ^- am Elektron an die Verteilung der gemessenen Q^2 wurde der mittlere quadratische Ladungsradius zu $\langle r^2 \rangle = 0.60 \pm 0.08\,(stat.) \pm 0.08\,(syst.)\,\mathrm{fm}^2$ bestimmt.

Abstract

Measurement of the Σ^- Charge Radius at the Fermilab Hyperon Beam.
The Σ^- charge radius was measured in the framework of the SELEX (E781) experiment by scattering Σ^- elastically off atomic electrons.
The experiment at Fermilab utilized a 600 GeV/c Σ^-/π^- beam. The spectrometer was equipped with devices for high-precision tracking and particle identification covering a wide momentum range. A special trigger for hadron-electron elastic scattering was developed and integrated into the SELEX trigger.
Using the 1997 data, a sample of 12,000 Σ^- -electron elastic scattering events was obtained and used in this analysis.
The four-momentum transfer squared Q^2 was calculated from the beam momentum and the electron scattering angle. Fitting the differential cross section for Σ^--electron elastic scattering to the measured Q^2 distribution yielded a mean squared charge radius of $\langle r^2 \rangle = 0.60 \pm 0.08\,(stat.) \pm 0.08\,(syst.)\,\mathrm{fm}^2$.

Contents

1 Introduction **3**

2 Theoretical Basis **5**

2.1 Radii of hadrons 5

2.1.1 Charge vs. strong interaction radii 5

2.1.2 Direct measurements of charge radii 8

2.1.3 The direct measurement at SELEX 9

2.2 Σ^--electron elastic scattering 10

2.2.1 Kinematics 10

2.2.2 The differential cross section 13

2.2.3 Form factors and the charge radius 15

3 The SELEX Experiment **19**

3.1 Physics goals 19

3.1.1 Charm physics 20

3.1.2 Beam physics 21

3.2 Setup 26

3.2.1 The hyperon beam 31

3.2.2 Tracking 32

3.2.3 Particle identification 38

3.2.4 Trigger elements 44

4 The Trigger **45**

4.1 Trigger and data acquisition concepts 45

4.2 The hadron-electron scattering trigger 47

4.2.1 Implementation history 48

4.2.2 Performance 51

4.2.3 Background 52

4.3 The interaction counter 57

5 Data Analysis **63**
5.1 Expected event rates 63
5.2 Data reduction 65
5.2.1 Strip 1 65
5.2.2 Strip 2 67
5.2.3 Strip 3 69
5.3 Analysis of the filtered sample 70
5.3.1 Final cuts 70
5.3.2 Radius fits 76
5.3.3 Resolution and acceptance studies 79
5.3.4 Statistical and systematic errors 87

6 Results and Discussion **93**
6.1 The Σ^- charge radius 93
6.2 Discussion 96
6.2.1 Comparison to other hadrons and theoretical predictions . . 96
6.2.2 Possibilities for improvement 99

7 Conclusion **101**

Bibliography **107**

Contributions to the experiment **113**

The SELEX collaboration **114**

Acknowledgements **115**

1

Introduction

Hadrons as we understand them today are composite systems which consist of quarks and gluons. One characterizes hadrons by their static properties such as mass, charge, spin, and magnetic moment which describe the composite system as a whole. For example, the charge is the sum of the fractional charges of the constituent quarks. The rest mass reflects the energy stored in the system. The one static property which reflects the phenomenon unique to hadrons – quark confinement – is the size of the particle.

How can the size of a hadron be defined? It depends on the process employed to measure it. Since quark confinement is not fully understood, the definition of a strong interaction radius is model-dependent. Besides, being a feature of the strong interaction, confinement itself may be affected by a strong-interaction measurement process. The electromagnetic interaction, on the other hand, is well understood and provides an unambiguous definition of a hadron's size by means of its charge radius, analogous to the nuclear charge radius.

Unfortunately, charge radii are known only for five different hadrons so far – for proton, neutron, π^-, K^-, and K^0. The fact that the K^- radius has been found to be smaller than that of the π^- suggests that the size of a hadron is related to the flavor composition of its constituent quarks. There is supporting evidence from a recent study of strong interaction radii [1] which finds that replacing an *up* or *down* quark by a *strange* quark decreases the radius by a constant value. Consequently the Σ^- radius should be smaller than the proton radius, and larger than the Ξ^-.

The charge radius can be measured by scattering electrons elastically off the hadrons. The distribution of scattering angles reflects the charge distribution. In other words, one measures the differential cross section for the process of scattering the pointlike electron off the hadron. The departure from the differential cross

section for scattering the electron off a pointlike particle yields the radius. This kind of experiment has been pioneered by Hofstadter more than 40 years ago at SLAC[1] [2]. It requires the hadron to be stable, which is true only for the proton. For unstable hadrons one reverses the process and scatters the hadron off atomic electrons. A beam of the hadron in question has to be produced, with sufficient energy to extend the hadron's lifetime in the laboratory system so that the scattering process can be reconstructed, and sufficient intensity to provide the statistics necessary for a meaningful measurement.

Only two high-energy high-intensity hyperon beam facilities exist today, one at CERN[2] [3] and one at Fermilab[3] [4]. The WA89 experiment at CERN has demonstrated that a measurement of the Σ^- charge radius by Σ^--electron scattering is feasible [5].

The objective of the investigation presented here was to make use of the high-intensity hyperon beam at Fermilab in the framework of the SELEX (E781) experiment to determine the Σ^- charge radius.

In the following chapters a summary of the information available on charge radii is given and the theoretical groundwork of the measurement summarized. The SELEX experiment and the special trigger used to obtain the Σ^--electron elastic scattering data are described in chapters 3 and 4. Finally, a report on the analysis of the data and a first result for the Σ^- charge radius is presented.

[1] Stanford Linear Accelerator Center, Stanford, CA, U.S.A.
[2] Conseil Européen pour la Recherche Nucléaire, Geneva, Switzerland
[3] Fermi National Accelerator Laboratory, Batavia, IL, U.S.A.

2

Theoretical Basis

2.1 Radii of hadrons

2.1.1 Charge vs. strong interaction radii

A hadron's radius can be defined in different ways, depending on what probe is used to measure it. Elastic electron–hadron scattering yields the mean squared charge radius $\langle r^2 \rangle$. The theory of this process is well-established [6] and can be summarized as follows:

The electromagnetic interaction between electron and hadron can be described as function of the four-momentum transfer squared Q^2 by the differential elastic scattering cross section:

$$\frac{d\sigma}{dQ^2} = \frac{4\pi\alpha^2\hbar^2}{Q^4}\left(1 - \frac{Q^2}{Q^2_{max}}\right) \cdot F^2(Q^2). \tag{2.1}$$

All information about the spatial extent of the hadron as seen by the electron is contained in the form factor $F(Q^2)$. Assuming a spherically symmetric charge distribution of the form $z \cdot \rho(r)$ where z is the charge and $\rho(r)$ a normalized probability density, the mean squared charge radius is defined as

$$\langle r^2 \rangle = \int r^2 \rho(r) d^3r. \tag{2.2}$$

For spin-0 hadrons it can be extracted from the derivative of the form factor $F(Q^2)$ extrapolated to zero momentum transfer:

$$\langle r^2 \rangle \equiv -6\hbar^2 \frac{dF(Q^2)}{dQ^2}\bigg|_{Q^2=0}. \tag{2.3}$$

For hadrons with non-zero spin the above equation describes a radius which also incorporates contributions from the interaction of the electron with the magnetic

moment of the hadron. In this case the form factor $F(Q^2)$ is considered a combination of two form factors which describe the electric and magnetic contributions separately (refer to section 2.2.3 for a more detailed description).

Elastic hadron–proton scattering, on the other hand, should be related to a radius which reflects strong interactions as well. However, there is no general agreement on the definition of this kind of radius. Strong interaction radii are therefore always model-dependent and their significance is less clear as compared to charge radii which are well-defined and can be measured directly [7, 8].

Charge radii have been measured only for five different hadrons so far (Table 2.1; also Table 2.2 on page 8). Total elastic hadron–proton scattering cross sections, on the other hand, are available for a number of particles. A recent study of strong interaction radii used an empirical linear relation between the total cross section for hadron–proton scattering and the strong interaction radius at fixed center-of-mass energy [9]:

$$\langle r^2 \rangle^{(st)}_{hadron} = \langle r^2 \rangle^{(st)}_{proton} \cdot \frac{\sigma^{tot}_{hadron-proton}}{\sigma^{tot}_{proton-proton}} \tag{2.4}$$

The results are listed in Table 2.1 ("strong radius"). The values for charged hadrons are indeed very close to the charge radii, where available.

The most important feature to be noted is the flavor dependence of the radius: $\langle r^2 \rangle^{(st)}$ decreases in steps of approximately 0.08 fm^2 for every strange valence quark. This is true for the chains

$$p(\mathtt{uud}) \rightarrow \Lambda(\mathtt{uds}), \Sigma^-(\mathtt{dds}) \rightarrow \Xi^-(\mathtt{dss})$$

as well as for $\pi^- \rightarrow K^-$ (zero to one strange quark) and $\rho \rightarrow \phi$ (zero to two strange quarks).

Most theoretical models do not yield this strong flavor dependence (Table 2.1). The non-relativistic quark model, however, can reproduce the systematics if a correction [1]

$$\Delta^{(st)} = \frac{1}{n} \sum_{q=1}^{n} \frac{\xi}{m_q^2} \tag{2.5}$$

is applied to the mean squared strong interaction radius, where ξ is constant, n is the number of constituent quarks, and m_q the mass of the quark. For the mean squared charge radius this correction is weighted with the quarks' charge e_q:

$$\Delta = \sum_{q=1}^{n} e_q \frac{\xi}{m_q^2} \tag{2.6}$$

Table 2.1: Measured charge radii $\langle r^2 \rangle$ in fm^2 for different hadrons (*cf.* Table 2.2) compared to strong interaction radii [1] and predictions for charge radii from various models.

	experimental results		theoretical predictions						
	charge radius	strong radius	non-rel. quark[a]	VDM [b]	rel. bag [c]	Skyrme [10]	Skyrme [11]	CCDM [12][d]	Soliton [13]
p	0.67 ± 0.02	0.67 ± 0.02	0.67	0.40	0.53	0.775	1.20	0.663	0.78
p	0.74 ± 0.02[e]								
n	-0.11 ± 0.03					-0.308	-0.15	-0.081	-0.09
Σ^+		0.58 ± 0.02	0.73			0.964	1.20	0.707	0.79
Λ		0.58 ± 0.02	0.33	0.49	0.55	0.107	-0.06	0.082	-0.04
Σ^-	0.9 ± 0.7	0.58 ± 0.02	0.55	0.34	0.49	0.751	1.21	0.543	0.75
Ξ^-		0.50 ± 0.02	0.45	0.29	0.46	0.261	1.21	0.352	0.72
Ω^-			0.33		0.51	0.147		0.74	
π^-	0.44 ± 0.01	0.41 ± 0.02	0.54	0.40	0.24				
K^-	0.34 ± 0.05	0.35 ± 0.02	0.44						
K^0	-0.054 ± 0.026		-0.09	-0.09	-0.011				

[a] calculated with the procedure described in [7], normalized to proton radius of 0.67 fm^2.

[b] Vector dominance model, values taken from [1]

[c] Relativistic bag model, values taken from [1]

[d] SU(3) Chiral color dielectric model

[e] for different Q^2 range, *cf.* Table 2.2.

The most recent predictions for charge radii of strange hadrons have been compiled in Table 2.1. There is little agreement among the different models.

2.1.2 Direct measurements of charge radii

Table 2.2: Experimental values of hadronic charge radii.

hadron	Q^2 [GeV$^2/c^2$]	$\langle r^2 \rangle$ [fm^2]	exp. method
p	$0.003 - 0.06$	0.74 ± 0.02	direct e-p scattering [14]
	$0.006 - 0.12$	0.67 ± 0.02	direct e-p scattering [15, 16]
		0.79 ± 0.03	Lamb shift [17]
n	≈ 0	-0.113 ± 0.003	inverse n-e scattering [18]
Σ^-	$0.01 - 0.09$	0.9 ± 0.7	inverse Σ^- e scattering [5]
π^-	$0.015 - 0.25$	0.44 ± 0.01	inverse π^- e scattering [19]
K^-	$0.017 - 0.095$	0.34 ± 0.05	inverse K^-e scattering [20]
K^0	$0 - 6$	-0.054 ± 0.026	coherent K regeneration, K^0e scattering [21]

The proton radius has been measured to good precision by elastic scattering of an electron beam off a liquid hydrogen target [2, 15, 16, 22, 14]. The proton radius can also be determined from the nuclear correction to the Lamb shift for the hydrogen $1S$ ground state which has been measured to very high precision [17]. However, there is a considerable discrepancy between the results of different experiments (Table 2.2).

The neutron radius can be extracted from electron–deuteron scattering in a similar fashion. However, the necessary corrections require good knowledge of the deuteron wavefunction. Measurements by inverse scattering of neutrons on atomic electrons have been more successful [23, 18].

For all other unstable hadrons inverse scattering is the only way to measure the charge radius directly. The minimal requirement is a beam of the particle in question, a suitable target, and appropriate experimental setup for particle identification and tracking with good angular and momentum resolution.

The pion radius has been measured by three generations of inverse scattering experiments with π^- beams of 50 GeV/c (at Serpukhov 1974 [24]), 100 and 250 GeV/c (Fermilab 1977 and 1980 [25, 26]), and 300 GeV/c (CERN 1984 [19]). The latter two of these experiments were also able to establish values for the K^- charge radius [27, 20] by making use of their beam's kaon contamination. All

of them used a liquid hydrogen target as the best compromise between electron density and radiation length.

A first attempt at a measurement of the Σ^- radius has been performed in 1994 by the WA89 experiment at CERN [5, 28]. A 330 GeV/c beam containing approximately 66% π^-, 33% Σ^-, and 1% Ξ^- was used in conjunction with a solid target consisting of copper and diamond foils adding up to 4.4% of an interaction length. In spite of its considerable statistical error the WA89 result of $\langle r^2 \rangle = (0.9 \pm 0.7)\,\mathrm{fm}^2$ demonstrates that a determination of the Σ^- charge radius with a solid target is feasible.

2.1.3 The direct measurement at SELEX

SELEX used a 600 GeV/c beam consisting of equal parts of Σ^- and π^-, as well as Ξ^- at the order of 2%. At this beam momentum the geometrical acceptance allowed a Q^2 range which had its lower limit at 0.015 GeV$^2/c^2$ and extended to 0.21 GeV$^2/c^2$ for Σ^- and Ξ^-, and to 0.6 GeV$^2/c^2$ for π^-. The Σ^- decay length amounted to 21 meters in the lab system.

A combination of copper/diamond targets was used, a modification of the WA89 target totaling 5% of an interaction length. The higher beam energy combined with full particle identification and a beam intensity 100 times that of WA89 provided the possibility to extract the Σ^- radius with significantly improved statistics.

The strategy was to use a dedicated trigger for preselection of elastic scattering candidates, and high-precision tracking combined with full particle identification to permit reconstruction of all variables needed for extracting the radius in the offline analysis.

SELEX has taken data with positive beam as well, which contained mainly protons, and Σ^+ at the order of one percent.

2.2 Σ^--electron elastic scattering

2.2.1 Kinematics

The kinematics of Σ^--electron elastic scattering in the laboratory frame are given by the Σ^- beam particle which interacts with an electron at rest. Let the four-momenta of the incoming Σ^-, electron at rest, scattered Σ^-, and recoil electron be

$$p_\Sigma = (E_\Sigma, \vec{p}_\Sigma) \qquad p_e = (m_e, \vec{0}) \tag{2.7}$$

$$p'_\Sigma = (E'_\Sigma, \vec{p}_\Sigma{}') \qquad p'_e = (E_e{}', \vec{p}_e{}') \tag{2.8}$$

The scattering angles θ_Σ, θ_e are defined with respect to the direction of the beam particle (Fig. 2.1).

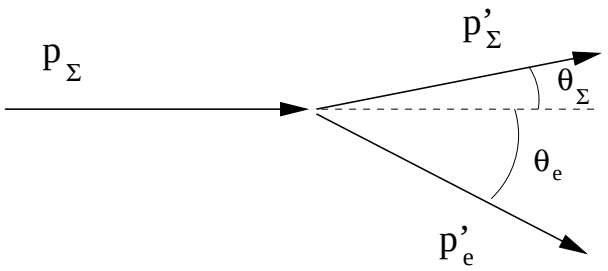

Figure 2.1: Kinematics of Σ^--electron elastic scattering

The four-momentum transfer squared is defined as

$$Q^2 = -(p_\Sigma - p'_\Sigma)^2 = -(p'_e - p_e)^2. \tag{2.9}$$

Four-momentum is conserved:

$$p_\Sigma + p_e = p'_\Sigma + p'_e. \tag{2.10}$$

Eqn. (2.10) squared yields

$$p_\Sigma \cdot p_e = p'_\Sigma \cdot p'_e \tag{2.11}$$

Using equation (2.10) one of the parameters in (2.11) can be eliminated to extract the scattering angles (Fig. 2.2):

$$\cos\theta_\Sigma = \frac{E'_\Sigma(m_e + E_\Sigma) - m_e E_\Sigma - m_\Sigma^2}{|\vec{p}_\Sigma||\vec{p}_\Sigma{}'|} \tag{2.12}$$

$$\cos\theta_e = \frac{E_e{}'(m_e + E_\Sigma) - m_e E_\Sigma - m_e^2}{|\vec{p}_\Sigma||\vec{p}_e{}'|} \tag{2.13}$$

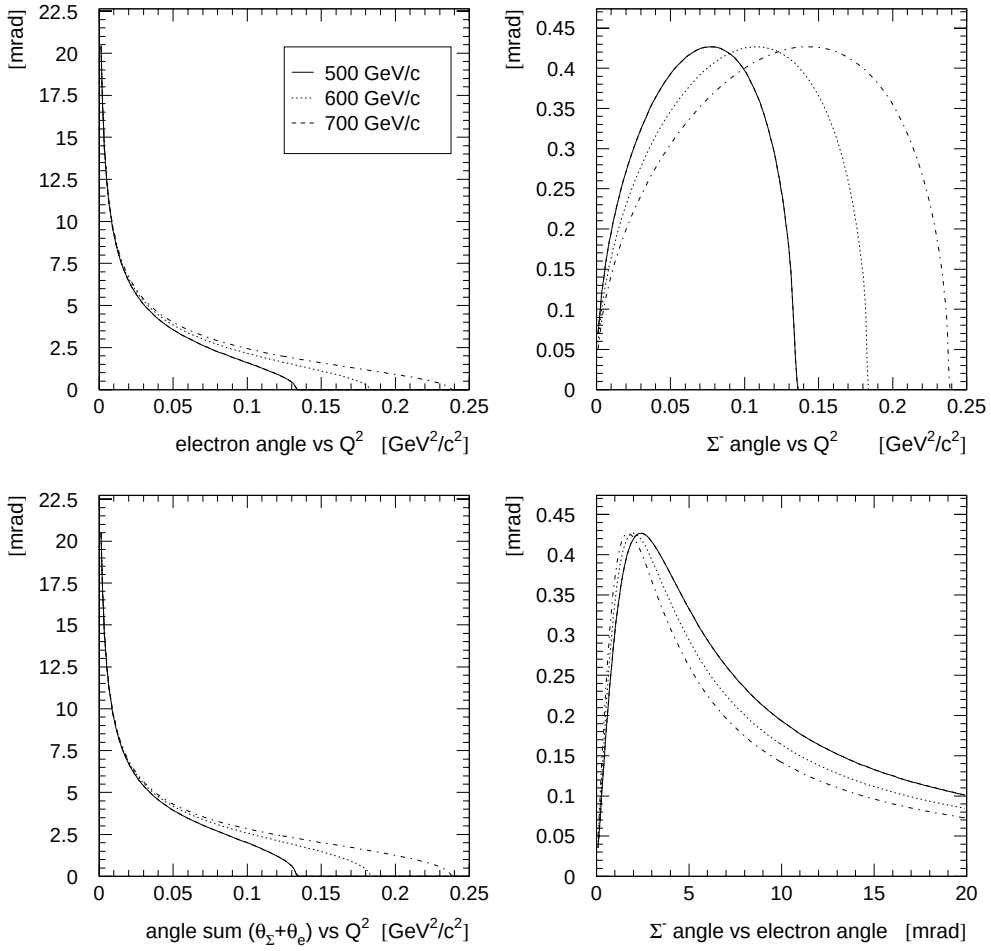

Figure 2.2: Kinematic relations for Σ^--electron scattering at 500, 600, and 700 GeV/c beam momentum.

The four-momentum transfer Q^2 can be obtained in four different ways:

1. From the scattered electron's momentum:

$$Q^2 = 2m_e(E_e{}' - m_e) \approx 2m_e E_e{}'. \tag{2.14}$$

2. From the electron scattering angle:

$$Q^2 = \frac{2E_\Sigma |\vec{p}_e{}'| m_e \cos\theta_e}{E_\Sigma + m_e}. \tag{2.15}$$

3. From beam and scattered Σ^- energy:

$$Q^2 = 2m_e(E_\Sigma - E'_\Sigma). \tag{2.16}$$

4. From the Σ^- scattering angle:

$$Q^2 = \frac{2|\vec{p}_\Sigma| m_e \cdot (|\vec{p}_\Sigma| - |\vec{p}_\Sigma{}'| \cos\theta_\Sigma)}{E_\Sigma + m_e}. \tag{2.17}$$

Q^2 has a maximum given by the beam energy. Consider the center of mass (CM) energy in the lab frame

$$s = (p_e + p_\Sigma)^2 = m_e^2 + m_\Sigma^2 + 2m_e E_\Sigma \approx m_\Sigma^2 + 2m_e E_\Sigma \tag{2.18}$$

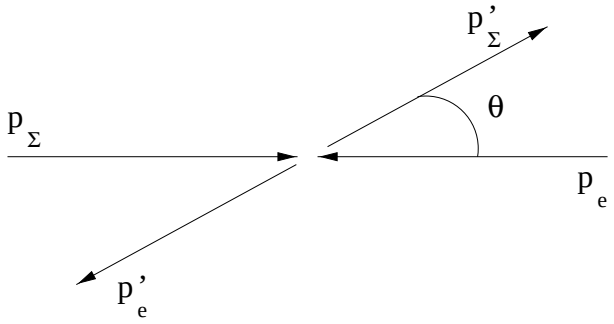

Figure 2.3: Σ^--electron scattering in the center of mass system.

The CM energy in the center of mass frame for a head-on collision ($\theta = 180°$) can be written as

$$s = (p_e + p_\Sigma)^2 \approx m_\Sigma^2 + 2|\vec{p}_e| \left(\sqrt{m_\Sigma^2 + \vec{p}_e{}^2} + |\vec{p}_e| \right) \tag{2.19}$$

where $\vec{p}_e = -\vec{p}_\Sigma$. Then the four-momentum transfer squared is given by

$$t = -Q^2 = (p_e - p'_e)^2 \approx -2\vec{p}_e{}^2(1 - \cos\theta). \tag{2.20}$$

Its maximum in terms of CM energy,

$$Q^2_{max} = -t_{min} = \frac{(s - m^2_\Sigma)^2}{s}, \tag{2.21}$$

yields in the lab frame

$$Q^2_{max} = \frac{4m^2_e E^2_\Sigma}{m^2_\Sigma + 2m_e E_\Sigma} \tag{2.22}$$

Table 2.3 lists Q^2_{max} for different SELEX beam particles at 650 GeV/c .

Table 2.3: SELEX beam particles and their Q^2_{max} at 650 GeV/c

Beam particle	Q^2_{max} [GeV$^2/c^2$]
π^-	0.645
Σ^-	0.210
Ξ^-	0.183
Ω^-	0.127
p	0.286
Σ^+	0.212

2.2.2 The differential cross section

The scattering of electrons on nucleons, or the scattering of pointlike spin-$\frac{1}{2}$ particles on fermions of finite size in general is described by the Rosenbluth equation [29]. For electron-Σ^- scattering in the laboratory frame one obtains

$$\begin{aligned}\frac{d\sigma}{d\Omega} =& \frac{\alpha^2}{4E^2_\Sigma} \cdot \frac{\cos^4(\theta/2)}{\sin^4(\theta/2)} \cdot \frac{1}{1 + (2E_\Sigma/m_\Sigma)\sin^2(\theta/2)} \\ & \cdot \left[\left(F_1^2 + \frac{Q^2}{4m^2_\Sigma}\kappa^2 F_2^2 \right) + \frac{Q^2}{2m^2_\Sigma} \tan^2\frac{\theta}{2} (F_1 + \kappa F_2)^2 \right].\end{aligned} \tag{2.23}$$

Σ^--electron scattering can be regarded as the same process with reversed kinematics [30]. The Rosenbluth equation can be written in Lorentz invariant form as a function of $t = -Q^2$ [31]:

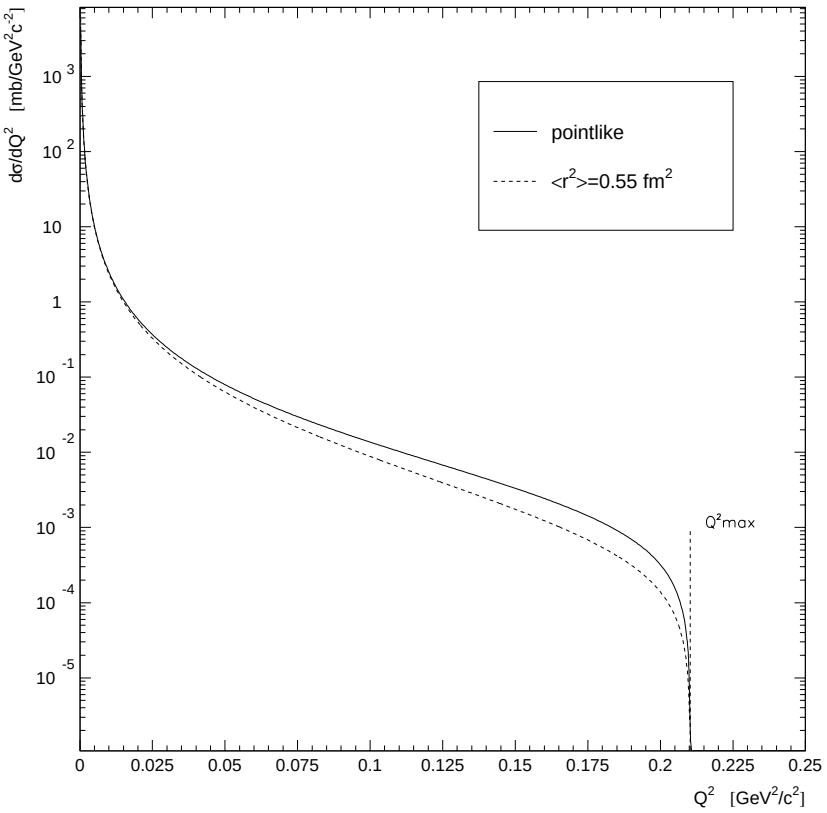

Figure 2.4: Differential cross section for Σ^- -electron elastic scattering at 650 GeV/c beam momentum and a mean square charge radius of 0.55 fm^2 compared to the cross section for a pointlike Σ^- .

$$\frac{d\sigma}{dt} = \frac{4\pi\alpha^2\hbar^2}{t^2(s-m_\Sigma^2)^2}\left[st+(s-m_\Sigma^2)^2\right] \cdot \left[F_1^2 - \frac{t}{4m_\Sigma^2}\kappa^2F_2^2 + \frac{t^2}{2(st+(s-m_\Sigma^2)^2)}\cdot(F_1+\kappa F_2)^2\right]. \quad (2.24)$$

Here, m_Σ is the beam particle mass, κ the anomalous magnetic moment, F_1 and F_2 are both functions of Q^2, and $s = m_e^2 + m_\Sigma^2 + 2E_\Sigma m_\Sigma$ the center of mass energy.

Making use of $Q^2 \gg m_e^2$, $E_\Sigma \gg m_e$, and $E_\Sigma \gg m_\Sigma$ and the definition (2.22)

of Q^2_{max} the above expression can be simplified to

$$\frac{d\sigma}{dQ^2} = \frac{4\pi\alpha^2\hbar^2}{Q^4}\left(1 - \frac{Q^2}{Q^2_{max}}\right) F^2(Q^2) \tag{2.25}$$

which is the Mott cross section modified by the electromagnetic form factor squared F^2:

$$\begin{aligned} F^2 =& F_1^2 + \frac{\kappa^2 Q^2}{4m_\Sigma^2}\ F_2^2 \\ &+ \frac{\frac{1}{2}Q^4 \cdot (F_1 + \kappa F_2)^2}{(m_e^2 + 2E_\Sigma m_\Sigma)^2 - Q^2(m_e^2 + m_\Sigma^2 + 2m_e E_\Sigma)}. \end{aligned} \tag{2.26}$$

2.2.3 Form factors and the charge radius

The contributions of F_1 and F_2 in Eqn. (2.26) to F^2 can be decoupled by introducing the electric and magnetic form factors $G_E(Q^2)$ and $G_M(Q^2)$ [32],

$$G_E = F_1 - \frac{Q^2}{4m_\Sigma^2}\kappa F_2 \tag{2.27}$$

$$G_M = F_1 + \kappa F_2, \tag{2.28}$$

so that for $\kappa = 0$ G_E and G_M are identical. Now F^2 can be rewritten as

$$F^2 = G^2 + \frac{\frac{1}{2}Q^4}{(m_e^2 + 2E_\Sigma m_\Sigma)^2 - Q^2(m_e^2 + m_\Sigma^2 + 2m_e E_\Sigma)} G_M^2 \tag{2.29}$$

where

$$G^2 = \frac{G_E^2 + G_M^2 \frac{Q^2}{4m_\Sigma^2}}{1 + \frac{Q^2}{4m_\Sigma^2}} \tag{2.30}$$

$$= F_1^2 + \frac{Q^2}{4m_\Sigma^2}\kappa^2 F_2^2. \tag{2.31}$$

For proton and neutron, G_E and G_M extrapolated to $Q^2 = 0$ take on the value of the charge and magnetic moment, respectively [6].

The Q^2 dependence of the nucleon form factors is described to good approximation by a dipole fit:

$$G_E(Q^2) = \left(1 + \frac{Q^2}{\Lambda^2}\right)^{-2} \approx 1 - \frac{2Q^2}{\Lambda^2} \tag{2.32}$$

$$G_M(Q^2) = (\kappa - 1) \cdot \left(1 + \frac{Q^2}{\Lambda^2}\right)^{-2} = \mu \cdot G_E(Q^2) \tag{2.33}$$

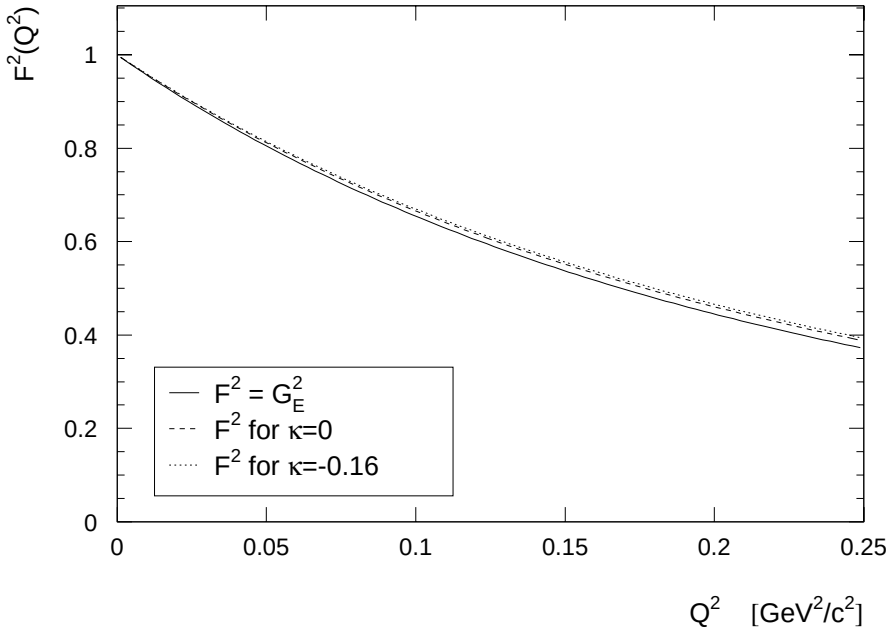

Figure 2.5: The total form factor squared for 650 GeV/c beam momentum and $\langle r^2 \rangle = 0.55\text{fm}^2$ with and without magnetic contributions compared to the electric form factor squared.

The relation $G_E = \mu G_M$ suggests to rearrange F^2 in yet another fashion to separate electric and magnetic contributions more clearly:

$$F^2 = G_E^2 \cdot \left[\frac{4m_\Sigma^2}{4m_\Sigma^2 + Q^2} + \mu^2 \left(\frac{Q^2}{4m_\Sigma^2 + Q^2} + \frac{\frac{1}{2}Q^4}{(m_e^2 + 2E_\Sigma m_\Sigma)^2 - Q^2(m_e^2 + m_\Sigma^2 + 2m_e E_\Sigma)} \right) \right] \tag{2.34}$$

The influence of the different terms on F^2 is illustrated in Fig. 2.5.

For the π^- and K^- mesons as spin 0 particles, the form factor has no magnetic contributions. It is described by a monopole fit:

$$G_E(Q^2) = \left(1 + \frac{Q^2}{\Lambda^2}\right)^{-1} \approx 1 - \frac{Q^2}{\Lambda^2} \tag{2.35}$$

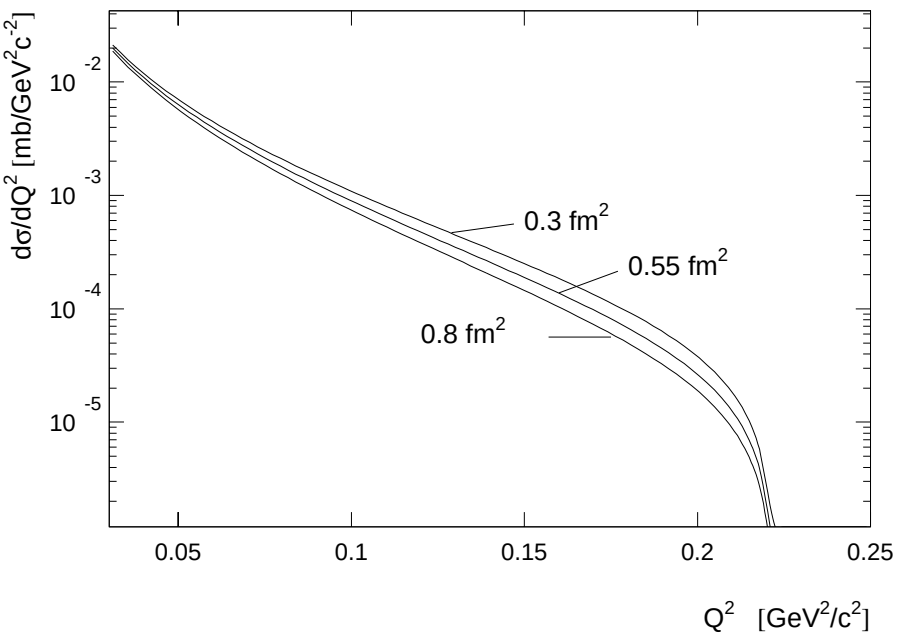

Figure 2.6: The differential cross section for assumed Σ^- mean squared radii of 0.3 fm^2, 0.55 fm^2, and 0.8 fm^2 at 650 GeV/c beam momentum.

The connection between the charge radius and the electric form factor is inherited from the definition of the nuclear radius. One assumes a spherically symmetric distribution of the charge density $C\rho(r)$, where C is the total charge and $\rho(r)$ the normalized probability density. The form factor F is interpreted as the Fourier transform of the charge distribution,

$$F = \int_{-\infty}^{\infty} \rho(r) e^{i\vec{q}\vec{r}/\hbar} d^3r, \tag{2.36}$$

where $\vec{q} = \vec{p} - \vec{p}'$ is the momentum transfer. The mean squared charge radius is defined as

$$\langle r^2 \rangle = \int_{-\infty}^{\infty} r^2 \rho(r) d^3r \tag{2.37}$$

For $\vec{q}\vec{r} \ll \hbar$ the exponential in (2.36) can be expanded:

$$\begin{aligned} F &= \int_{-\infty}^{\infty} \left(1 - \frac{(\vec{q}\vec{r})^2}{2\hbar^2} + \frac{(\vec{q}\vec{r})^4}{24\hbar^4} - \dots\right) \rho(r) d^3r \\ &= 1 - \frac{|\vec{q}|^2}{6\hbar^2} \int_{-\infty}^{\infty} r^2 \rho(r) d^3r + \int_{-\infty}^{\infty} \left(\frac{(\vec{q}\vec{r})^4}{24\hbar^4} - \dots\right) \rho(r) d^3r \\ &= 1 - \frac{|\vec{q}|^2}{6\hbar^2} \langle r^2 \rangle + \mathcal{O}(Q^4). \end{aligned} \tag{2.38}$$

The same reasoning is applied to the form factors of hadrons. Neglecting higher order terms the charge radius is extracted from the derivative of the form factor at zero momentum transfer

$$\langle r^2 \rangle = 6\hbar^2 \frac{dG_E}{dQ^2}\bigg|_{Q^2=0}, \tag{2.39}$$

i.e. the fit parameter Λ in equation (2.32) can be interpreted to reflect the charge radius:

$$\Lambda^2 = \frac{12\hbar^2}{\langle r^2 \rangle}. \tag{2.40}$$

The magnetic radius is defined accordingly:

$$\langle r^2 \rangle_M = 6\hbar^2 \frac{dG_M}{dQ^2}\bigg|_{Q^2=0}. \tag{2.41}$$

Finally, the electric and magnetic radii are related to the radii $\langle r_1^2 \rangle, \langle r_2^2 \rangle$ obtained from the Dirac and Pauli form factors F_1, F_2 by

$$\langle r^2 \rangle = \langle r_1^2 \rangle + \frac{3\kappa(\hbar c)^2}{2m_\Sigma^2} \tag{2.42}$$

$$\langle r^2 \rangle_M = \langle r_1^2 \rangle + \kappa \langle r_2^2 \rangle \tag{2.43}$$

The finite size of the hadron steepens the slope of the Mott cross section towards $Q^2 = 0$, and flattens it towards $Q^2 = Q^2_{max}$. This means: the larger the radius, the smaller is the differential cross section compared to the Mott cross section (2.25) at fixed Q^2 and fixed beam energy (Fig. 2.6).

3

The SELEX Experiment

3.1 Physics goals

SELEX (E781) (*Segmented Large x_F baryon spectrometer*) was proposed in 1986 as a third generation fixed target charm experiment [33]. WA62 as a typical representative of first generation charm experiments relied on wire chambers as tracking detectors and pioneered the Ξ_c^+ detection in 1983 [34]. WA89 as a second generation charm experiment in 1993/1994 made use of sophisticated silicon microstrip detectors to reconstruct decay vertices with high precision and thus allow lifetime measurements of the Ξ_c^+ and Ω_c^0 [35]. SELEX may be considered as the direct successor of WA89, exploiting similar techniques for precise beam and vertex tracking. The experimental regime in SELEX is extended to higher momentum of 600 GeV/c beam particles and larger statistics owing to a secondary beam rate of up to 2 MHz. The third generation approach is represented by an online charm filter capable of a rejection factor of 1:40.

SELEX intends to contribute to the understanding of hadron physics, in particular by studying the production and decay of hadrons containing charm quarks. Combining the four flavors *up*, *down*, *strange*, and *charm* to three-quark particles according to SU(4) yields a symmetric multiplet of 20 particles with spin 3/2 and a mixed multiplet of 20 baryons with spin 1/2. Figure 3.1 shows a three-dimensional scheme of this concept with the axes isospin, strangeness, and charm. SELEX concentrates on charm baryons rather than charm mesons, since large charm meson samples are already available from other experiments like E687, E791, CLEO, and E831 [37]. An important advantage of the fixed-target approach compared to collider experiments are the greater decay lengths of particles produced in forward direction. This allows a resolution on the order of picoseconds for lifetime measurements. The SELEX projects related to charm physics are presented in the following section.

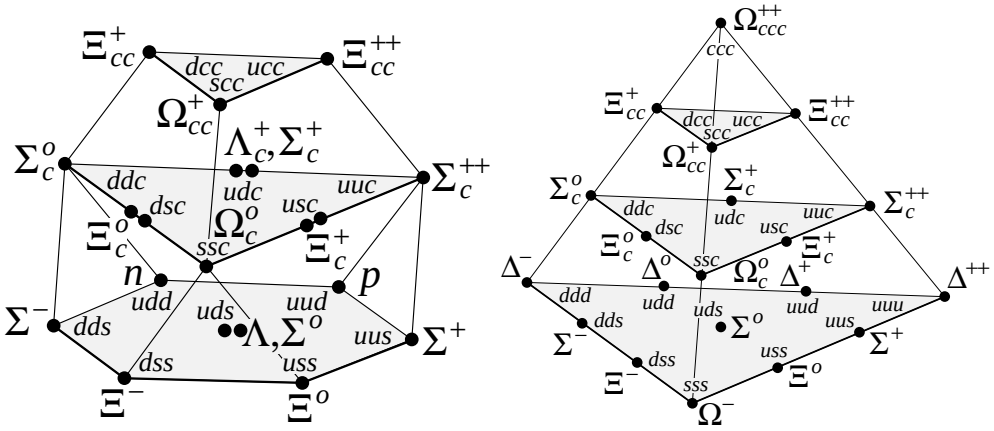

Figure 3.1: The SU(4) multiplets of baryons containing u,d,s, and c quarks for $J^P = \frac{1}{2}^+$ (left) and $J^P = \frac{3}{2}^+$ (right) [36].

Besides charm physics, SELEX hosted a number of projects which took advantage of the Σ^-/π^- content of the beam. Depending on the individual trigger requirements these projects were realized either in parallel with the charm program or during dedicated beam time periods. The respective projects will be described in section 3.1.2.

3.1.1 Charm physics

Strong production mechanisms

The strong interaction production characteristics of charm hadrons are being investigated, comparing data taken with $\pi^\pm$, p, and Σ^- beams. Comparative studies are possible over a broad kinematical region from $x_F = 0.1$ to 1.0. Beam particles with strangeness content allow further insights into the role of quark flavor overlap in the incident and produced particles. For a Σ^- beam the leading particle effect is expected to enhance the production of strange particles compared to anti-strange ones. Furthermore, a cross check with other beam particles will help to clarify the impact of the quarks' intrinsic momenta within the parton. Naively, the transverse momenta of the beam and the produced particles should be equal. Asymmetries as predicted by next-to-leading order perturbation theory and observed in collider experiments are being studied by SELEX as well [33].

Spectroscopy of charm baryons

Many of the baryons in the second level of the SU(4) multiplets have been observed, but are not well measured. In a high statistics data sample doubly-charmed baryons might be observed and their properties studied [38]. Comparison of meson and baryon spectroscopy will lead to a deeper understanding of the heavy charm quark's influence on excitation spectra, thus testing predictions of the Heavy Quark Effective Theory (HQET) [37].

Weak decay systematics

While the lifetime of the Λ_c^+ has been measured to good accuracy, the lifetimes of the three remaining weakly decaying charm strange baryons Ξ_c^+, Ξ_c^0, and Ω_c^0 are poorly measured and are especially targeted by the SELEX program. In order to understand weak decay physics in detail, the impact of the strong interaction must be reduced. Quantum Chromodynamics (QCD) effects are less prominent in semileptonic decays, which thereby constitute an important complement to lifetime measurements. Relative branching ratios of different charm baryons, normalized to their semileptonic rates, are sensitive to wave function effects in the decay [37].

3.1.2 Beam physics

Charge radii

The charge radii of beam particles (Σ^- , π^- , Ξ^- , proton, and Σ^+) can be measured by elastic scattering off target electrons, as described in chapter 2. These events were recorded using a special trigger which ran in parallel to the charm trigger (chapter 4).

Total cross sections

Hadron–proton total cross sections have been found to increase with the center-of-mass energy $\sqrt{s}$ for $\sqrt{s} > 10\,\mathrm{GeV}$ [36]. A compact description of this behavior is given by Regge theory: the total cross section can be written as

$$\sigma_{tot} = Xs^{\epsilon} + Ys^{-\eta} \tag{3.1}$$

where ϵ and η are assumed to be universal [39]. This assumption can be tested by measuring the total Σ^--p and π^--p cross sections at SELEX energies [40]. While

π^--p cross sections have been measured at comparable beam momentum, Σ^--p cross sections are known only up to 140 GeV/c [41] so far.

Instead of a liquid hydrogen target which could not be implemented in SELEX for various technical reasons, the measurement was performed on high-purity carbon and polyethylene ($(CH_2)_n$) targets. The Σ^--proton cross section can in principle be calculated by subtracting the Σ^--C from the Σ^--CH_2 cross section. This method requires very good statistics, however.

These data sets were taken in dedicated mode both with negative and positive beam. In addition, total hadron–nucleus cross sections were measured using beryllium, copper, and lead targets.

Primakoff production and hyperon resonances

The interaction of a charged particle with the Coulomb potential of a nucleus can lead to the production of a neutral meson via one-photon exchange (Primakoff effect, [42]).

$$\pi^-\gamma \to \pi^-\pi^0 \tag{3.2}$$

$$\pi^-\gamma \to \pi^-\eta \tag{3.3}$$

are typical reactions of this kind. Hyperon resonances include $\Sigma^-\gamma \to \Sigma^{-*}$, which decay to $\Sigma^{-*} \to \pi^-\Lambda$ and $\Lambda \to p\pi^-$ [43].

The Primakoff effect can also be used to study hadron polarizabilities, the chiral anomaly amplitude, exotic mesons, and radiative transistions (see below).

Pion polarizabilities and radiative transistions

Pion polarizability has been measured via radiative pion scattering in the nuclear Coulomb field [44],

$$\pi + Z \to \pi' + \gamma + Z', \tag{3.4}$$

where the incident pion Compton scatters from a virtual photon. At SELEX , virtual Compton scattering events of the type

$$\pi + e \to \pi' + e' + \gamma \tag{3.5}$$

would have passed the h-e trigger (chapter 4) and have therefore been recorded. This process is related to generalized pion polarizabilites which reduce to the Compton polarizabilities in the limit of zero momentum transfer [45].

Similarly, reactions involving radiative transitions like

$$\pi + e \to \rho + e' \tag{3.6}$$

may be observed in SELEX data. Clean data for this particular reaction would allow a determination of the $\rho \to \pi\gamma$ radiative width from the transition form factor [45].

Chiral anomaly tests

The perturbative expansion of the effective chiral Lagrangian for the $\gamma - \pi$ interaction to fourth order in momenta and masses yields a term containing abnormal intrinsic parity (also referred to as chiral axial anomaly). For the processes $\pi^0 \to 2\gamma$ and $\gamma \to 3\pi$, described by the amplitudes F_π and $F_{3\pi}$, respectively, the chiral anomaly term leads to a prediction of [46]

$$F_\pi(\mathcal{O}(p^4)) = \frac{\alpha N_c}{3\pi f} = 0.025\text{GeV}^{-1} \tag{3.7}$$

and

$$F_{3\pi}(\mathcal{O}(p^4)) = \frac{N_c\sqrt{4\pi\alpha}}{12\pi^2 f^3} \sim 9.7 \pm 0.2\text{GeV}^{-3} \tag{3.8}$$

where N_c is the number of colors in QCD and f is the charged pion decay constant. The latter amplitude can be measured via pion production by a pion in the nuclear Coulomb field:

$$\pi^- + Z \to \pi^{-\prime} + \pi^0 + Z \tag{3.9}$$

where Z is the nuclear charge. This experiment has been performed with a 40 GeV/c pion beam at Serpukhov [47] and yielded $F_{3\pi} = 12.9 \pm 0.9\ (stat.) \pm 0.5\ (syst.)$ [46]. While the prediction for F_π agrees with experiment, $F_{3\pi}$ does not. Since SELEX uses a pion beam and nuclear targets as well, this experiment could be repeated using the Primakoff trigger.

Another reaction to determine $F_{3\pi}$ is [46]

$$\pi^- + e \to \pi^{-\prime} + \pi^0 + e' \tag{3.10}$$

which has the signature of a hadron–electron elastic scattering event at the trigger level where no photon identification was included and should therefore be present in the data taken with this trigger.

Weak radiative hyperon decays

Weak and electroweak decays of hyperons can be used to probe the baryon structure with all of the nuclear forces. Topics of investigation could be the radiative transitions $\Sigma^{-\star} \to \Sigma^-\gamma$, $\Xi^{-\star} \to \Xi^-\gamma$, and the process $\Xi^- \to \Sigma^-\gamma$ [43].

Production polarization of hyperons

It has been observed that nearly all hyperons inclusively produced by proton beams are polarized at high transverse momenta p_T [48]. At SELEX , the polarization of Σ^+ and Ξ^- produced from the proton beam can be studied as a function of x_F and p_T [43].

Exotic states

The quantum numbers of the known hadrons, mesons and baryons, can be described by quark-antiquark or three-quark configurations, respectively. Hadrons for which this would not be true (exotic hadrons) may have multiquark configurations like $qq\bar{q}\bar{q}$ [49], $qqqq\bar{q}$ (pentaquarks [50]), or six-quark states (dibaryons), for example the $H(udsuds)$ [51]. They could also be hybrid systems with valence quarks and gluons ($(q\bar{q}g)$ mesons or $(qqqg)$ baryons) or glueballs, i.e. mesons consisting only of gluons $((gg), (ggg))$. They could have quantum numbers not accessible to three-quark or quark-antiquark structures (open exotic states) or even normal quantum numbers (cryptoexotic states). The latter kind could be identified only by their unusual dynamical properties like for example anomalously narrow decay widths or anomalous decay branching ratios.

The general hypothesis of "flavor antisymmetry" suggests that those quark systems which have the maximum possible antisymmetry of quark flavors are the most strongly bound, i.e. the most likely to be observed. For example, the Hexaquark H mentioned above would be expected to be the most bound dibaryon with six light quarks because not more than two quarks are in states with identical flavors. The most bound pentaquark states are expected to have the configuration $P^0(uud\bar{c}s)$ or $P^-(udd\bar{c}s)$.

One example for possible P production mechanisms, next to a one-step hadronization, is meson-baryon coalescence. Analogous to deuteron production by coalescence of a neutron and a proton a weakly bound P (i.e. with a deuteron type structure) could be produced by coalescence of a nucleon with a $D_s^-(\bar{c}s)$. Expected production cross sections have been estimated to be in the range of $\sigma(P)/\sigma(D_s^-) = 10^{-3} - 10^{-2}$ [52].

How would a P be reconstructed? The analysis would focus on decay modes where all final state particles are charged, for then the invariant mass of the system could be determined with high resolution. One signature of the pentaquark would be a peak in the invariant mass spectrum which is constant for different decay modes. A decay mode to be considered is, for example, $P \to K^+K^-\pi^-p$ [52]. SELEX is expected to have a good efficency for detecting all particles in the final state, since at large-x production the produced particles and decay fragments

are all focused in a forward cone in the laboratory system. Other requirements for background suppression like a good vertex resolution and particle identification over a large momentum range are met as well.

3.2 Setup

Three dipole magnets divided SELEX into independent spectrometers, each dedicated to one momentum region (Fig. 3.2). Each spectrometer was equipped with a combination of detectors for tracking and particle identification (Fig. 3.3).

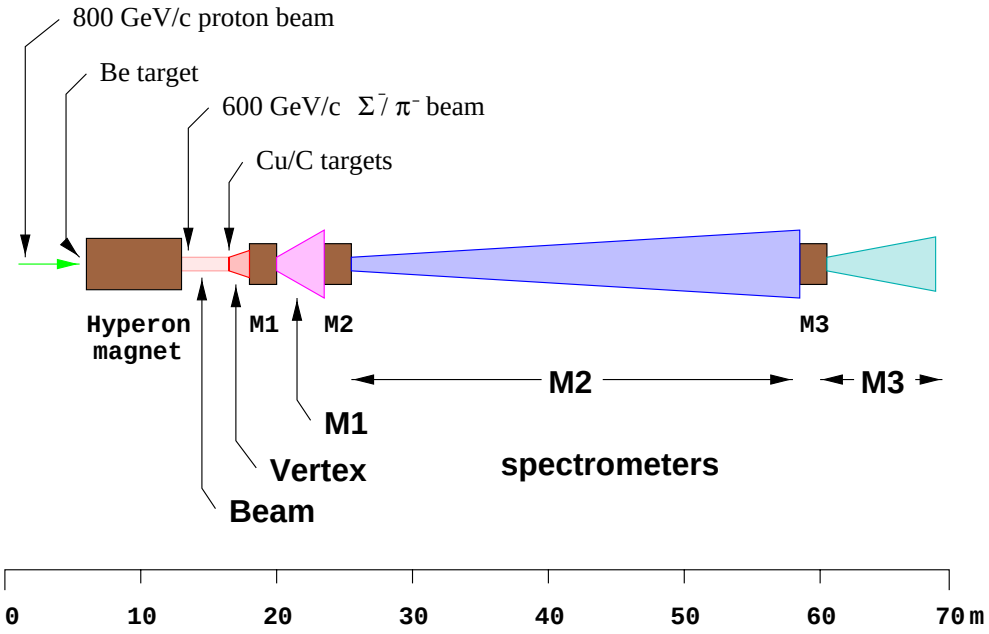

Figure 3.2: Schematic diagram of the SELEX layout. The hyperon beam runs from left to right. Four dipole magnets (`Hyperon`, `M1`, `M2`, `M3`) define five spectrometers: beam spectrometer upstream and vertex spectrometer downstream of Cu/C targets, respectively, M1 – low momentum spectrometer, M2 – high momentum spectrometer, M3 – hyperon decay spectrometer. Acceptances are indicated by shaded areas. Transverse axis is not to scale.

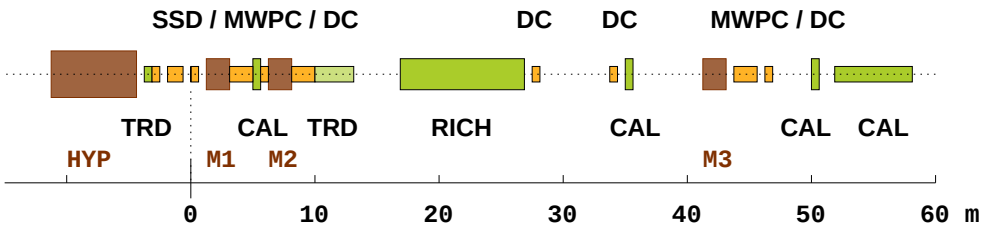

Figure 3.3: Schematic drawing of the main detector groups. Tracking was accomplished by silicon microstrip detectors (SSD), MWPCs and drift chambers (DC). Two TRDs, a RICH, three electromagnetic and one hadronic calorimeter provided particle identification.

The beam spectrometer

The section between hyperon magnet and the charm production targets was dedicated to beam definition and triggering.

After the first station of a set of three real-time silicon strip detectors – part of the hardware scatter trigger (HST) setup – the beam passed through a transition radiation detector (BTRD) which distinguished pions from baryons (Fig. 3.4).

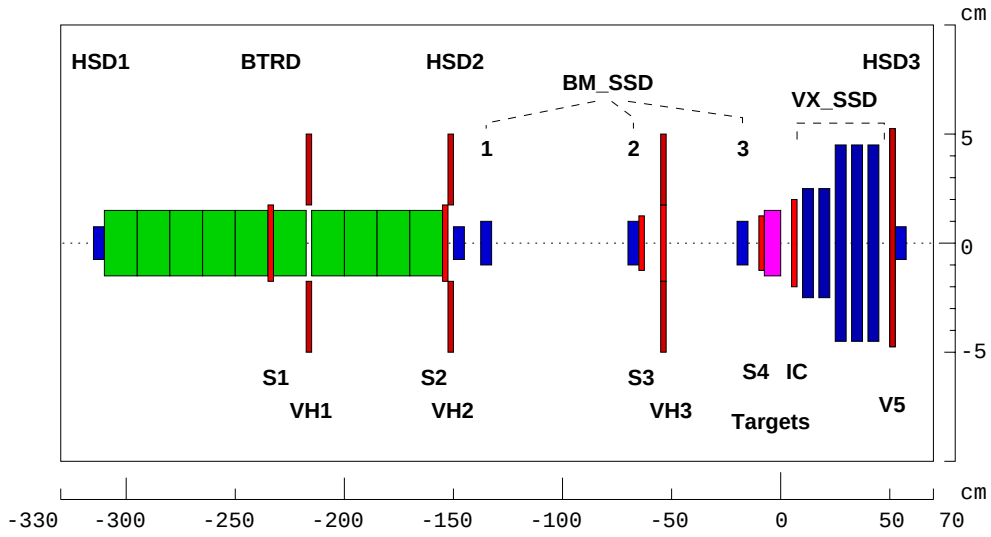

Figure 3.4: The SELEX beam and vertex spectrometer. HSD 1–3: HST silicon detectors; BTRD: beam transition radiation detector; BM_SSD, VX_SSD: beam and vertex silicon detectors; S1–S4: scintillators for beam definition; VH1–VH3: scintillators for beam halo definition.; IC: interaction counter; V5: scintillator.

Downstream of the BTRD the beam traversed the second station of HST silicon and entered the 1.94 m long RF cage which contained three stations of silicon microstrip detectors (BSSD). Together with the Hyperon magnet they provided the beam definition, i.e. both the trajectory and momentum of the beam track.

The RF cage also contained the targets. In normal running mode a set of two copper and three diamond targets totaling 4.2 % of an interaction length were used.

Table 3.1: The SELEX targets. L_{int} – interaction length, L_{rad} – radiation length.

	material	z-pos. [cm]	dimensions [cm] transverse	long.	density [g/cm^3]	L_{int} [%]	L_{rad} [%]
1	Copper	−6.08	2.54 × 2.54	0.16	8.96	1.06	11.19
2	Copper	−4.55	2.54 × 2.54	0.10	8.96	0.67	7.10
3	Diamond	−3.11	3.0 × 2.0	0.22	3.23	0.82	1.66
4	Diamond	−1.61	3.0 × 2.0	0.22	3.23	0.82	1.66
5	Diamond	−0.11	3.0 × 2.0	0.22	3.23	0.82	1.66

The vertex spectrometer

Immediately downstream of the targets an interaction counter (section 4.3) was used to make a first estimate of the charged-particle multiplicity for trigger purposes (see chapter 4). The vertex silicon detector consisted of 20 planes of silicon microstrip detectors covering an opening angle of approximately 150 mrad.

Outside the RF cage the third station of HST silicon terminated the vertex spectrometer.

The M1 spectrometer

The first dipole magnet was normally operated at 1.347 T, equivalent to a p_t kick of 0.74 GeV/c . Charged particles with less than 2.5 GeV/c momentum did not pass this magnet. The M1 spectrometer was designed to analyze particles in the 2.5 – 15 GeV/c range.

The tracking devices in this spectrometer consisted of three proportional wire counters (PWC), two drift chambers, and two stations of silicon microstrip detectors (referred to as large area silicon detectors or LASD) with 6 planes each to cover the near-beam region. These were attached to the M1 and M2 shield plates. A lead glass calorimeter provided photon identification (PHOT1, Fig. 3.5).

The M2 spectrometer

This was the fast-particle spectrometer (momentum higher than 15 GeV/c). The 1.541 T M2 magnet provided a p_t kick of 0.845 GeV/c . The magnet's end gap was covered by another LASD station (Fig. 3.5). Next to 14 MWPC planes this spectrometer also featured a 6-plane TRD for electron identification (ETRD) as well as a 10 m long RICH, followed by 10 m of decay region with two sets of drift chambers (Vee A and B) and another lead glass calorimeter for photon

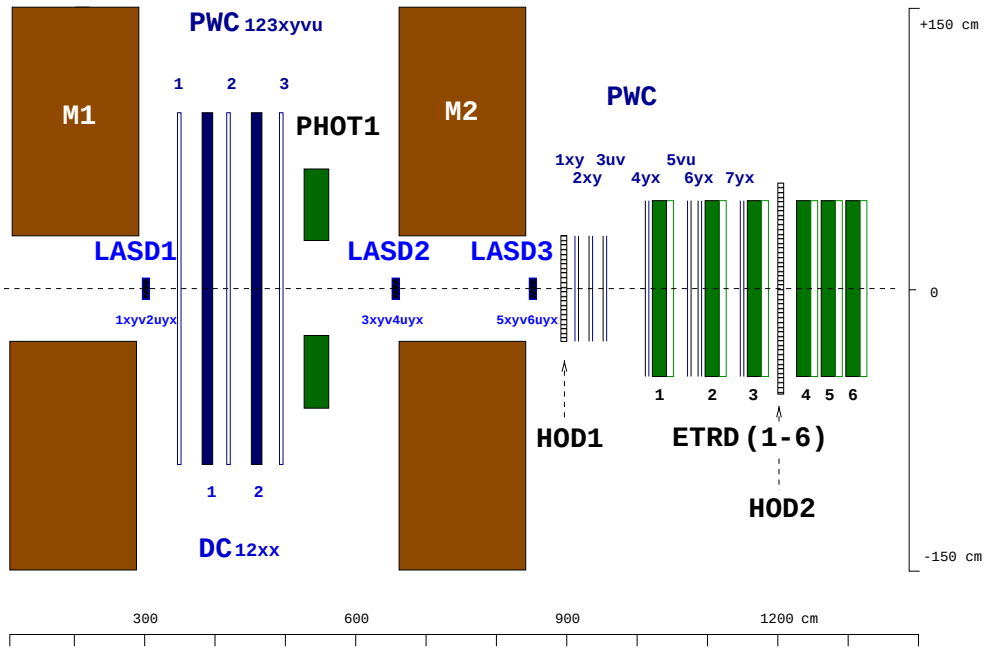

Figure 3.5: M1 spectrometer and upstream part of M2 spectrometer.

identification (Fig. 3.6). Two trigger hodoscopes (HOD1,HOD2) were located in the M2 spectrometer as well.

The M3 spectrometer

A third magnet (M3: 1.3 T, 0.72 GeV/c) was installed 42 m downstream of the charm target. This third spectrometer enhanced the acceptance for decays of long-lived hyperon states. For example, the momentum of proton and π^- out of a Λ decay could be measured this way. Again there were MWPCs, drift chambers, a lead glass calorimeter, and finally a hadronic calorimeter (NCAL) (Fig. 3.7).

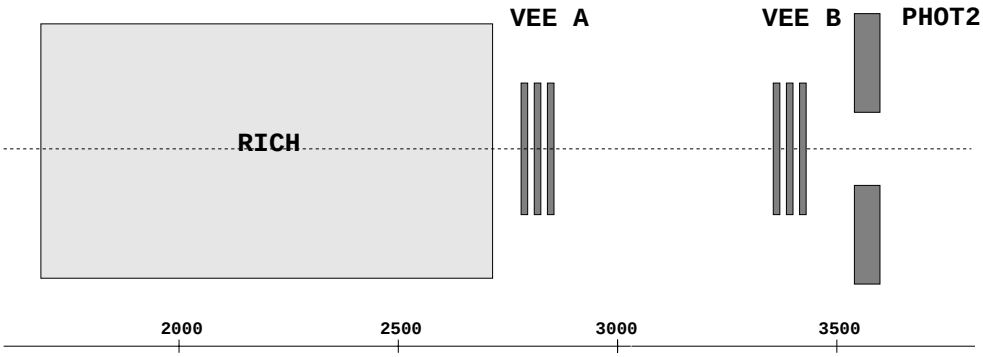

Figure 3.6: Downstream part of the M2 spectrometer

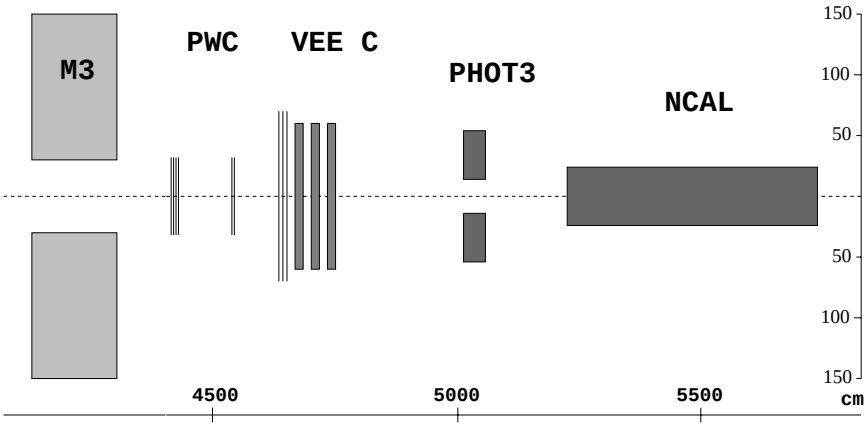

Figure 3.7: The M3 spectrometer

3.2.1 The hyperon beam

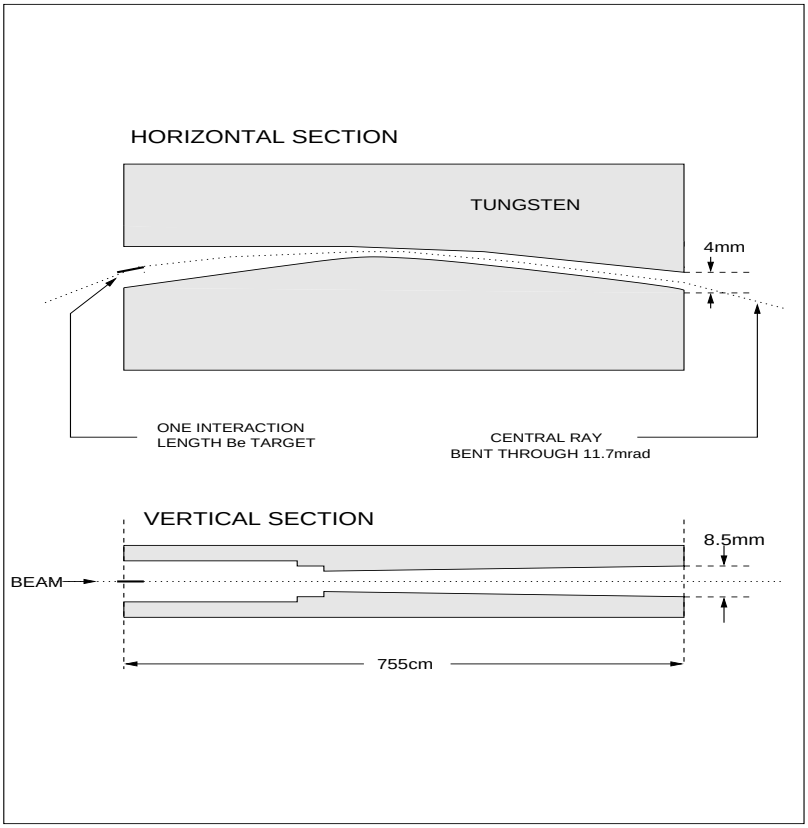

Figure 3.8: The hyperon channel [53].

An 800 GeV/c proton beam extracted from the Fermilab Tevatron was focused onto a $40 \times 0.2 \times 0.1\,\mathrm{cm}^3$ (0.98 interaction lengths) beryllium target with a spot size of less than 1 mm full width at half maximum. The beryllium target which could be exchanged for a copper target of equal interaction length was located at the upstream end of a 3.5 T magnet. The 7.5 m 13-ton magnet's gap was filled with layers of tungsten and lead, sparing out a curved channel with a rectangular aperture of $0.6 \times 0.2\mathrm{cm}^2$ at its downstream end (Fig. 3.8). At its center the channel narrowed to an aperture of about 1 mm in the bend plane. The channel turned the beam through 11 mrad. The resulting beam had a full width momentum spread of 8 % and a solid angle of 0.5 μsr [53].

At a typical intensity of $7 \cdot 10^{11}$ protons per 20-second spill the secondary beam

consisted of $1 \cdot 10^7$ Σ^- particles and an approximately equal amount of π^- in the momentum range of 600 ± 50 GeV/c .

The beam spot in the target region was of rectangular shape measuring approximately $1 \times 0.5\,\mathrm{cm}^2$.

3.2.2 Tracking

Tracking information was provided by a total of 35 planes of multiwire proportional chambers, 13 drift chamber planes, and 52 planes of silicon microstrip detectors. The SELEX coordinate system was defined by the forward (i.e. beam) direction (z) and four different transverse coordinates (x,y,u,v). The horizontal plane defined by the x and z axes was equivalent to the nominal magnet bend plane. The (y,z) plane was perpendicular to the (x,z) plane, the (u,z) and (v,z) planes had a $\pm 45°$ angle with the (x,z) and (y,z) planes.

Each spectrometer had tracking devices covering at least three out of these four projections.

Silicon microstrip detectors

In a simplified picture, a silicon strip detector can be regarded as a p-n junction in a semiconductor where the depletion zone has been extended over several 100 μm (Fig. 3.9). For example, if one surface of a n-type silicon wafer of 300 μm thickness is p^+-doped in a pattern of parallel strips, a p-n junction is formed along those strips. Neglecting further details, a voltage can be applied to the wafer/strip combination so that it acts as reversed biased diode.

A relativistic charged particle passing through 300 μm of silicon will generate $\sim$ 26000 electron-hole pairs. The holes are drawn towards the junction side and collected on one or more of the closest strips.

Obviously the resolution of a microstrip detector is related to the distance between strips (the *pitch*). The resolution is equal to $pitch/\sqrt{12}$ – 14.4 μm for a 50 μm pitch detector – if the charge is collected on a single strip. The pulse heights on adjacent strips can be compared to improve the resolution to 4 μm.

SELEX featured four independent systems of silicon strip detectors which are described in more detail below.

Hardware scattering trigger silicon detectors

Upstream and downstream of the BTRD four silicon planes were mounted as part of the *Hardware Scattering Trigger* for Primakoff physics. A fast processor defined a beam track from hits on these planes and detected scattering processes

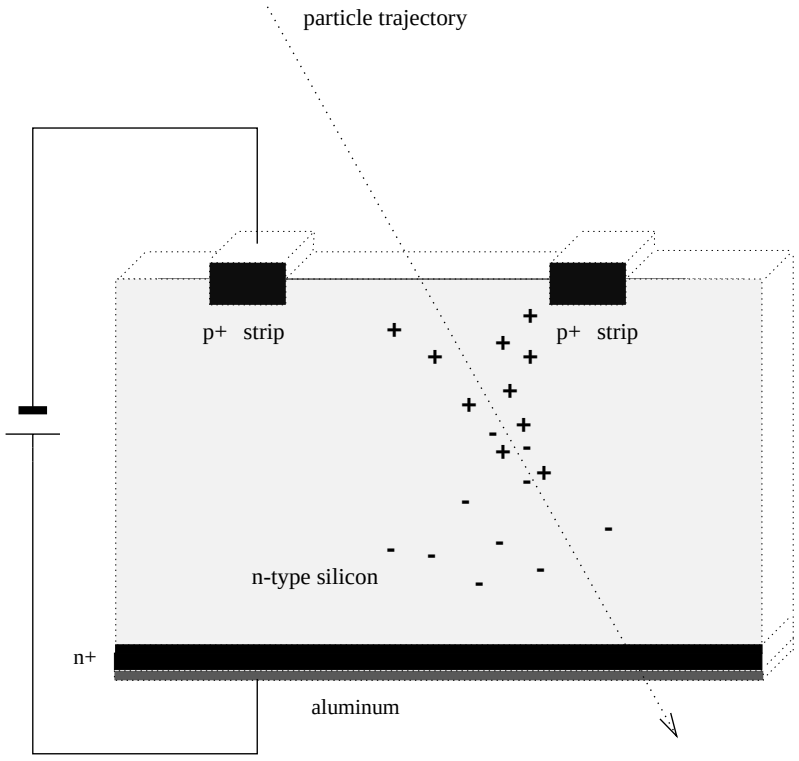

Figure 3.9: Schematic drawing of a silicon microstrip detector

with the information of 2 additional planes downstream of the vertex silicon. In order to trigger only on relevant events, the Fast Encoding and Readout System (FERS) was designed and built [54]. The detectors were fabricated on standard 300 μm thin n-type silicon with a strip pitch of 50 μm. Each of the three stations provided both x- and y-views. The detectors in the first station have 256 channels each, in the second station 320 channels each, and in the downstream vertex station 384 channels each, a total of 1920 channels. The front-end electronics consists of 4-channel charge sensitive preamplifier hybrid chips and 16-channel amplifier/discriminator cards. The 100 ns gate allowed for very fast readout, effectively adding timing information to the data. The HSD hit information could be used to select the beam track which was "in time" with the trigger out of the sample recorded by the beam silicon which had a longer gate (section below).

Beam silicon detectors

The beam track was reconstructed using 8 planes of 300 μm thick single sided silicon detectors of 2×2 cm^2 sensitive area each with 1024 strips at 20 μm pitch. The

hit efficiency of the single detectors averaged 99 % and the track reconstruction efficiency around 95 %. The beam momentum was determined by extrapolating the beam track measured in the silicon detectors upstream to the known position of the hyperon production target. A typical beam momentum distribution is shown in Figure 3.10.

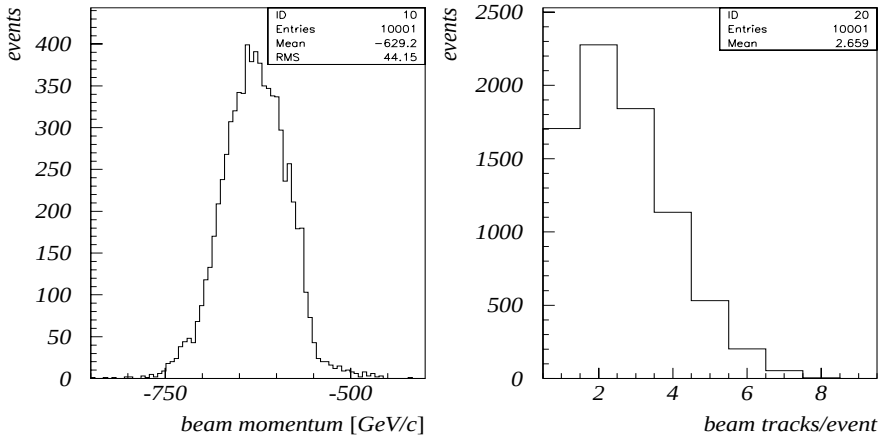

Figure 3.10: Momentum distribution of the SELEX hyperon beam (left), beam track multiplicity per event (right).

Usually several beam tracks were recorded since the beam silicon was read out by the SVX chip with a maximum possible integration gate period of 4 μs. At a beam rate of 1 MHz an average of four beam tracks per event should be expected. The measured distribution is shown in Figure 3.10. The "in time" beam track which had triggered the event had to be identified by other means, for example by including HST silicon information (section above).

Vertex silicon detectors

The vertex silicon system consisted of 20 single sided, 300 μm thin detectors, accounting for 6 x-views, 4 y-views, and 5 u- and v-views each. A set of 4 detectors was mounted on a monument block, the 5 monument blocks were fixed to a granite bench as illustrated in Figure 3.11. The upstream 8 planes had an active area of 5.12×5.00 cm^2 with 2560 strips at a pitch of 20 μm. In order to account for the 50 μm channel pitch of the SVX readout chip a fan-out was integrated along the shorter sides of the counters. The central region of 1536 strips was read out at 20 μm pitch, while only every second strip was read out in the outer regions of

512 strips each. Therefore, the total number of readout channels per detector corresponded to 2048 equalling 16 SVX chips.

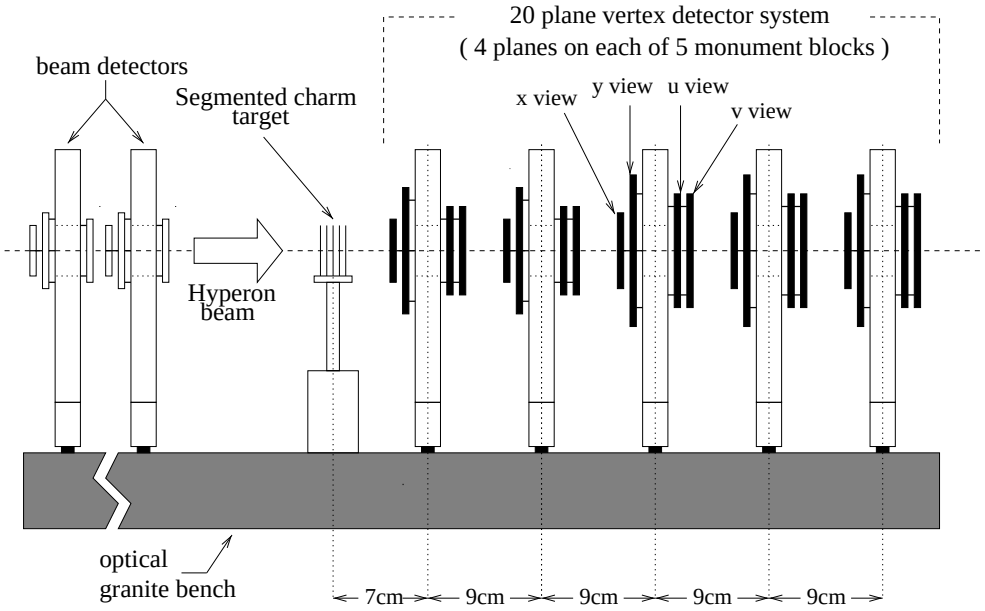

Figure 3.11: Vertex spectrometer layout [55].

The 12 downstream mosaic detectors consisted of three 8.3×3.2 cm^2 Hamamatsu counters each. 1280 strips were integrated on each panel at a pitch of 25 μm. All strips of the central panel were read out, while the readout pitch in the outer regions was reduced to 50 μm. The total number of readout channels per mosaic plane was 2560 or 20 SVX chips.

The single hit efficiency was measured to be greater than 98 %, the track reconstruction efficiency was better than 95 %, the resolution on the order of 6 μm [55].

Beam and vertex detectors as well as the charm target and trigger scintillators were enclosed in a light-tight aluminum box for RF shielding and flushed with chilled air of 19° C.

Large area silicon detectors

To enhance the resolution for high-momentum tracks downstream of the vertex spectrometer, three stations of 50 μm readout pitch large area silicon strip detec-

tors (LASD) were mounted on the shielding plates of the M1 and M2 magnets.

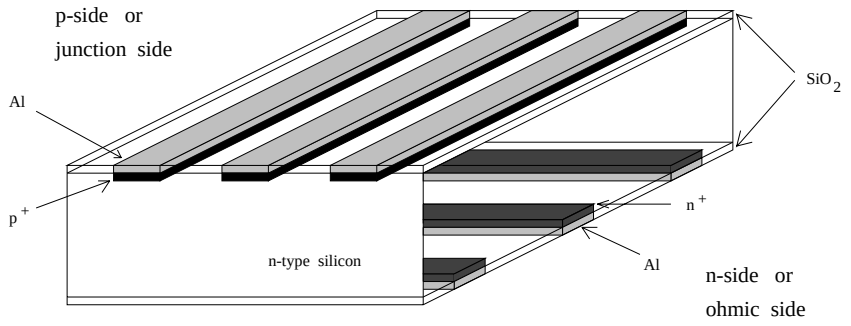

Figure 3.12: Schematic view of a double-sided silicon detector

Each station contained two single-sided and two double-sided detectors. The latter kind had strips implanted on both sides of the semiconductor in orthogonal directions, i.e. each double sided silicon detector provided both x and y coordinates while contributing radiation length only equivalent to one regular silicon plane. The single sided detectors covered the u and v projections so that every station supplied the full set of coordinates for each track.

The single sided detectors had an active area of $6.35 \times 6.35\,\mathrm{cm}^2$ with 1280 strips read out. The double sided detectors had 1024 channels on the p-side and 1280 on the n-side, covering an active area of $6.54 \times 5.26\,\mathrm{cm}^2$ [56]. The resolution averaged at 15 μm and efficiencies ranged from 91 % to 99 % [57].

Multiwire proportional chambers

A multiwire proportional chamber (MWPC) in principle consists of a plane of equally spaced anode wires centered between two cathode planes. The chamber is filled with a gas subject to ionization by a particle passing through the chamber. Ionization of gas molecules produces electrons and positively charged ions which drift in the electric field towards the closest anode wire or cathode plane, respectively. In the vicinity of a wire the field takes on a $1/r$ dependence, accelerating the electrons towards the wire. In this process the electrons will ionize other molecules on the way, i.e. produce more electrons which in turn collide with more molecules. This avalanche effect amplifies the signal related to the particle which passed through the chamber [58].

Another set of anode wires can be used in the same chamber. Oriented perpendicularly to the first set it provides a second coordinate.

The three M1 MWPCs were spaced 70 cm apart, had an aperture of 100 × 100 cm^2 and covered four projections each (x,y,u,v) at 2 mm wire spacing, i.e. $\sim$ 1 mm resolution. *Magic gas* – a mixture of argon, isobutane, and freon – was used as fill gas.

The M2 spectrometer had 7 MWPCs of 60(100) × 60 cm^2 aperture covering two projections each (either x,y or u,v). Like the M1 chambers, these had 2 mm wire spacing. They were located between the first and second hodoscope (Fig. 3.5).

Another three MWPCs (64×64cm^2 and 115×89cm^2) were located downstream of the M3 magnet.

Drift chambers

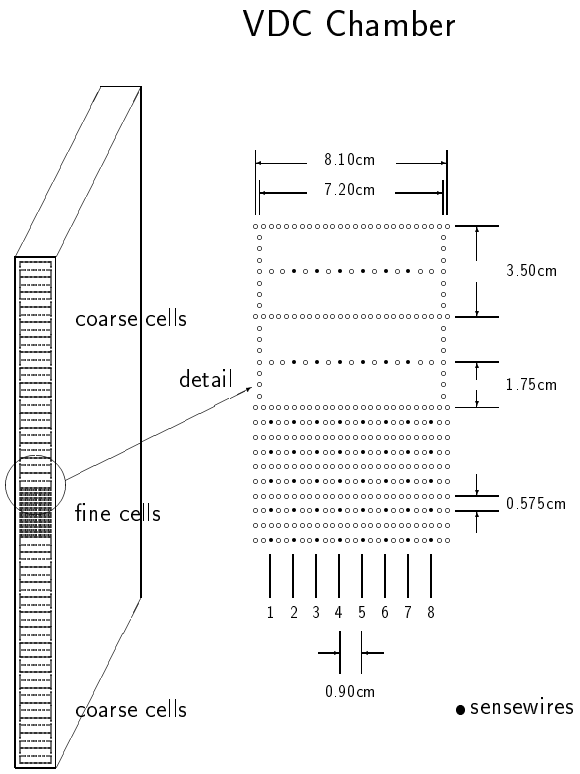

Figure 3.13: Drift cell sizes of the vector drift chambers (VDC). Each station consisted of three chambers covering three different projections [59].

If the drift velocity of electrons in a proportional chamber is known and a trigger is available to signal the arrival of a particle, the distance from the anode wire

to the origin of the electron can be calculated to enhance the resolution of the detector.

This defines the principle of a drift chamber. In practice, the drift velocity is held constant, i.e. the field is constant over the drift region (typically 5–10cm). This is achieved by lining the drift region with cathode field wires maintained at appropriate voltages. The volume enclosed by field and sense wires is called a drift cell.

The two drift chambers in the M1 spectrometer were located in between MWPCs. Each chamber consisted of two planes, covering the x and y projections [60].

Three stations of three drift chambers each (the *vector drift chambers*) provided for tracking in the downstream half of the spectrometer. They were arranged between the RICH and the Photon-3 calorimeter (figs. 3.6 and 3.7, "VEE A/B/C"). The chambers covered $116.5 \times 116.5\,\mathrm{cm}^2$ and three different projections per station (x,y,u/v). Each chamber consisted of 40 drift cells (Fig. 3.13).

3.2.3 Particle identification

The beam transition radiation detector (BTRD)

In order to discriminate π^- against heavier beam particles the relativistic Lorentz factor $\gamma = \mathrm{E/mc^2}$ may be used. For the typical beam momentum of 650 GeV/c the Lorentz factor for π^- equals $\gamma_\pi = 4676$ and for Σ^- $\gamma_\Sigma = 543$, respectively. The Lorentz factor is roughly proportional to the energy of the radiation emitted by a fast charged particle while traversing the boundary of media with different dielectrical constants. This energy of the emitted photons is in the order of several keV and detectable by multiwire proportional chambers (MWPCs). Therefore a beam transition radiation detector (BTRD) consists of several layers of radiator material to enhance the effect of transistion radiation and wire chambers to detect the radiation.

The SELEX BTRD consisted of 10 modules of 200 polypropylene foils and 3 proportional chambers each. The foils were 17 μm thick and separated by 0.5 mm gaps. The chambers consisted of aluminized mylar cathodes, 2 mm drift spaces and anode planes of 15 μm thick gold-plated tungsten wires of 1 mm spacing. They were flushed by a mixture of xenon and 30 % methane. The geometric acceptance was 3×3 cm^2, the sensitive area 2.2×2.2 cm^2 [61]. During the run the detector was shifted several times to make use of the entire sensitive area and move surfaces out of the beam acceptance which suffered from radiation damage.

Fig. 3.14 displays a typical distribution of the number of modules showing a signal. The cuts generally used were ≤ 4 for Σ^- and ≥ 7 for π^-. The efficiency

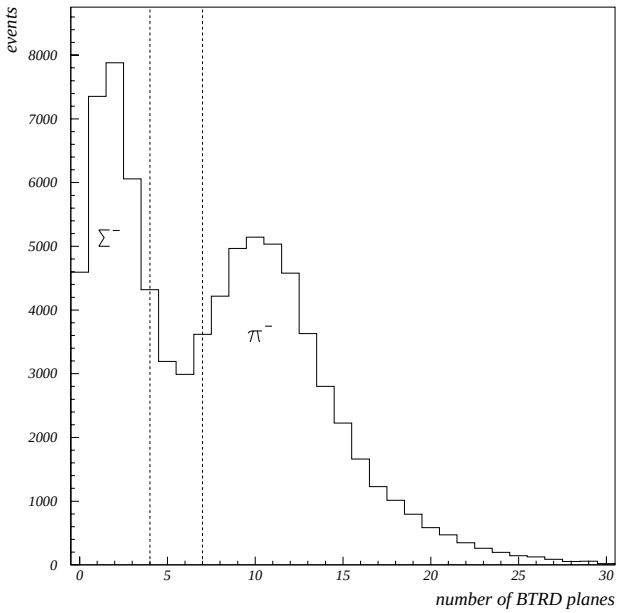

Figure 3.14: BTRD discrimination of π^- against heavier beam particles. Particles with a signal in at least seven planes are accepted as π^- .

for identifying pions is then 89.5 % with a background of 3.3 to 5.7 % Σ^- . The Σ^- detection efficiency is 91.5 % with a background of 2.2 to 6 % π^- .

The electron transition radiation detector (ETRD)

The ETRD consisted of 6 modules, each a combination of 200 polypropylene foils and a MWPC chamber. The foils were 17 μm thick and separated by 0.5 mm gaps. The chambers had 4 mm effective wire spacing and a readout aperture of $103 \times 63\,\mathrm{cm}^2$. The fill gas was a mixture of xenon and 30 % methane [62].

A charged particle was identified as an electron if the sum of clusters along the track in the 6 ETRD planes was greater than three (Fig. 3.16). In a calibration run with a 20 GeV/c e^-/π^- beam the efficiency of identifying electrons was determined to be 95 %, the efficiency to mistake a pion for an electron 1.2 %. Monitoring from standard runs yielded an average electron efficiency of 91 % and a pion efficiency of 1.2 % [63].

At higher momenta, a pion is likely to generate as many clusters as an electron (Fig. 3.15).

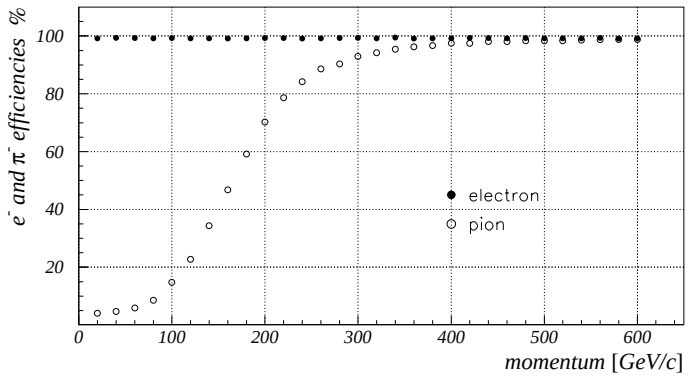

Figure 3.15: Identification efficiency for electrons and the efficiency to misidentify a pion as an electron, plotted versus momentum. The electron identification efficiency is better than 90% for momenta above 2.5 GeV/c .

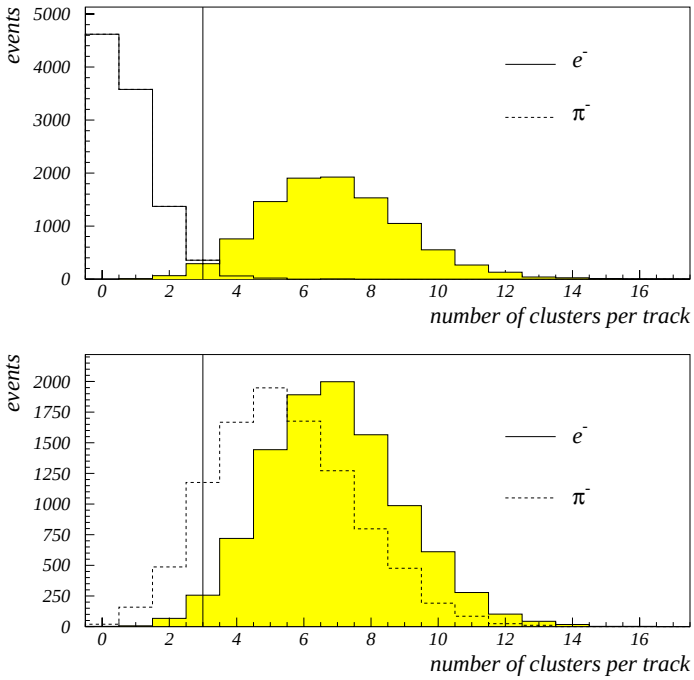

Figure 3.16: ETRD cluster sum for electrons and pions of 20 and 300 GeV/c . Vertical line indicates cut used for π^-/e separation.

The ring-imaging Čerenkov counter (RICH)

A ring-imaging Čerenkov detector (RICH) provided separation of pions, kaons, and protons up to 200 GeV/c [64].

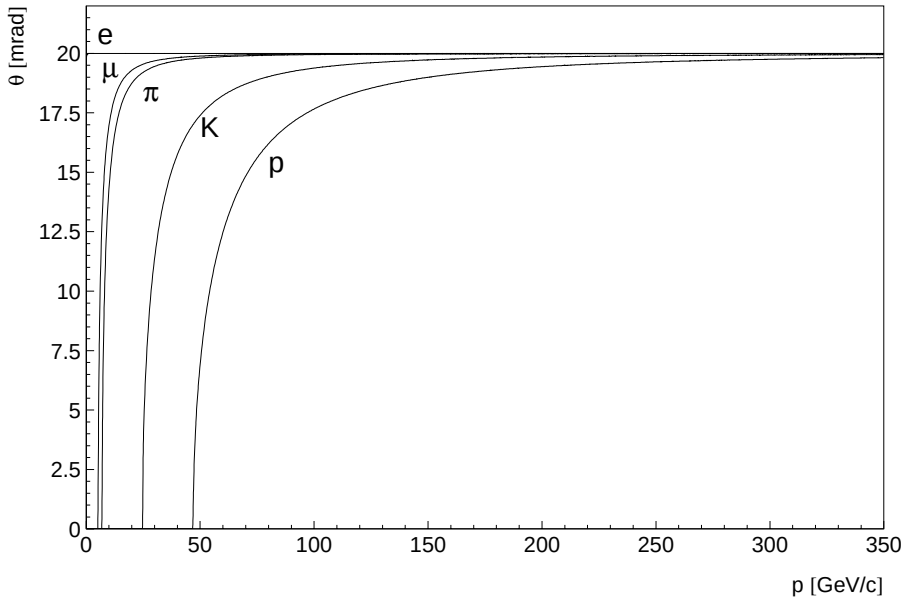

Figure 3.17: Čerenkov angle vs. momentum at a refractive index of $n = 1.0002$ for different particles.

A charged particle traversing a material of refractive index n (the *radiator*) at a velocity $v = \beta c$ higher than the speed of light c/n in this material

$$v = \beta c > c/n \tag{3.11}$$

emits electromagnetic radiation which forms a coherent wavefront – similar to the sonic shock wave created by supersonic aircraft – of conical shape. The opening angle θ of this cone is related to the particle's velocity by

$$\cos\theta = \frac{1}{\beta n(\omega)} = \frac{1}{n(\omega)\sqrt{1-\frac{1}{\gamma^2}}} \tag{3.12}$$

where ω is the frequency of the emitted radiation and $\gamma = E/mc^2$ the relativistic Lorentz factor. If the momentum of the particle is known, it can be identified by means of the Čerenkov angle θ (Fig. 3.17).

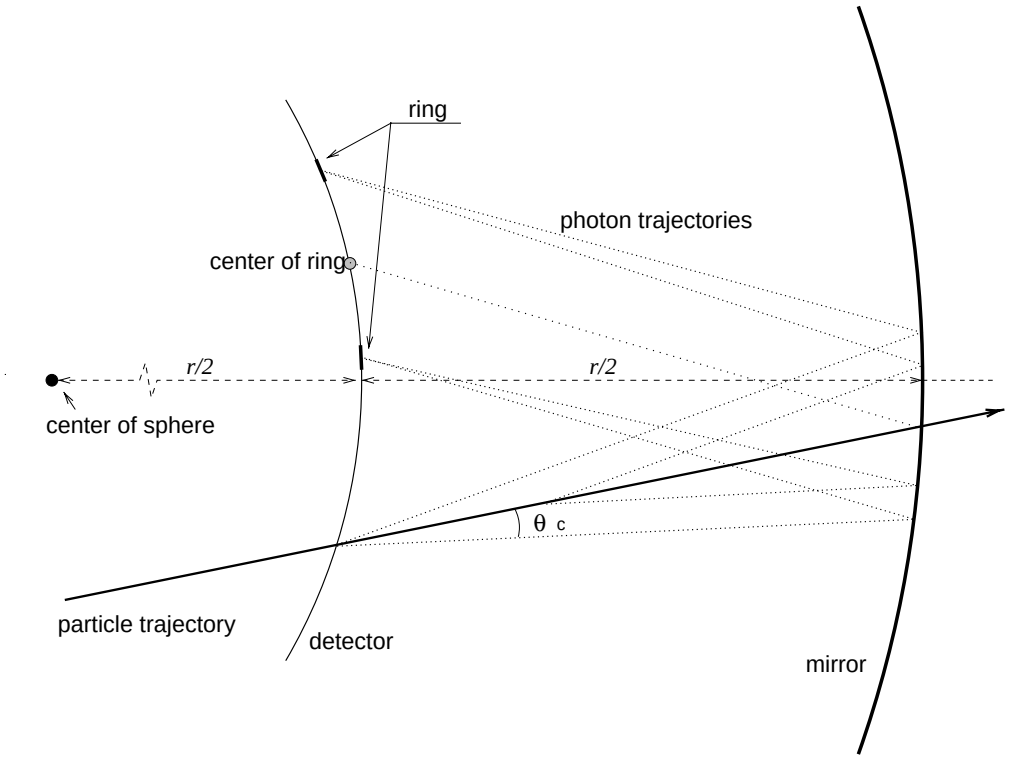

Figure 3.18: The particle passing through the RICH from the left emits Čerenkov radiation which is focused onto the detector by spherical mirrors.

A spherical mirror of radius of curvature r centered on the origin of the particle trajectory will focus the Čerenkov light cone into a ringlike image on the surface of a spherical detector of radius of curvature $r/2$ (Fig. 3.18). The Čerenkov angle θ and therefore γ can be calculated from the radius of this ring and matched to different particle hypotheses.

The SELEX RICH consisted of a 10 m long cylindrical vessel with 2.4 m diameter filled with neon at a pressure of 1.05 atm. The 16 hexagon-shaped glass mirrors with an average radius of curvature of 20 m were arranged in an array of approximately $2 \times 1\text{m}^2$. The Čerenkov photons were detected by a matrix of 2848 photomultiplier tubes which provided 100 % coverage of the detector's acceptance. The ring radius was measured with a resolution of 1.2 % [64].

The electromagnetic calorimeters

Each of the M1/M2/M3 spectrometers featured a lead glass calorimeter. This kind of detector consists of an array of glass bricks made of a mixture of PbO, SiO_2, Na_2O, K_2O, and As_2O_3 (Table 3.2). A high-energy photon or particle will produce an electromagnetic shower, i.e. electrons and positrons, inside the lead glass. These in turn emit Čerenkov light which is collected by photomultiplier tubes. The deposited energy can then be estimated by integrating over the pulse height [65]. In addition, the center of gravity of the electromagnetic shower can be calculated from the distribution of energy deposited in adjacent blocks, i.e. the coordinates of the particle can be estimated.

Table 3.2: Average composition of lead glass used in the Photon-1/2/3 detectors.

element	Pb	K	Si	Na	O
% by weight	47.3	4.5	19.3	1.6	27.2

The lead glass used for SELEX calorimeters Photon-1/2 had 4.1 g/cm^3 density and 2.5 cm radiation length. The blocks had dimensions of $4.25 \times 4.25 \times 34\,\mathrm{cm}^3$ and $8.5 \times 8.5 \times 34\,\mathrm{cm}^2$ [66], i.e. each block was the equivalent of 13.6 radiation lengths in longitudinal direction. The Photon-3 blocks measured $3.8 \times 3.8 \times 45\,\mathrm{cm}^3$ [67]. The lead glass blocks were stacked as a rectangular array with an opening centered on the beam axis.

Table 3.3: Specifications of the SELEX lead glass calorimeters.

	blocks		z-position	transverse dimensions	
	small	large	[cm]	total [cm^2]	hole [cm^2]
Photon-1	576	54	526.6	136.0×110.5	42.5×17.0
Photon-2	540	186	3573.2	229.5×110.5	50.7×41.2
Photon-3	328	–	5003.9	80.2×61.1	15.3×7.6

The neutron calorimeter

The downstream end of the spectrometer was covered by a hadronic calorimeter which could – for example – be used to distinguish beam particles from decay neutrons. The neutron calorimeter (NCAL) consisted of 50 scintillator planes sandwiched between 50 iron sheets, equivalent to 15.6 interaction lenghts. In addition, 17 PWCs were included in the upstream half.

3.2.4 Trigger elements

Next to beam and veto scintillators (Fig. 3.4 on page 27) an interaction counter (described separately in section 4.3) was installed downstream of the targets to estimate the charged particle multiplicity before any secondary interactions took place in the silicon detectors.

The hodoscopes

Two scintillation counter hodoscopes located in the M2 spectrometer provided multiplicity, charge, and momentum information for the trigger. They consisted of scintillators covering a small fraction of the spectrometer's horizontal aperture each (counter width ranging from 5 mm in the central region to 40 mm at the edges).

Table 3.4: Specifications of the hodoscopes. Both `H1` and `H2` were divided into subhodoscopes covering the negative-charge (`-`), positive-charge (`+`), and central (`0`) regions of the M2 spectrometer.

	z-pos. [cm]	area covered [cm^2]	elements		
			-	0	+
H1	890.9	$60.0 \times 30.5\,cm^2$	16	8	14
H2	1292.1	$119.0 \times 40.6\,cm^2$	12	16	32

4

The Trigger

The SELEX trigger environment was dictated by the high-intensity beam of up to 40 million particles per 20-second spill, i.e. a beam rate of 2 MHz, or on average one beam particle every 500 ns. At this time scale the propagation delay of an electronic pulse in standard coaxial cable – approximately five nanoseconds per meter – is already one limiting factor in trigger design. To limit cable delays the trigger electronics were placed as close to the spectrometer as possible, at the disadvantage of not being accessible during operation. Therefore CAMAC-programmable electronics were used consistently so that changes to the trigger logic could often be accomplished without having to turn off the beam.

The event rate was limited by the total data transfer rate on one hand and by deadtime one the other, depending on operating conditions.

4.1 Trigger and data acquisition concepts

The main objective of the experiment being production and spectroscopy of charmed baryons at high x_F, i.e. short-lived particles of neutral or positive charge produced by a beam-target interaction, the trigger had to look for a secondary vertex and at least two fast positive particles. A typical situation is the production of a Λ_c^+ which decays to

$$\Lambda_c^+ \to pK^-\pi^+.$$

Since online vertex reconstruction would have been too slow for triggering, SELEX followed the idea of an *impact parameter trigger*: find a beam track and a vertex, and accept only if they do *not* match. The miss distance or impact parameter was required to be larger than 20μm.

The SELEX trigger was designed as a four-level trigger, where the last level was in fact a software trigger [68, 69].

The beam definition was given by a set of scintillation counters (see Fig. 3.4 on page 27):

$$\mathtt{T0} = \mathtt{S1} \cdot \overline{\mathtt{VH1}} \cdot \mathtt{S2} \cdot \overline{\mathtt{VH2}} \cdot \mathtt{S4} \cdot \mathtt{V5} \tag{4.1}$$

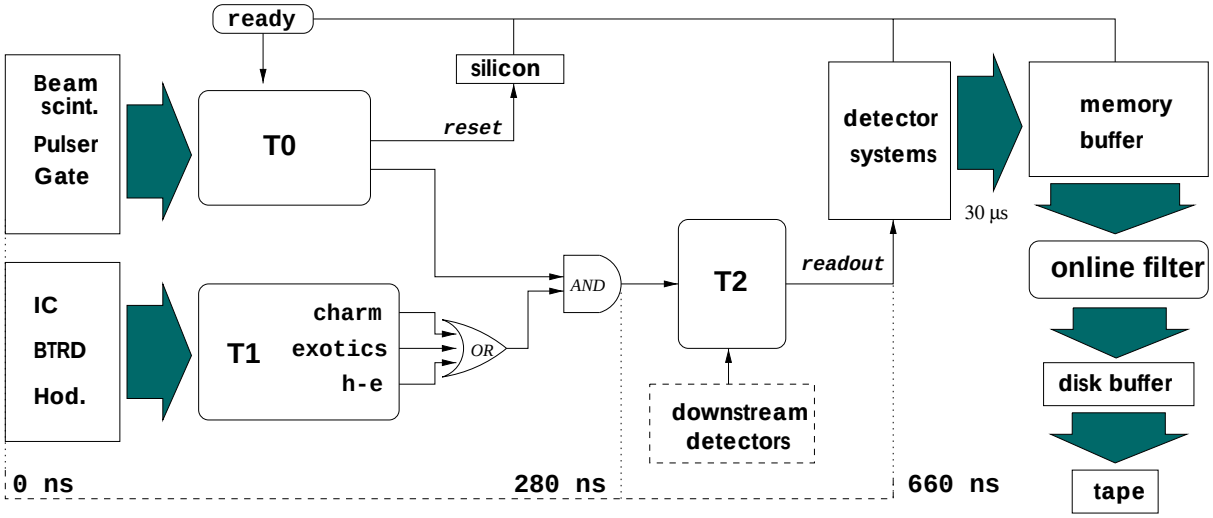

Figure 4.1: A simplified scheme of the SELEX trigger and data acquisition system. Next to the interaction trigger which required coincidence of T0 and T1 a beam trigger (T0 only) and a random trigger (T0 only, using a pulser) was available for calibration purposes.

The first trigger level (T0) fired if a valid beam definition coincided with ready state of the apparatus. The T0 signal provided the synchronisation for the experiment. At typical operating conditions the T0 stage reduced the gated beam trigger rate of $10 \cdot 7$/spill (0.5 MHz) to $1.5 \cdot 6$ (75 kHz).

The second trigger level (T1) decision was formed from BTRD and multiplicity information. Coincidence of T0 with T1 handed the event to the third trigger level (T2), which had been established to include information from slower or downstream detectors if needed. At normal operating conditions, however, T2 was equal to the T1–T0 coincidence, with a typical rate of 80,000 events per spill (4 kHz).

If the event had passed these three levels all systems were read out into dual-ported memories and the event analyzed by online filtering software running on a 17 processor SGI Challenge. The filter process included a partial reconstruction of the interaction vertex and the beam track. If the vertex had sufficient miss distance to the beam track the event was written to hard disk and later to tape.

The following calculation may illustrate the need for disk buffering. At a typical rate of 80,000 T2 triggers per spill one could expect 10,000 events to pass

the filter. Then, for the average event size of 5 kilobytes (with all systems read out) the disk space needed per minute equals 50 megabytes. SELEX had two 9-gigabyte disks dedicated to data buffering. Even if all of the four 8mm tape drives had failed the experiment could have stayed alive at this rate for three hours.

Calibration data was taken constantly with a minimum bias trigger at 1/6000 of the charm trigger rate at the first level.

10 % of the bandwidth were allowed to be used by different triggers running in parasitic mode (i.e. in parallel to the charm trigger, synchronised with its beam definition, and compatible with its structure). Parasitic triggers in SELEX included the hadron-electron trigger described below which was commissioned at the beginning of the official data-taking period in February 1997 and the exotics trigger, based on a 3-prong event topology, which joined in May 1997.

4.2 The hadron-electron scattering trigger

The topology of elastic scattering of beam particles on electrons is given by exactly two negative-charge tracks originating in one of the targets (Fig. 4.2).

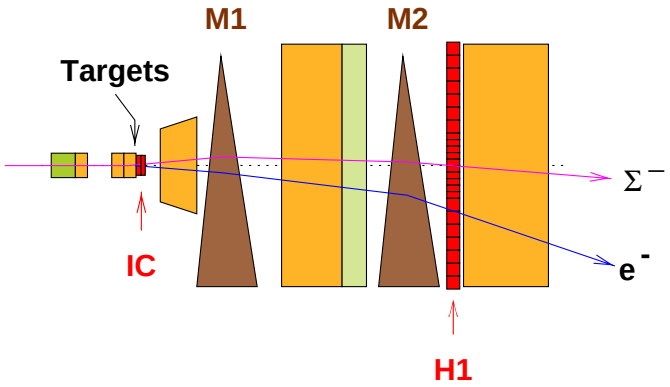

Figure 4.2: Event topology and elements of the hadron-electron elastic scattering trigger.

$\Sigma^- \to \pi^- n$ decays leave the event topology unaltered in the sense that one has two negative particles at all times. In the case of Ξ^-, this is true for the predominant decay mode $\Xi^- \to \pi^- \Lambda$ unless the Λ also decays upstream of H1.

The hadron-electron (h-e) elastic scattering trigger was designed to run parasitically as part of the standard interaction trigger.

The h-e trigger decision relied on the interaction counter (IC) and the first hodoscope (H1) which is logically divided into three subhodoscopes covering the negative ($H1^-$), beam-like ($H1^0$), and positive ($H1^+$) region. Centered approximately on negative 600 GeV/c beam, the central ($H1^0$) subhodoscope would trig-

ger on most particles with high momentum regardless of charge if they originated from the target.

The interaction counter (section 4.3) estimated the charged particle multiplicity directly downstream of the target.

Combining a valid beam definition T0 with the requirement for exactly two negative particles this trigger condition can be written as (in this notation, '$\cdot$' refers to a logical *AND* operation and '+' to a logical inclusive *OR*):

$$\mathtt{T1}_{he} = \mathtt{T0} \cdot [\mathtt{IC} = 2] \cdot [\mathtt{H1}^- = 2]. \tag{4.2}$$

We have to account for the common case that one of these particles has fairly high momentum and passes through $\mathtt{H1}^0$ instead of $\mathtt{H1}^-$:

$$\mathtt{T1}_{he} = \mathtt{T0} \cdot [\mathtt{IC} = 2] \cdot [((\mathtt{H1}^- = 2) \cdot (\mathtt{H1}^0 = 0)) + ((\mathtt{H1}^- = 1) \cdot (\mathtt{H1}^0 = 1))] \tag{4.3}$$

Furtheron, we do not want any positive particles:

$$\begin{aligned} \mathtt{T1}_{he} = \quad & \mathtt{T0} \cdot [\mathtt{IC} = 2] \cdot \\ & [((\mathtt{H1}^- = 2) \cdot (\mathtt{H1}^0 = 0)) + ((\mathtt{H1}^- = 1) \cdot (\mathtt{H1}^0 = 1))] \cdot \\ & [\mathtt{H1}^+ = 0] \end{aligned} \tag{4.4}$$

These are the ideal trigger conditions. For technical reasons they could not be implemented from the first day. The h-e trigger rather evolved towards these conditions [70].

4.2.1 Implementation history

The very first implementation of the h-e trigger was constrained by an unfavorable beam definition. T0 is defined by an *AND* of the beam and veto scintillators, including an interaction veto counter V5 (equation (4.1)). The V5 threshold was set to an equivalent of roughly 3.5 MIPS, i.e. at least three charged particles downstream of the vertex silicon – the minimum topology of a charm event. The purpose was to cut off beam events in a very efficient way in order to decrease deadtime. This condition obviously kills most of the two-prong candidates.
Another constraint was given by the lack of discriminator channels for $\mathtt{H1}^-$. The only thresholds available were $\mathtt{H1}^- > 0, \mathtt{H1}^- > 1$ so it was not possible to cut on $\mathtt{H1}^- > 2$.

It was not known at that time to what extent one had to deal with fake correlations. One known cause are particles originating from the production target which propagate through the hyperon magnet's coils (muons for example [33]).

This means they form a halo around the selected beam but never actually come close to it. If, for example, a muon at a transverse distance of 30 cm from the beam axis propagates through the M1 and M2 magnets it may strike the outermost element of $\mathtt{H1}^-$. If a non-interacting beam particle hits $\mathtt{H1}^0$ at the same time the hodoscope part of the trigger requirement is already met. A single charged particle can easily produce a 2 MIPS signal in the IC due to Landau fluctuations. However, this background can be reduced by a good calibration of the IC .

If a valid elastic scattering event is accompanied by a muon it would look like a 3-prong, so vetoing on more than 2 particles could actually kill a good event. As a consequence the cuts on $\mathtt{H1}^-$ and $\mathtt{H1}^+$ were kept very loose:

$$\begin{aligned} \mathtt{T1}_{he} = \quad & \mathtt{T0} \cdot [\mathtt{IC} = 2] \cdot \\ & [((\mathtt{H1}^- \geq 2) \cdot (\mathtt{H1}^0 = 0)) + ((\mathtt{H1}^- \geq 1) \cdot (\mathtt{H1}^0 = 1))] \cdot \\ & [\mathtt{H1}^+ \geq 2] \end{aligned} \tag{4.5}$$

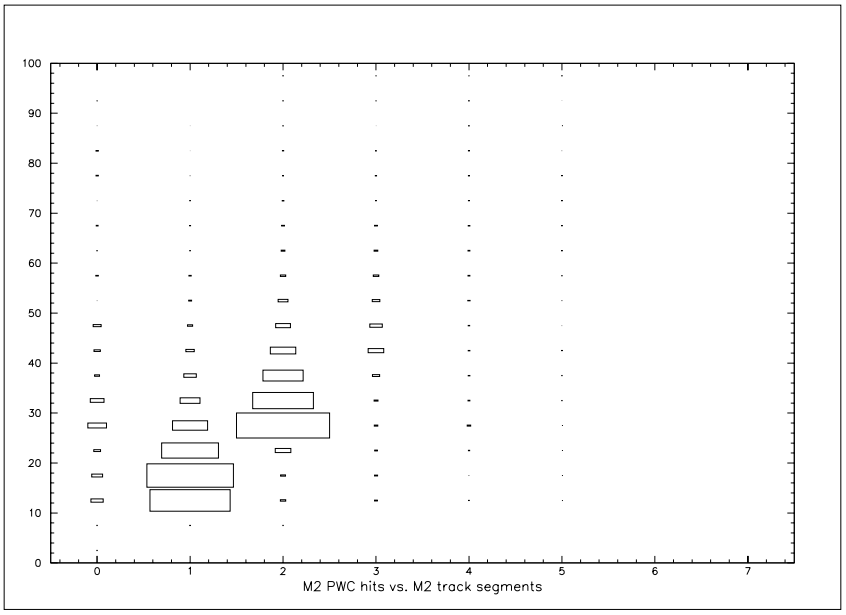

Figure 4.3: M2 total PWC hits vs. M2 track segments. The online filter rejected events with less than 20 hits.

Finally, the $\mathtt{T1}_{he}$ rate had to stay well below 10 % of the charm trigger T1 rate. The main background being beam events with Landau fluctuations in both IC counters, the rate was adjusted by raising the IC thresholds and thus narrowing the acceptance window for 2 MIPS events (cf. section 4.3).

After it had been proven that deadtime would not increase by more than 1 % the effective V5 threshold was lowered to less than 2 MIPS (run 7019).

The data taken with this trigger was found to have a very high background of 3–prong events. This was attributed to the open $\mathtt{H1}^+$ cut and inefficiencies of the hodoscope and interaction counter.

Fake events involving positive tracks (like the beam/muon combination described above) turned out to be a negligible background [70]. Therefore the cuts on $\mathtt{H1}^+$ and the total H1 multiplicity were tightened.

The second version of the h-e trigger featured

- A better calibration of the IC ,
- the possibility to count total multiplicity in H1 after more discriminator channels had been added,
- hard cuts on $\mathtt{H1}^+$ and total multiplicity after fake correlations were found to be a percent effect. The rate was now controlled by these cuts instead of the IC thresholds so
- the IC thresholds were adjusted to maximum 2 MIPS window size.
- further rate control by vetoing on the H2 horizontal counters.

The trigger decision became

$$\begin{aligned} \mathtt{T1}_{he} = \quad & \mathtt{T0} \cdot [\mathtt{IC} = 2] \cdot \\ & [((\mathtt{H1}^- \geq 2) \cdot (\mathtt{H1}^0 = 0)) + ((\mathtt{H1}^- \geq 1) \cdot (\mathtt{H1}^0 = 1))] \cdot \\ & [\mathtt{H1}^+ = 0] \cdot [\mathtt{H1}^{total} = 2] \\ & [\mathtt{H2}^{horiz} = 0] \end{aligned} \tag{4.6}$$

Later, an online filter was implemented which tested the data for

- at least one beam segment,
- not more than six beam segments,
- a maximum number of hits in beam, vertex, and M2 spectrometers (200, 1000, and 200, respectively) and less than 1000 SVX words,
- no positive-slope M2 segments.

This took care of part of the hodoscope inefficiencies. The typical rejection factor was 1:1.2.

Two more requirements were added after run 10386:

- a minimum of 20 hits in the M2 chambers (Fig. 4.3),

- at least one negative M2 segment.

The rejection of this filter was on average 1:1.7.

4.2.2 Performance

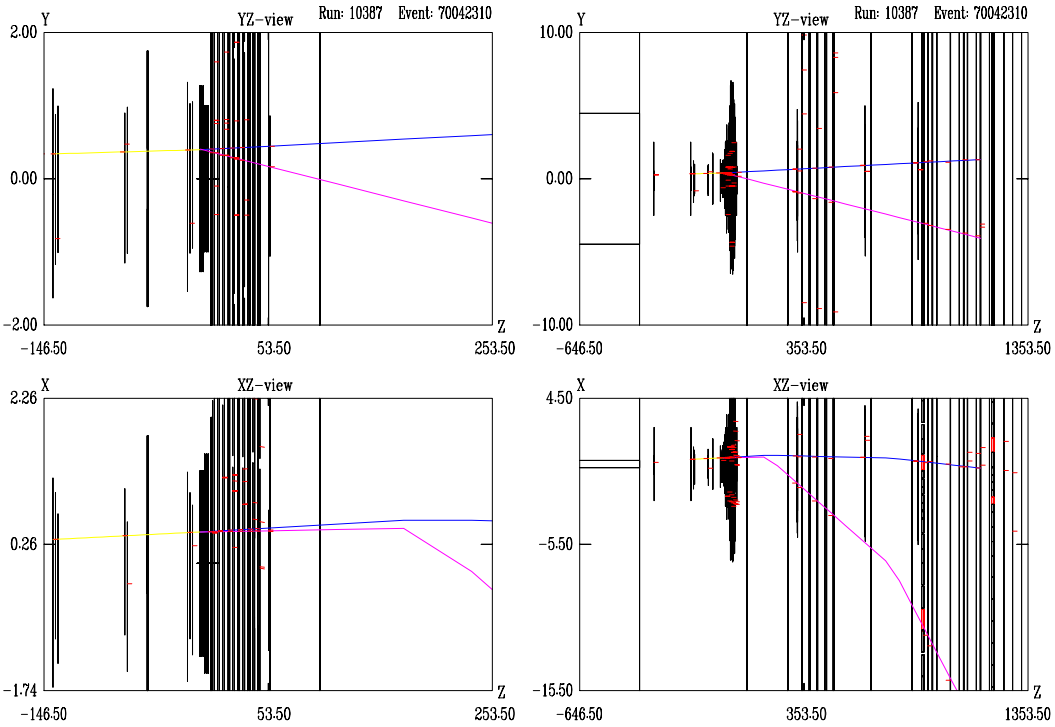

Figure 4.4: A typical event which matches the h-e trigger conditions, as seen with the SELEX event display. Top row: view in the non-bend plane, bottom row: magnet bend plane. Pictures on the left have zoomed in on the vertex detector, pictures on the right include the M2 chambers as well.

A total of 215 million h-e events from negative beam have been written to tape. The efficiency of the h-e trigger can be studied by evaluating certain critical parameters, for example the fraction of events with exactly two reconstructed negative-slope M2 segments (Fig. 4.6). Even though this number depends on the track reconstruction efficiency as well, it can be used to compare different trigger versions. Fig. 4.5 shows that before the V5 high voltage was adjusted, only one third of the h-e events matched this basic requirement. After the V5 voltage was raised, this fraction was above 50 % and above 60 % when the new trigger version was implemented. The filter increased this ratio to 67 %.

Table 4.1: Strip1 and final cut yields for data taken with different trigger versions. Yields are calculated as fraction of the total h-e trigger data of the specified runs, i.e. the Σ^-/π^- ratio is not taken into account.

trigger version	runs in sample	Strip 1 [%]		final sample [%]	
		Σ^-	π^-	Σ^-	π^-
1st h-e trigger	6822 – 7018	3.8	6.8	0	0
V5 threshold lowered	7019 – 9047	3.3	12.0	0.0020	0.0093
new IC thresholds	9048 – 9098	1.9	28.7	0.0021	0.0066
2nd h-e trigger	9099 – 9653	3.3	14.9	0.0056	0.0215
online filter	9654 – 10061	4.3	15.9	0.0102	0.0260
IC voltage lowered	10062 – 10127	3.5	13.9	0.0042	0.0135
new IC thresholds	10128 – 10385	2.9	14.4	0.0118	0.0285
2nd filter version	10386 – 10858	4.4	17.8	0.0202	0.0465

In addition, one can estimate the relative improvement of background rejection at the trigger level by comparing the yields of h-e data stripping for the different versions of the trigger (Table 4.1). The strip 1 requirements were based mainly on M2 data, the main cut being electron identification (see 5.2.1). The strip 1 yields can be compared to the fraction of h-e trigger events which survived all cuts in the Σ^- and π^- charge radius analysis (section 5.3.1).

In general, the strip 1 yields show a slight increase from the original to the second filtered version. In some cases the trends for Σ^- data do not follow those observed in π^- data. This may have its reason in other run conditions as well.

The trends are more pronounced in the final sample. While the yields are zero for data taken before the V5 threshold was lowered, they increased from the first to the last version of the h-e trigger by a factor of 10 for Σ^- and a factor of five for π^- data.

4.2.3 Background

Known background consists mainly of beam and three-prong events (two negative plus one positive particle).

Beam events can lead to a positive trigger decision if

- the IC sees 2 MIPS due to Landau fluctuations and/or noise *and*
- H1 sees 2 particles - one would be the beam particle, the second one could be from a secondary interaction either upstream of H1 or inside the hodoscope itself, for example a δ electron, or noise.

- two beam particles pile up inside one gate period.

The noise level in the electronics can be estimated from the fraction of h-e trigger events which show less than two hits in H1 . This number increased from 7 % to 25 % throughout the run. However, it is in part due to a timing difference between the pulse which went to the trigger curcuits and the pulse which was recorded with the event. It can only be considered an upper limit for line noise which affected the hodoscope signals. The only means for rejecting three-prong events in the first version of the trigger was the upper IC threshold. The cut on two particles maximum in H1 implemented in the second version reduced this background considerably. Events which passed due to H1 inefficiency were rejected by the online filter.

If, however, the positive track is bent out of the spectrometer by the M1 magnet (Fig. 4.7) *and* the energy deposited in the IC is not sufficient to fire the upper threshold this event will look like a valid two-prong to both trigger and filter. It can only be unmasked by reconstructing the vertex.

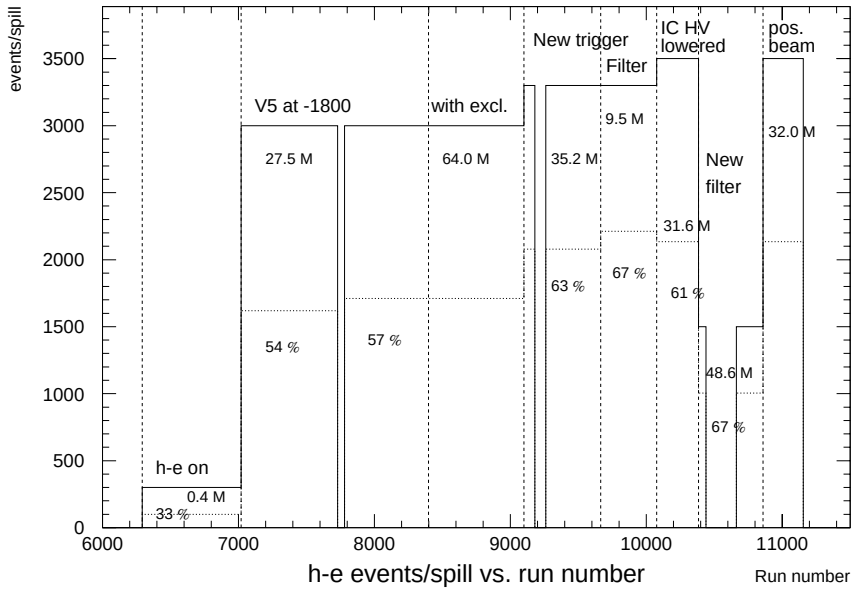

Figure 4.5: Average h-e events written to tape per spill versus run number. The fraction of events with exactly two M2 negative track segments is given in percent, as a rough evaluation of trigger and filter efficiency. The total number of h-e events written are given for the individual trigger/filter versions.

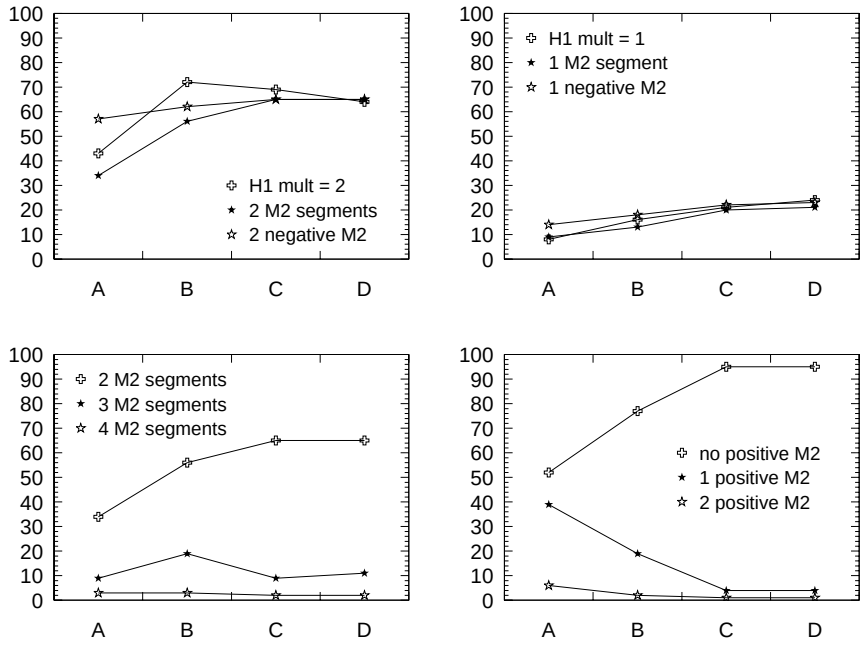

Figure 4.6: The improvement of the h-e trigger efficiency is reflected by the fraction of events with two and only two negative M2 track segments (upper left). Shown are the first trigger version (with V5 threshold adjusted) (A), the second version (B), the second version after implementation of the first (C), and the second (D) filter version. Lines are drawn to guide the eye. – The noise contribution from the hodoscope can be estimated from the fraction of events with only one M2 track (upper right). While the fraction of events with two M2 tracks increased the fraction of events with more than 2 M2 tracks remained approximately constant (lower left). The background level is also reflected by the fraction of events with positive M2 tracks, which was reduced to less than 5 % after implementation of the online filter (lower right).

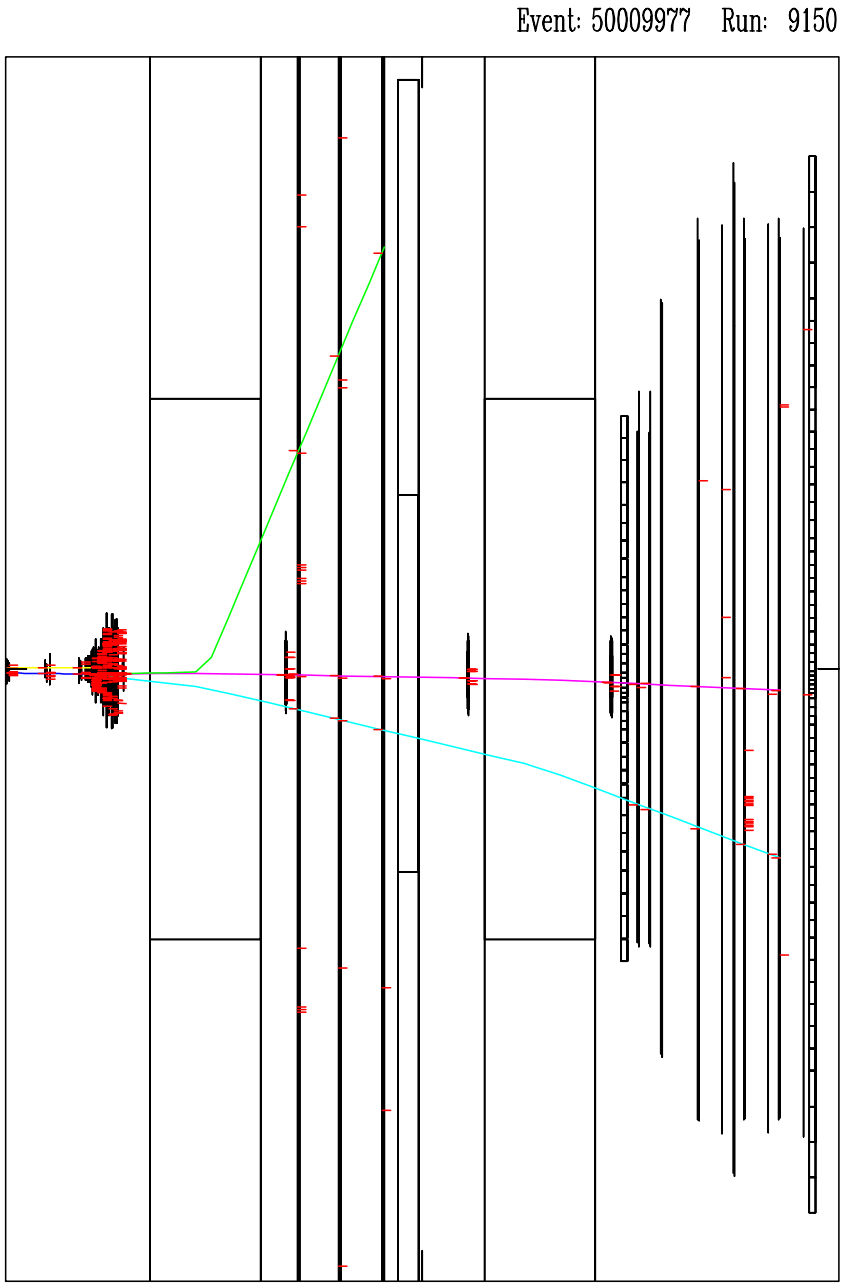

Figure 4.7: Display of a three-prong event with a low-momentum positive track. This event was accepted by both trigger and filter since it matched the hodoscope requirements. It must be concluded that the energy deposition in the `IC` was below the 3-MIPs threshold.

4.3 The interaction counter

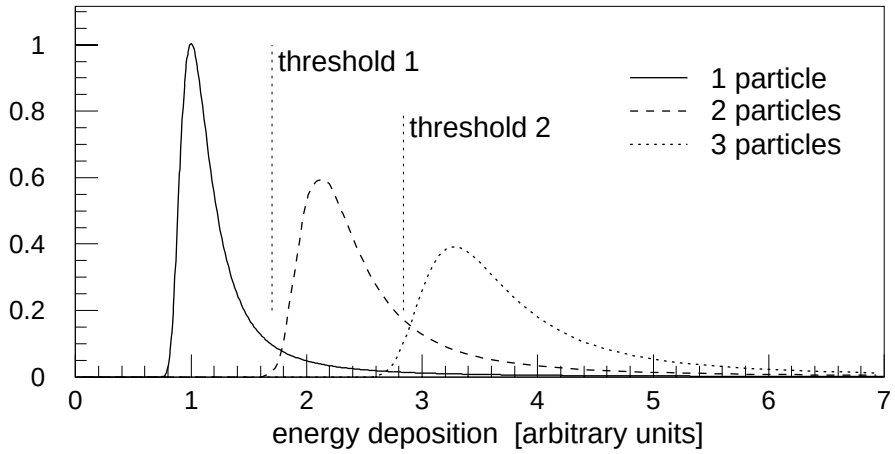

Figure 4.8: Idealized picture of how multiplicity can be counted using a scintillator. The minimum energy deposited by one charged particle in a given scintillator is approximately constant, the spectrum is Landau-distributed [58]. If more than one particle pass through the scintillator the deposited energy adds up. Selecting events with two particles means rejecting those where the energy deposition is either lower than the minimum for two particles (threshold 1), or higher than the minimum for three. Due to the Landau form of the energy spectrum background cannot be avoided. However, it can be reduced by combining the information from several counters.

The SELEX spectrometer features 32 planes of silicon microstrip detectors downstream of the target. While providing superb tracking capability, they are also a source of secondary interactions (32 planes of 300 μm are equivalent to 2 % of an interaction length). A trigger decision based on charged particle multiplicity thus cannot rely entirely on the hodoscopes.

The interaction counter (`IC`) served the purpose of estimating the multiplicity directly downstream of the target. Assuming that the energy deposited in a given scintillator by a minimum-ionizing particle (MIP) is constant, the multiplicity can be counted simply by measuring the total energy deposition (Fig. 4.8). In practice, one counts the charge deposition by integrating the pulse of the photomultiplier tube. For the given trigger purposes, however, this would have been too slow. Alternatively the pulse height can be used as if pulse shape and width are approximately constant.

The constraints on this multiplicity counter located between target and vertex silicon were that it had to be compact in size and contribute as little material as possible while operating at highest possible efficiency.

Thick scintillators were out of the question. A thin scintillator, though, would not be as efficient. In addition, since the energy deposited by a minimum-ionizing particle in a scintillator is Landau–distributed and not Gaussian, the multiplicity can easily be overestimated.

The individual energy deposition is purely statistical, though, i.e. if a particle has deposited enough energy in one scintillator to be mistaken for two of its kind, it will not necessarily deposit an equal amount of energy in a second scintillator of identical characteristics.

The concept of the IC was to use independent twin counters and compare their pulse heights.

The combination of choice [72] was a BC408 plastic scintillator [73] which has a 2.1 ns time constant read out by a Hamamatsu R1405 10-stage phototube with 19.5 ns transition time [74]. Complete technical specifications are listed in Table 4.2. The pulse, typically less than 25 ns wide, was run through a linear fan-out and a passive splitter to produce two full-height and four quarter-height signals (Fig. 4.10). One channel of the fan-out was fed into an ADC so the charge deposition could be recorded for calibration purposes. These were fed into a CAEN C207 discriminator with individually programmable channels [75]. Each counter's signal was tested against six different thresholds (1–6 MIPs, approximately 1 MIP difference between thresholds). The 1- and 2-MIP thresholds were applied to the full-height signals. The discriminator's ECL output was fed through a LeCroy 2373 memory lookup unit which performs the logical–*AND* combination of the discriminator output bits within 40 ns [76]. The multiplicity decision was delivered to the T1 trigger processor via ECL cable.

Prior to installation in SELEX the IC setup was tested with a 70 GeV/c π^- beam at CERN [71]. The tests showed that the contamination due to one-particle events can be reduced by up to a factor of ten at otherwise ideal conditions when two counters are used for the decision (Fig. 4.9).

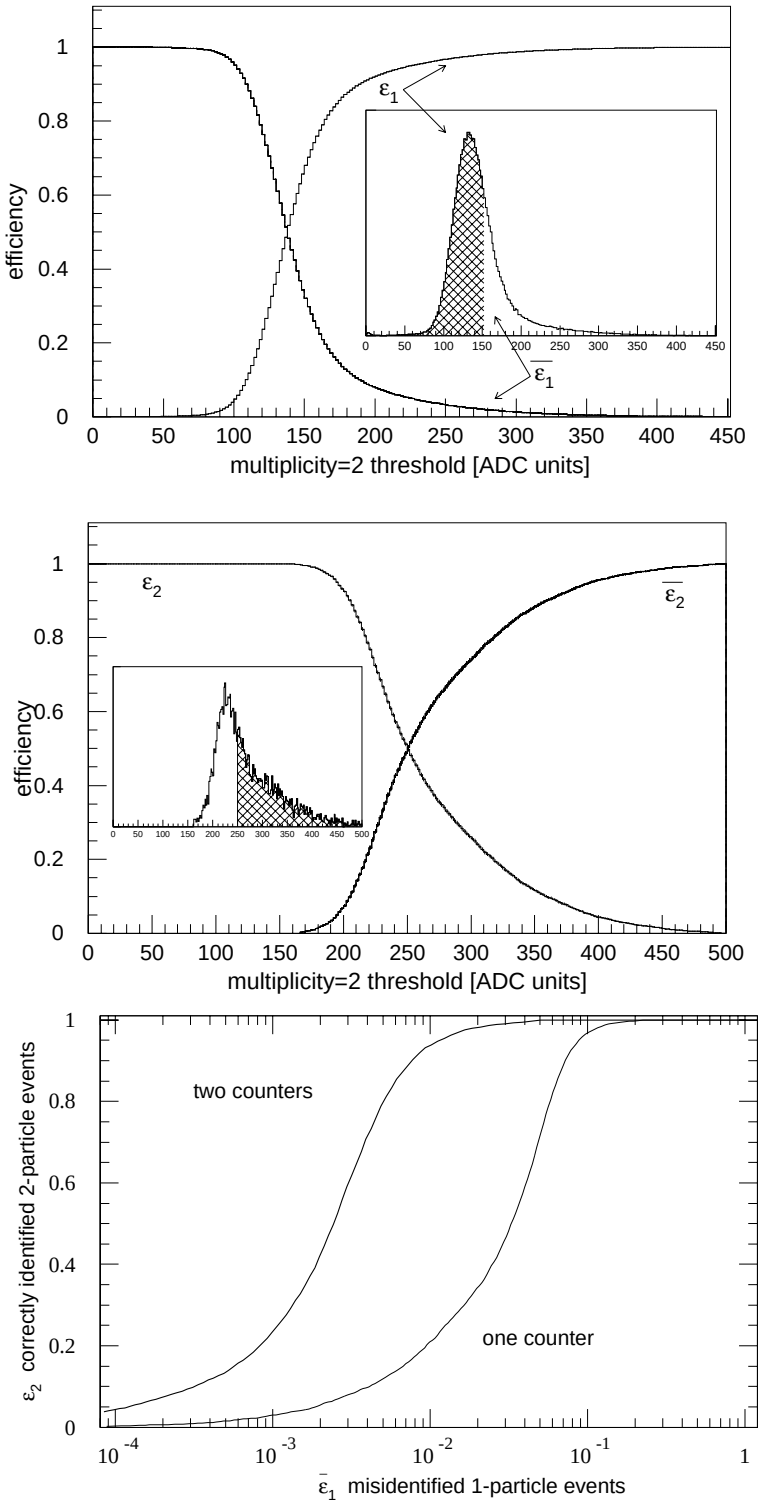

Figure 4.9: Top: The efficiency ϵ_1 for correctly identifying a 1-MIP event versus the 2-MIP threshold. The inefficiency $\overline{\epsilon_1}$ is shown in the same plot. – Center: the efficiency for identifying a 2-MIP event ϵ_2 and the inefficiency $\overline{\epsilon_2}$ for the same process. – Bottom: Efficiency of identifying a two-particle event vs. the inefficiency of identifying a one-particle event (i.e. mistaking it for a two-particle event) [71].

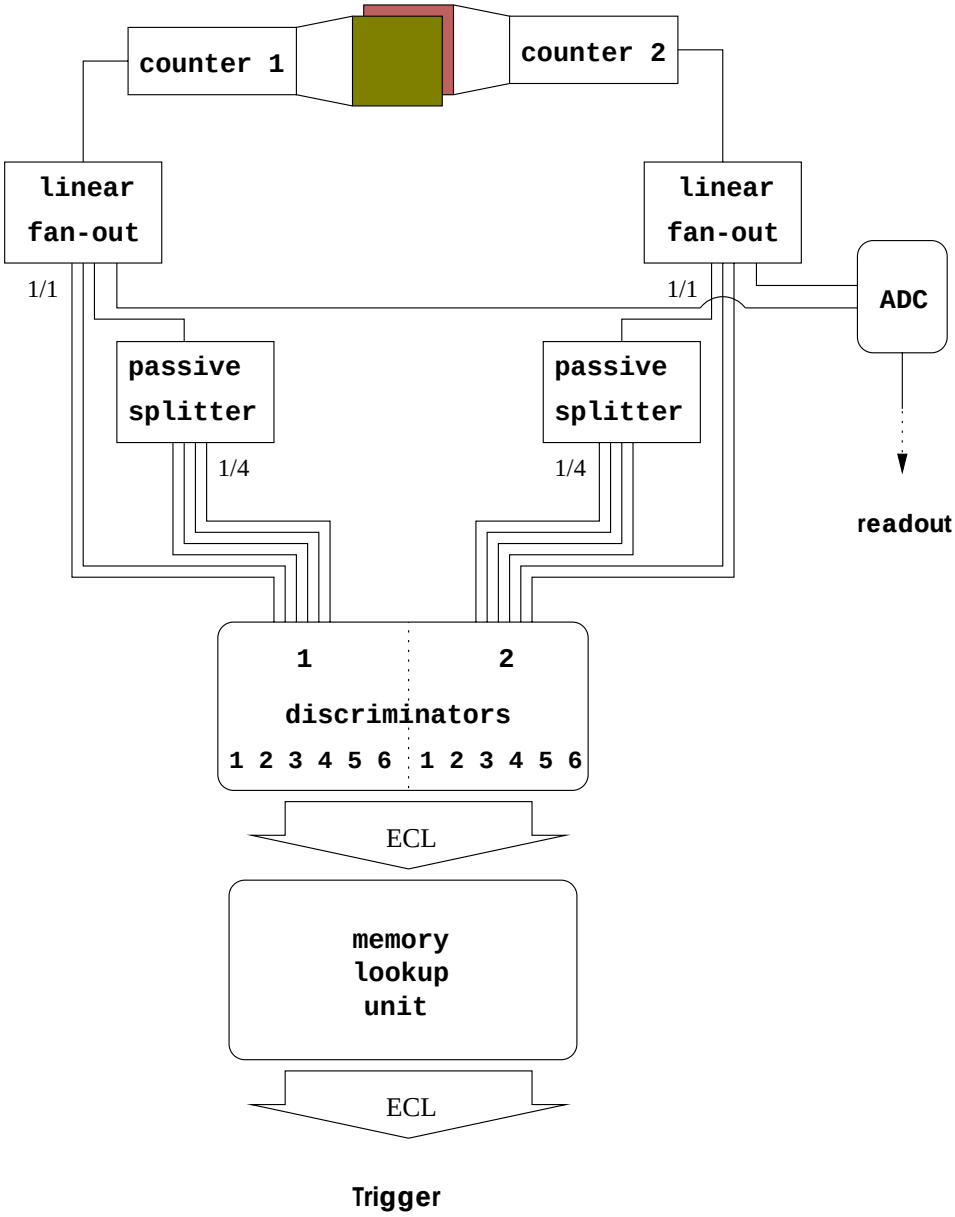

Figure 4.10: Schematic diagram of the interaction counter logic as implemented in SELEX .

Table 4.2: Technical specifications of the interaction counter.

scintillator	
manufacturer	Bicron
type	BC-408, PVT base (plastic)
light output	64 % Anthracene
max. emission wavelength	425 nm
decay constant	2.1 ns
bulk light attenuation length	380 cm
refractive index	1.58
H/C ratio	1.104
density	1.032 g/cm^3
softening point	70°C
thickness	2mm
active area covered	40×40mm^2
reflector	aluminum foil
light guide	
material	standard plexi glass
geometry	twisted
total length	176 mm
photomultiplier tube	
manufacturer	Hamatsu
type	R-1450 sealed in H3167 package
photocathode	$^3/_4$" (19mm) 10-stage head-on bialkali
package specs	24.6mm diameter $\times$ 140mm length
max supply voltage	–1800 V
bleeder current	0.47mA
anode pulse rise time	1.8 ns
electron transit time	19 ns
transit time spread	760 ns

5

Data Analysis

During the 1996/97 run 215 million events taken with the hadron–electron elastic scattering trigger have been written to tape. Less than 0.2 % of this data sample were expected to be true elastic Σ^--electron events (section 5.1, below). Therefore the strategy for processing the data was to focus on efficient rejection of background events (section 5.2) before an in-depth analysis (section 5.3) was attempted.

5.1 Expected event rates

The number of Σ^--electron elastic scattering events N_{el} to be expected at 100 % total efficiency can be estimated from the number of beam triggers N_{beam}, the total Σ^--electron elastic scattering cross section σ_{el}, and the electron density in the targets:

$$\frac{N_{el}}{N_{beam}} = \sigma_{el} \cdot \frac{Z}{A} N_A \cdot \rho \cdot l \tag{5.1}$$

The total cross section can be calculated by integrating equation (2.25). For 650 GeV/c beam energy, a mean squared radius of $\langle r^2 \rangle = 0.55$ fm^2, and $0.02 \leq Q^2 \leq 0.211$ GeV$^2/c^2$ one obtains

$$\sigma_{el} = 3.98 \mu\text{barn}. \tag{5.2}$$

In addition to the five targets made of either copper or diamond, scintillators located in the target region also can be considered effective targets (Fig. 5.1). Since the pureness of target material is of no concern in this investigation, events which have their vertices within these counters were included in the analysis. The parameters of the effective targets are listed in Table 5.1.

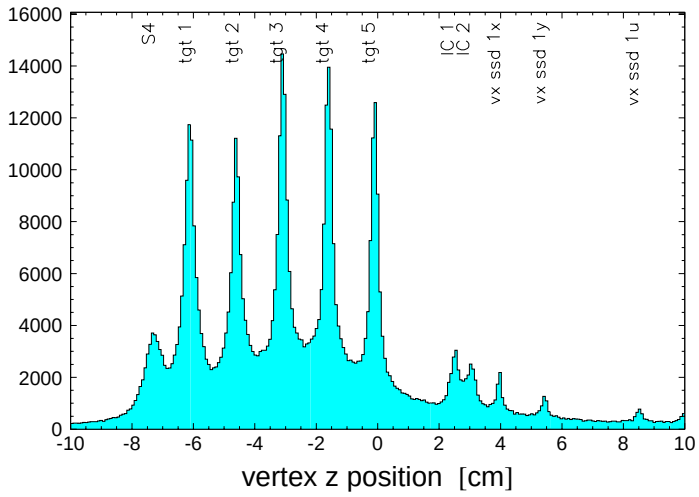

Figure 5.1: Material in the target region can be visualized by means of the z-positions of interaction vertices. In this sample of 2-prong events scintillators, targets, and the first three planes of vertex silicon detectors can be distinguished (cf. Fig. 3.4 on page 27).

Table 5.1: Parameters of the effective targets. l - length in z-direction, ρ – density, Z – atomic number, A – atomic mass.

target	material	l [cm]	ρ [g/cm^3]	Z/A [mol/g]
S4	PVT	0.16	1.032	0.563
target 1	Cu	0.16	8.96	0.456
target 2	Cu	0.1016	8.96	0.456
target 3	C	0.22	3.23	0.500
target 4	C	0.22	3.23	0.500
target 5	C	0.22	3.23	0.500
IC 1	PVT	0.20	1.032	0.563
IC 2	PVT	0.20	1.032	0.563

With Avogadro's number $N_A = 6.022 \cdot 10^{23}$ mol^{-1} the fraction of Σ^- -electron events becomes

$$\frac{N_{el}}{N_{beam}} = 5.89 \cdot 10^{-6} \tag{5.3}$$

The number of beam triggers can be estimated from the ratio of T0 triggers (beam trigger and ready state of the apparatus) to gated beam (a logical pulse corre-

sponding to a beam particle), which was typically 15 %. The total gated beam count for all runs with h-e trigger equals $4.93 \cdot 10^{11}$. Assuming that 50 % of the beam are Σ^- , the maximum event count to be expected at 100 % total efficiency would be

$$N_{el} \approx 2.1 \cdot 10^5 \tag{5.4}$$

This number is reduced by the geometrical acceptance and trigger and reconstruction efficiencies.

5.2 Data reduction

Assuming an average processing time of 70 ms per event it would take 175 days – almost half a year – to go through 215 million events only once.

Background events were stripped off from the complete data sample in three passes. Stripping means an event is partially reconstructed so it can be tested against certain rejection criteria.

The different stages are summarized in Table 5.2 on the following page and described in detail in the following sections.

The data was processed using the SELEX Offline Analysis Package (SOAP) which handles event unpacking, track and vertex reconstruction, and particle identification. This software package was in a development stage throughout this analysis, and the choice of strip criteria partially reflects the status of SOAP at that time.

The general strategy for track reconstruction was to find straight track segments within the individual spectrometers first, and then link these together.

5.2.1 Strip 1

The first pass over the complete data sample (Strip 1) was designed to reject 90 % of the background at a modest processing time. As a compromise, the strip criteria required unpacking only part of the event, particle identification from TRDs, and tracking in the beam, vertex, M1, and M2 spectrometers.

The cuts concentrated on the M2 spectrometer which was already in reasonably good shape in terms of tracking efficiency at the time Strip 1 was performed. The efficiency of linking M2 to vertex track segments, on the other hand, was far too low.

An event passed if it met all of the following conditions:

1. The correct trigger bit was set.

2. The event could be unpacked without errors.

Table 5.2: The different stages of data reduction. Numbers shown are for Σ^- events only, in percent of total h-e trigger events.

	description of cuts	events
	strip 1	
1	correct trigger bit	100.0 %
2	no unpack errors	96.7 %
3	minimum no. of hits in beam, vertex, and M2	83.9 %
4	beam particle identified as baryon	40.3 %
5	at least one electron signal from ETRD	8.9 %
6	$\geq$ 2 M2 tracks or one M1-M2 track plus at least one more M1 track	7.1 %
7	$\geq$ 2 M2 tracks or one M1-M2 track with negative slope	5.1 %
8	no positive-slope vertex-M2 tracks	4.4 %
9	at least one beam track can be reconstructed	3.5 %
10	interacting beam track can be identified	3.4 %
	strip 2	
11	$\geq$ 2 vertex tracks, at least one linked to a negative-slope M1/M2 track	3.2 %
12	interacting beam track forms a vertex with $\geq$ 2 tracks that passed above condition	1.1 %
13	the vertex is two-prong	0.7 %
	strip 3	
14	coplanarity of all tracks in vertex	0.06 %
15	one and only one of the scattered-particle tracks can be identified as electron	0.03 %
16	nonzero beam momentum, beam track originates in hyperon production target	0.02 %
17	momentum	0.017 %
18	acceptance	0.013 %
19	kinematics	0.006 %

3. Beam, vertex, and M2 spectrometers each had a minimum number of hits:

   - beam silicon: at least 7 hits needed for one track
   - vertex silicon: at least 20 hits for two tracks
   - M2 PWCs: at least 25 hits for two tracks (Fig. 4.3 on page 49).

4. The beam particle was identified by the BTRD either as pion or baryon.

5. At least one of the event's tracks could be identified as electron from ETRD information. For Σ^- data, an electron was required to have less than 250 GeV/c momentum. This corresponds to $Q^2_{max} = 0.256$ GeV$^2/c^2$.

6. There were at least two M2 tracks or one M1-M2 track plus at least one more M1 track

7. At least two of the M2 tracks or the M1-M2 track had negative slope (i.e. the particles carried negative charge).

8. There were no positive-slope vertex-M2 tracks. A positive track originating in the targets indicates an event with three or more tracks leaving the vertex. The earlier trigger versions (section 4.2) allowed events of this category to pass, i.e. there had to be at least two negative tracks as well.

9. At least one beam track could be reconstructed.

10. The interacting beam track could be identified by one of the following criteria:

    - The event contained one and only one beam track.
    - One of the beam tracks could be matched to hits in the HST silicon (cf. section 3.2.2). Since these detectors were cleared after only 100 ns they were likely to have recorded only the one beam track which had actually led to a trigger.
    - Two vertex-M2 tracks could be identified. If they form a vertex, the interacting beam track can be identified later.

    This cut was removed for runs where the HST silicon was known to be too inefficient, and for data stripped in Heidelberg.

5.2.2 Strip 2

The purpose of the second stage of data stripping was to extract all events with two-prong vertices from the Strip 1 data sample. Strip 2 was redone after major

improvements in vertex tracking and vertex identification. The Strip 2 requirements were:

11. At least two good tracks in the vertex spectrometer: either

    - two negative-slope vertex-M2 tracks *or*
    - one vertex-M1 and one vertex-M2 track, both with negative slope (this allowed Σ^- decay candidates to pass) *or*
    - two good vertex segments found by track search in the vertex silicon starting from the identified interacting beam track.

12. The event has a vertex. Vertex identification involved two steps: the distance of closest approach (dca) between all combinations of vertex track segments and beam tracks was calculated. A combination with a dca of less than 100 μm was tagged as a candidate. In this process the interacting beam track identification could be redefined if no vertex could be found involving the previously tagged beam track. The coordinates of the candidate were used as starting point for the SOAP vertex package which conducted its own search for vertices and performed a χ^2 fit for the vertex, taking into account multiple Coulomb scattering errors [77].

13. The identified vertex is of two-prong type (one beam track in – two tracks out).

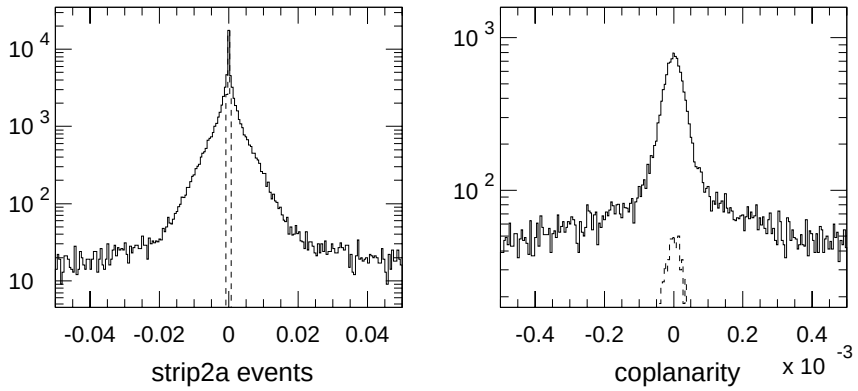

Figure 5.2: Coplanarity check: triple vector product for strip 2 events (left; dashed line indicates cut) and distribution of cut survivors (right; dashed line indicates kinematics cut).

5.2.3 Strip 3

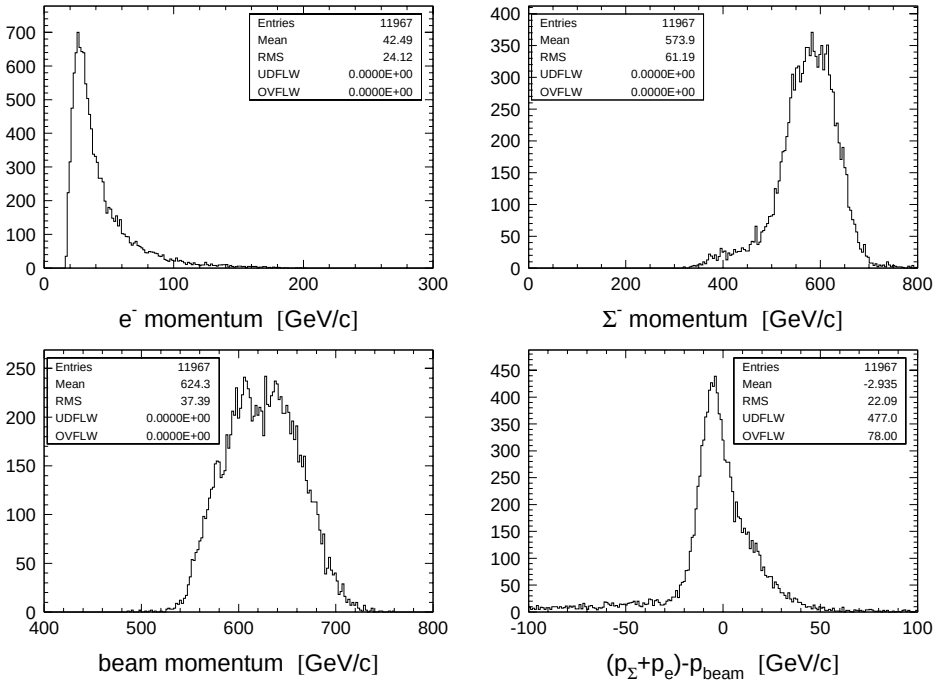

Figure 5.3: Distribution of electron, Σ^- , and beam momenta and elasticity for the final data sample. The shape of the elasticity peak reflects electron Bremsstrahlung losses on one hand (momentum sum less than zero) and a broad Σ^- momentum resolution on the other.

The last stage of data stripping tested the sample of two-prong events for physical relations that had to be true if the event actually resembled elastic scattering.

14. The three tracks forming the vertex were required to be coplanar. For an elastic process, conservation of momentum forces beam as well as scattered hyperon and electron tracks to be in one common plane, i.e. the scattering angles with respect to the beam track have to add up to the angle between the scattered-particle tracks. Coplanarity was tested by requiring the triple vector product of the normalized three-momentum vectors to be less than $0.5 \cdot 10^{-3}$ (Fig. 5.2):

$$\left| \frac{\vec{p}_\Sigma{}' \times \vec{p}_e{}'}{|\vec{p}_\Sigma{}' \times \vec{p}_e{}'|} \cdot \frac{\vec{p}_\Sigma}{|\vec{p}_\Sigma|} \right| < 0.5 \cdot 10^{-3} \tag{5.5}$$

15. One and only one of the two scattered tracks could be identified as electron, either by

- ETRD information, which implicitly required the electron track to have a M2 segment *or*
- if the scattering angle permitted an unambiguous assignment under the hypothesis of a Σ^--electron scattering. If the scattering angle was greater than 0.48 mrad the track was considered to resemble an electron.

16. The momentum of the beam track could be calculated, *and* the beam track originated from the hyperon production target. This requirement combined with the implicit prerequisite of level 14 that both scattering angles are available ensured that Q^2 could be calculated using at least the beam momentum and the scattering angles.

5.3 Analysis of the filtered sample

5.3.1 Final cuts

To separate background that had survived all three stages of data stripping the data was tested using the kinematic relations listed in section 2.2.1. In principle, if both scattering angles fit into the $\theta_e - \theta_\Sigma$ correlation and the angle–momentum relations are matched for both particles at the same time, the identification of the event as elastic Σ^--electron scattering is complete. However, the errors of scattering angles and momenta have to be sufficiently small. This was not the case at the time this analysis was performed. Cuts on kinematic relations were limited to the variables with the lowest errors.

The resolutions of the variables needed for calculating Q^2 were estimated with the help of Monte Carlo simulations described in section 5.3.3. The status of the offline analysis software at the time of this investigation did not allow for a reliable determination of momenta above approximately 300 GeV/c . Therefore, the four-momentum transfer squared could not be calculated from the scattered-Σ^- momentum. The angular resolution in the vertex spectrometer of 40 μrad was not good enough to include the Σ^- scattering angle in the analysis. The electron momentum, on the other hand, could be measured to better than 0.5 % in the M1 and M2 spectrometers. However, there is considerable energy loss due to Bremsstrahlung in targets and silicon detectors (the 20 planes of vertex silicon detectors already contribute 6.4 % of a radiation length) so the measured electron momentum does not resemble the electron momentum at the interaction vertex.

Q^2 could, however, be calculated from the scattering angle of the electron with

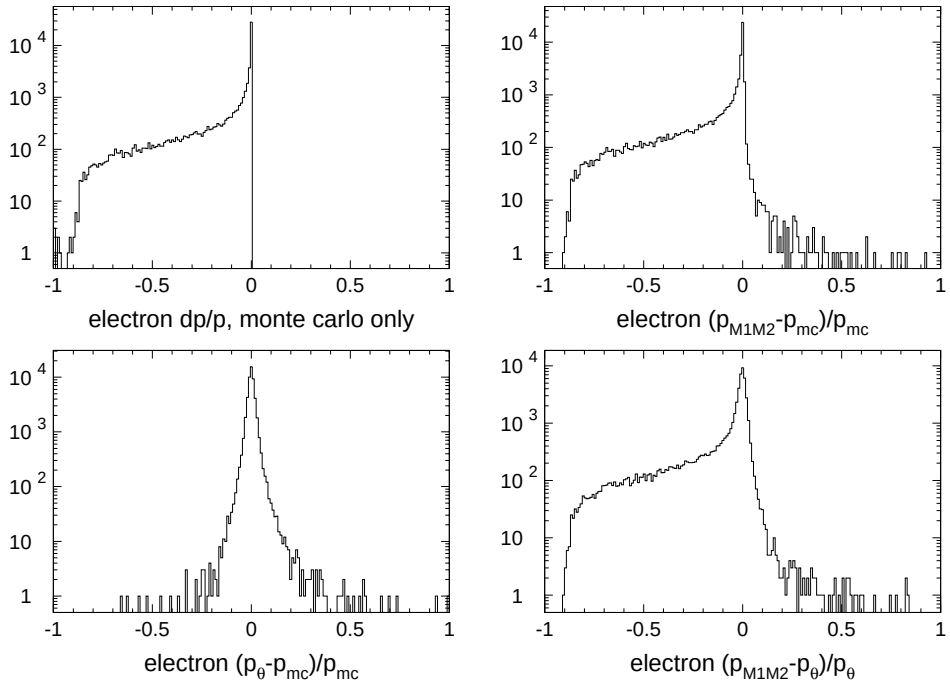

Figure 5.4: Monte Carlo study of Bremsstrahlung losses for the electron momentum. Bremsstrahlung was simulated for the targets and all material in the vertex spectrometer (upper left). The electron momentum measured in the M1/M2 spectrometers (upper and lower right) reflects these losses while the momentum calculated from the scattering angle is not affected (lower left).

a resolution of 1.5 %:

$$Q^2 = \frac{2E_\Sigma |\vec{p}_e\,'| m_e \cos\theta_e}{E_\Sigma + m_e}, \tag{5.6}$$

where the electron momentum is calculated from beam momentum and electron scattering angle:

$$|\vec{p}_e\,'(\theta_e)| = \frac{E_\Sigma m_e + m_e^2}{E_\Sigma + m_e - |\vec{p}_\Sigma| \cos\theta_e}. \tag{5.7}$$

The final cuts applied to the data sample checked for consistency of the kinematic relations involving θ_e within their errors:

17. The electron track was required to be inside the geometrical acceptance of the M2 spectrometer. This corresponds to a scattering angle of less than 8 mrad. The allowed region for the vertex was limited to -10 cm $< z <$ 10 cm.

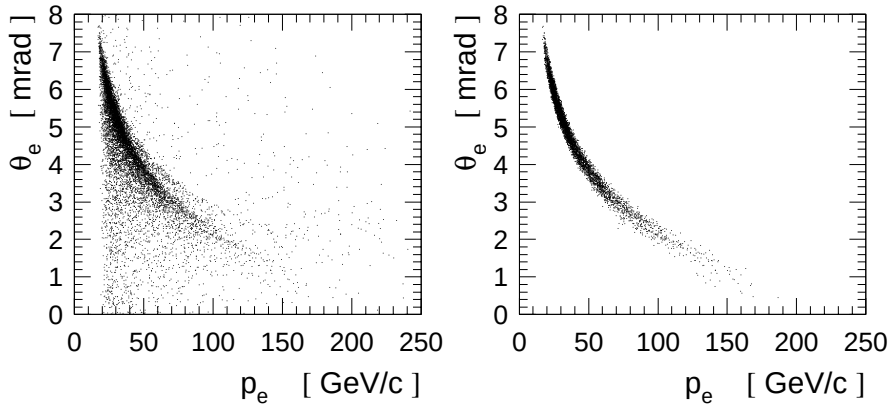

Figure 5.5: Distribution of electron scattering angle versus momentum, before (left) and after kinematics cut (right).

18. The scattered Σ^- momentum had to carry more than 60 % of the beam momentum

$$\frac{|\vec{p}_\Sigma{}'|}{|\vec{p}_\Sigma|} > 0.6. \tag{5.8}$$

This cut essentially threw out all events where the Σ^- decayed upstream of the M2 chambers. The resolution for high-momentum particles was not sufficient at the time of this analysis to place hard cuts on elasticity using the measured momenta (Fig. 5.3 on page 69).

19. The electron momentum $|\vec{p}_e{}'|$ as measured in the M1/M2 spectrometers had to match the momentum calculated from the electron scattering angle $|\vec{p}_e{}'(\theta_e)|$ within a 10 % tolerance (Fig. 5.5). It was decided to apply a symmetric cut rather than allowing for $|\vec{p}_e{}'| < |\vec{p}_e{}'(\theta_e)|$ because the error in $|\vec{p}_e{}'(\theta_e)|$ was estimated to be at the order of 1.5 % which is already larger than the Bremsstrahlung loss for more than 80 % of the events (Fig. 5.4 on the page before). Monte Carlo studies showed that the errors assigned to the momentum calculated from the scattering angle underestimate the real error with respect to the true momentum at the vertex (Fig. 5.13). Since the error in the angle is calculated from the fit errors of the vertex track segments, multiple Coulomb scattering in the targets is not taken into account (Fig. 5.12).

11,967 events remained which matched the kinematic relations (figs. 5.5 and 5.8). Both vertex resolution (Fig. 5.9) and Q^2 distribution (Fig. 5.7) indicate

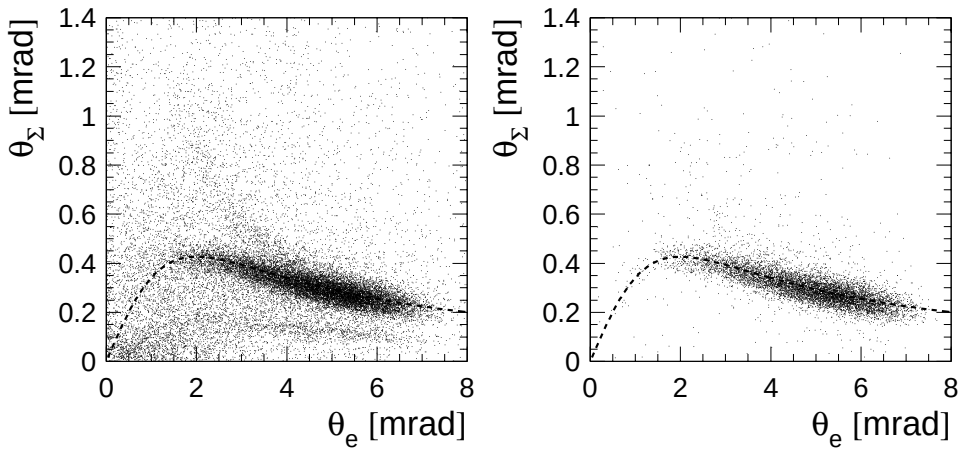

Figure 5.6: Correlation of Σ^- and electron scattering angles before (left) and after the kinematics cut was applied (right).

that the signal-to-background ratio is significantly improved by the final cuts. The remaining background is visible at Q^2 close to its maximum (Fig. 5.7, lower right). The number of events where $Q^2/Q^2_{max} > 0.8$ is by a factor of four higher than the Monte Carlo prediction for this interval (see discussion at the end of section 5.3.4).

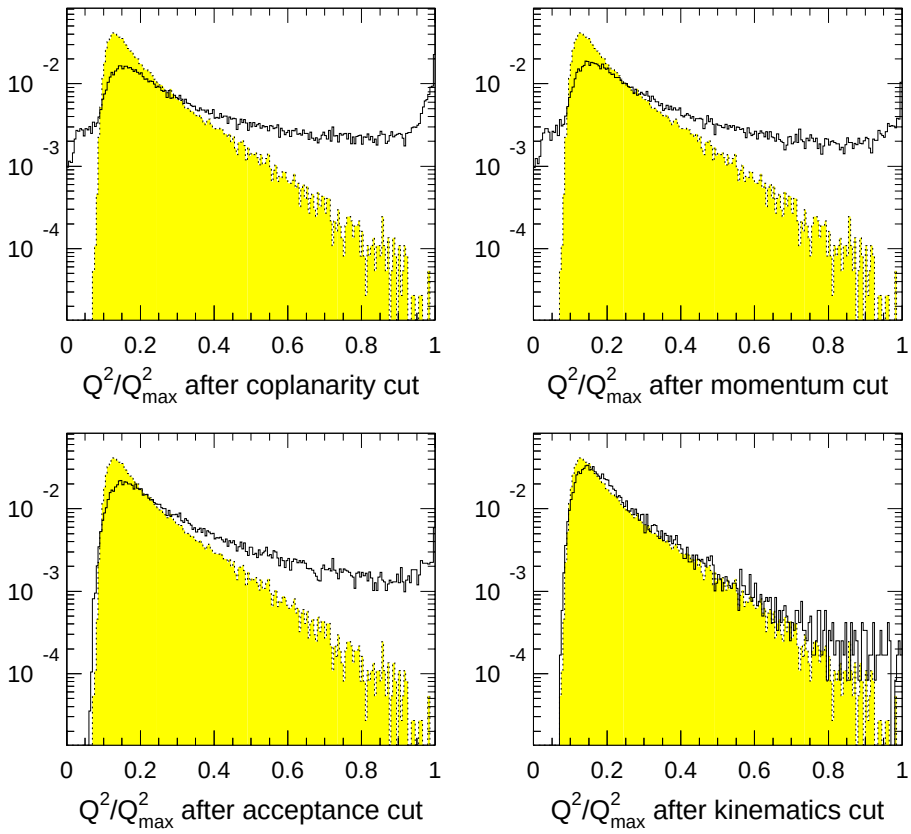

Figure 5.7: Effect of the final cuts on the Q^2/Q^2_{max} distribution. Shaded area: Monte Carlo generated events for $\langle r^2 \rangle = 0.55\,\mathrm{fm}^2$. Solid line: real data. By plotting the Q^2 distribution normalized to Q^2_{max}, background in the data which otherwise is smeared out by the beam spread can be made visible. The Q^2/Q^2_{max} distribution should follow the shape of the differential cross section (Fig. 2.4 on page 14).

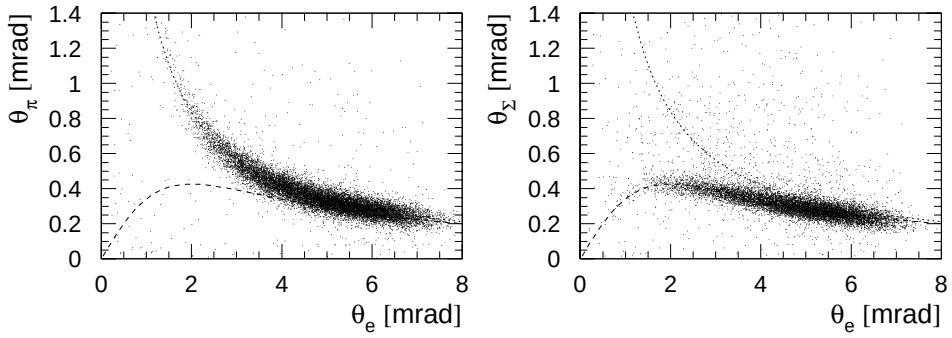

Figure 5.8: The angular correlation for π^- - (left) and Σ^--electron scattering (right). The dashed lines indicate the correlations at average beam momentum.

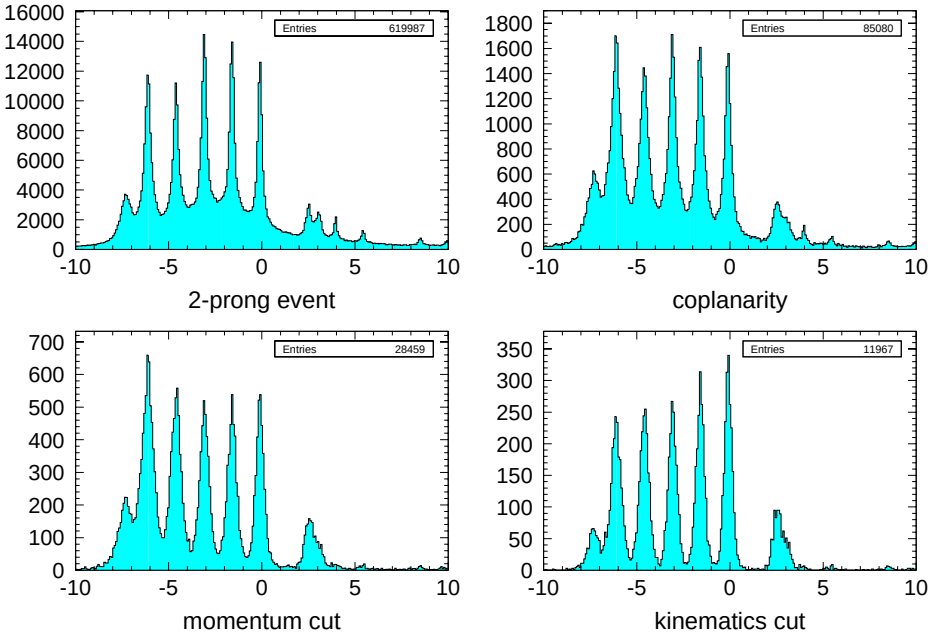

Figure 5.9: Effect of selected cuts on the vertex resolution.

5.3.2 Radius fits

From the final data sample, Q^2 and beam momentum were extracted for every event. The distribution of Q^2 was expected to resemble the differential cross section (2.25) in shape but not normalization, with Q^2 dependent acceptance corrections ϵ applied:

$$\frac{d\sigma}{dQ^2} = \frac{4\pi\alpha^2(\hbar c)^2}{Q^4}\left(1 - \frac{Q^2}{Q^2_{max}}\right) F^2(Q^2)\cdot\epsilon(Q^2) \tag{5.9}$$

The steep slope of the cross section does not allow a binned fit procedure since the average of a bin would be assigned to a Q^2 value which corresponds to the center of the bin instead of its center-of-gravity. This effect could be avoided by reducing the bin size to the effective Q^2 resolution of 2 %. However, this would cause high-Q^2 bins to have high statistical error and consequently lower weights in the fit. Since the high Q^2 region is of significance for the determination of the radius a binned approach is not suitable.

An unbinned maximum likelihood method was employed to fit the radius.

The principle of this method is to maximize the likelihood $\mathcal{L}(a)$ of the hypothesis that the parameter a – which represents the radius – takes on a certain value. The likelihood is defined as the product of the probability densities $y_i(x,a)$ (representing the differential cross section values calculated for the individual $(Q^2,|\vec{p}_\Sigma|)$ data points),

$$\mathcal{L}(a) = \prod_{i=1}^{n} y_i(x,a), \tag{5.10}$$

which requires the y_i to be normalized:

$$\int y_i(x,a)dx = 1. \tag{5.11}$$

Instead of calculating the product of many small numbers y_i it is more convenient to evaluate the logarithm of the likelihood function

$$\ell = \log\mathcal{L} = \sum_{i=1}^{n} \log y_i. \tag{5.12}$$

For large numbers n of events, $\mathcal{L}(a)$ is a Gaussian distribution in the vicinity of its maximum where $a = a_0$:

$$\mathcal{L} \sim e^{-(a-a_0)^2/2\sigma^2}. \tag{5.13}$$

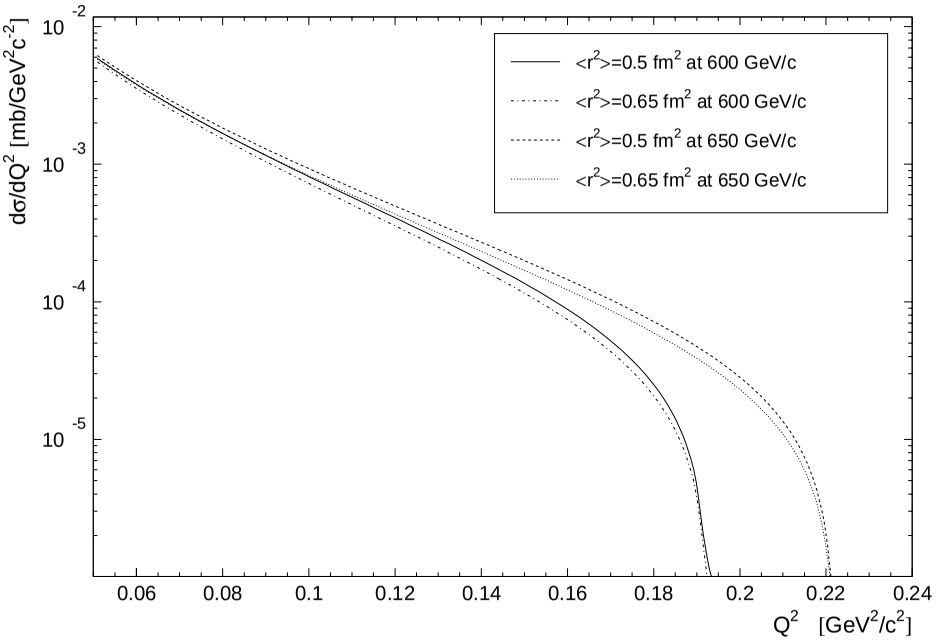

Figure 5.10: Ambiguity of the differential cross section when both mean squared radius and beam momentum are free parameters. In this example, the cross section is plotted for $\langle r^2 \rangle = 0.5\,\mathrm{fm}^2$ and $\langle r^2 \rangle = 0.65\,\mathrm{fm}^2$ at 600 and 650 GeV/c , respectively. For $Q^2 < 0.1\ \mathrm{GeV}^2/c^2$ the radii cannot be distinguished unless the beam momentum is known.

Then ℓ is a parabolic function of the parameter a and the error in a can be defined as the root mean square deviation of the $\mathcal{L}(a)$ distribution about its mean a_0, which has an equivalent for ℓ [78]:

$$\sqrt{\langle \mathcal{L}(a)|_{a_0} \rangle} = \left(-\frac{\partial^2 \ell}{\partial a^2}\bigg|_{a_0} \right)^{-1/2}. \tag{5.14}$$

If the likelihood distribution is not Gaussian, one can define an asymmetric error. The quantities in Eqn. (5.14) are equivalent to the change in a required to reduce ℓ from its maximum value by 0.5:

$$\ell(a_0 \pm \delta a) = \ell(a_0) - \frac{1}{2} \tag{5.15}$$

If two values a_1,a_2 can be found such that

$$\ell(a_i) = \ell(a_0) - \frac{1}{2}, \quad i = 1, 2 \tag{5.16}$$

then the range of parameters

$$a_1 \leq a \leq a_2 \tag{5.17}$$

still contains the true value of the parameter to 68 % probability [78].

The considerable spread of beam momentum (Fig. 3.10) leads to a distortion of the radius since, within the statistical error of the data point, the differential cross section for one value of radius and beam energy can be matched by the cross section for a smaller (larger) radius at higher (lower) beam energy (Fig. 5.10).

This effect was eliminated by an event-by-event normalization. The differential cross section for each $(Q^2,|\vec{p}_\Sigma|)$ point was normalized to

$$\frac{d\sigma}{dQ^2}^{(norm)} = \frac{d\sigma}{dQ^2} \cdot \left(\int_{Q^2_{min}}^{\lambda Q^2_{max}} \frac{d\sigma}{dQ^2} dQ^2 \right)^{-1} . \tag{5.18}$$

The upper limit of the integral was given by a fraction λ of ${Q^2}_{max}$ where λ was constant for all data points.

The integration has to be performed only once if the cross section is corrected for its deviation from the cross section at equal Q^2 but fixed beam momentum (for example, the average beam momentum of the sample):

$$\frac{d\sigma}{dQ^2}^{(fix)} = \frac{d\sigma}{dQ^2} \cdot \frac{Q^2_{max}}{Q^{2\,(fix)}_{max}} \cdot \frac{(Q^{2\,(fix)}_{max} - Q^2)}{(Q^2_{max} - Q^2)} \cdot \frac{F^{2\,(fix)}(Q^2)}{F^2(Q^2)} \tag{5.19}$$

5.3.3 Resolution and acceptance studies

Both angular and momentum resolutions as well as the geometrical acceptance and Q^2 dependences of trigger, reconstruction, and cuts were studied by embedding Monte Carlo generated events in real data.

The procedure was to reconstruct all tracks in a real event, then remove all hits that had been linked to tracks except for the beam tracks, and generate a Σ^- - electron elastic scattering event on top of this event. Remaining noise hits could be left in the sample or removed to study their influence on track reconstruction efficiency. The Q^2 distribution could be generated either according to a differential cross section of the type discussed in section 2.2.2, or as a flat distribution. The lower Q^2 cutoff and the mean squared radius could be varied. The package also simulated multiple Coulomb scattering effects and Bremsstrahlung losses.

Resolutions

Angular and momentum resolutions and their effect on the Q^2 resolution were studied by comparing the generated values with the reconstructed ones. Results are shown in Fig. 5.11. The momentum resolution was found to be better than 0.5 % for low momentum tracks. For momenta above 300 GeV/c , however, the resolution is only of the order of 5 %. In addition, for a significant fraction of events the momentum measurement is off by more than 50 %. An angular resolution of 41 μrad in the vertex spectrometer was determined.

The electron angle was calculated from the beam and vertex track segments. The fit errors for these segments take into account multiple Coulomb scattering in the silicon detectors but not in the targets. They tend to underestimate the real error (Fig. 5.13 on page 81). A realistic evaluation of the error of the electron angle would require that the track segment be refitted with the vertex coordinates included. For this analysis, the resolution as estimated by the Monte Carlo study was used instead.

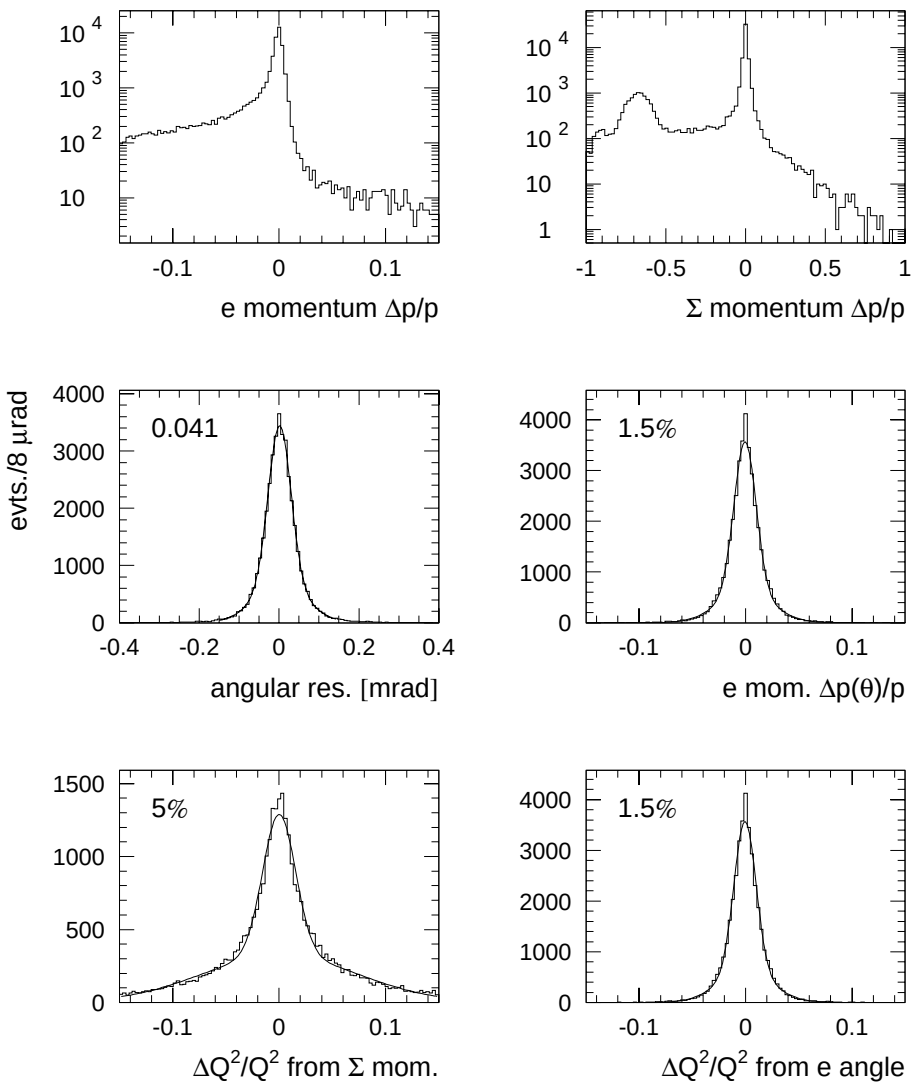

Figure 5.11: Monte Carlo calculation of the momentum, angular, and Q^2 resolution. Top row: The electron momentum is measured in the magnets to better than 0.5 %, however there can be considerable Bremsstrahlung losses. For part of the events the Σ^- momentum is off by more than 50 % (upper left). – Center row: An angular resolution of 41 μrad was calculated. From beam momentum and electron scattering angle, the electron momentum is determined to 1.5 % accuracy. – Bottom row: If the events off by 50 % are excluded, Q^2 can be calculated from the Σ^- momentum with an estimated resolution of 5 % (upper right). If the electron momentum is calculated from beam momentum and electron scattering angle, a Q^2 resolution of 1.5 % is achieved (not including beam momentum uncertainty).

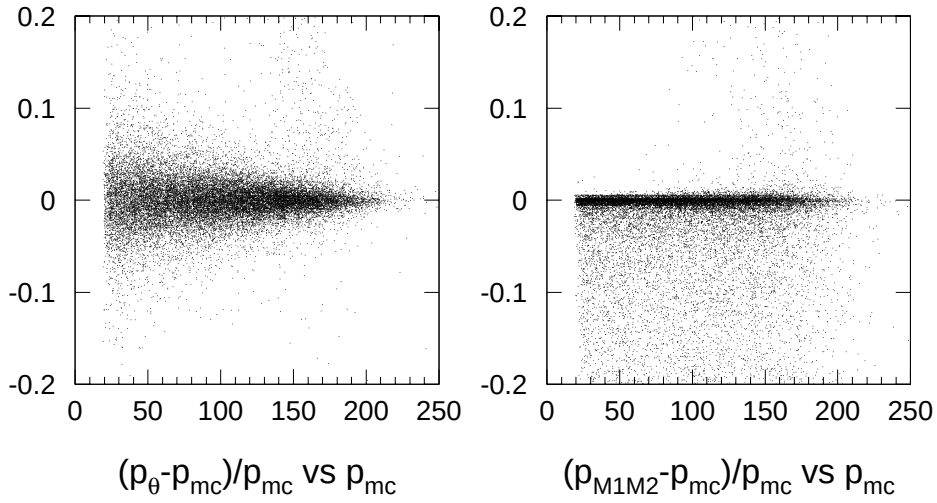

Figure 5.12: Monte Carlo study of the electron momentum measured in the M1/M2 spectrometers compared to the calculation from the scattering angle. The error of the latter is dominated by multiple Coulomb scattering effects which are momentum dependent (left) while Bremsstrahlung is not (right).

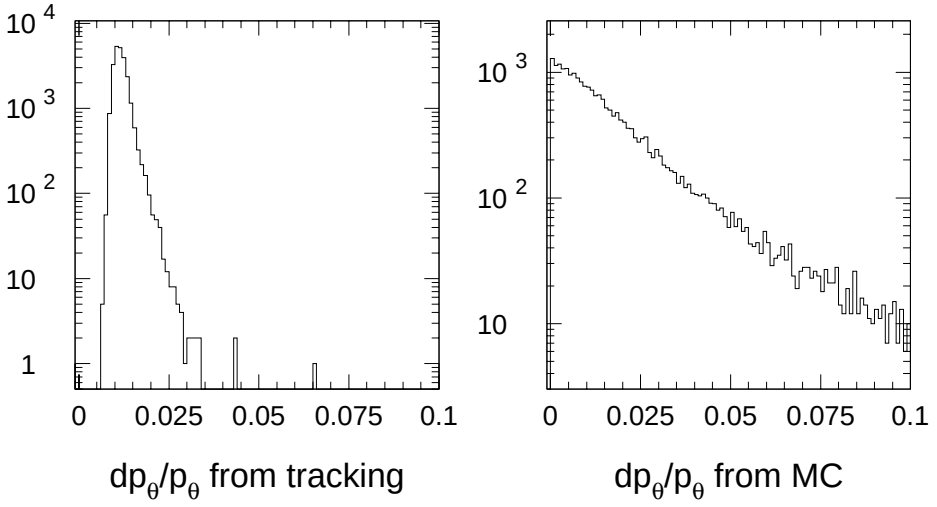

Figure 5.13: The $\vec{p}_e(\theta)$ error calculated from the track segment fit in the vertex silicon (left) does not include multiple Coulomb scattering in the targets and is therefore too small compared to the error determined from Monte Carlo (right).

Acceptance

The Q^2 dependence of the reconstruction and analysis code was studied by generating a flat Q^2 distribution. The binwise ratio of the final to the original sample yields the reconstruction efficiency including geometric acceptance (Fig. 5.16). The Q^2 dependence of the individual cuts was studied, and the cuts adjusted to keep this dependence minimal where possible (Fig. 5.14). The acceptance obtained from this study is Q^2-independent for $0.025 \leq Q^2 \leq 0.16$ GeV$^2/c^2$. At the low-Q^2 end the geometrical limit defined by the aperture of the M2 magnet causes the acceptance to drop to zero at $Q^2 = 0.02$ GeV$^2/c^2$. Towards high Q^2 the acceptance function displays a moderate negative slope. Since embedded Monte Carlo events get their beam momentum from real data, the statistics of this study are limited at high Q^2 by the momentum distribution.

Only two cuts in the analysis have significant Q^2 dependence:

- The rejection of the strip 1 cut on electron identification from the ETRD decreases almost linearly between the geometric cutoff at $Q^2 = 0.02$ GeV$^2/c^2$ and $Q^2 = 0.05$ GeV$^2/c^2$. This effect is attributed to low-momentum particles which did not pass through a sufficient number of ETRD planes to generate the minimum three clusters required for electron identification (cf. Fig. 3.16 on page 40).
- The cut on Σ^- which carry less than 60 % of the beam momentum increases with Q^2 above 0.15 GeV$^2/c^2$. This affects primarily events where either the Σ^- momentum determination was completely wrong (cf. Σ^- momentum resolution, plot at upper left in Fig. 5.11 on page 80) or only the momentum of the decay pion was measured. Both classes of events were targeted by the cut. The increased rejection at higher Q^2 is probably due to events where the Σ^- momentum was underestimated. The higher the fraction of the beam momentum carried by the electron under these circumstances, the more likely it is for an event to be rejected.

Trigger-related effects

The trigger efficiency was studied by including the measured efficiencies of `H1` counters and gaps between the hodoscope segments in the calculation. The effect of one hodoscope counter known to be highly inefficient was studied by assuming zero efficiency for this counter and 100 % for all others. The effect of gaps was studied by varying the gap size.

The inefficient counter causes a slight dip in the acceptance for $0.03 \leq Q^2 \leq 0.04$, which is actually seen in the data. The trigger efficiency drops off to both the low-Q^2 and high-Q^2 limits of the geometrical acceptance. Low efficiency towards

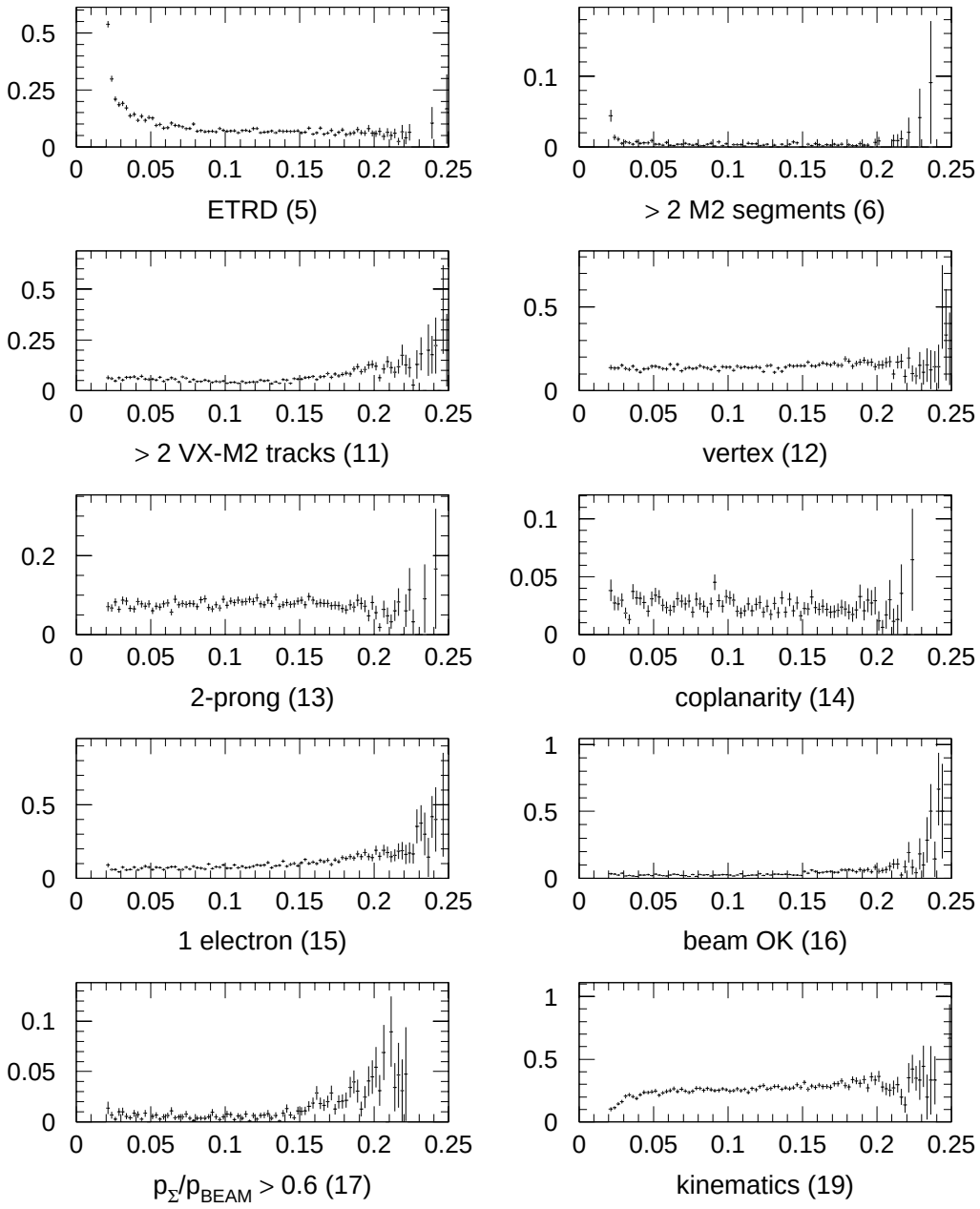

Figure 5.14: Q^2 dependence of various cuts. Plotted is the binwise fraction of events rejected in the cut versus Q^2 in GeV^2/c^2, starting from a flat Q^2 distribution. Numbers in title refer to cut as listed in section 5.2.

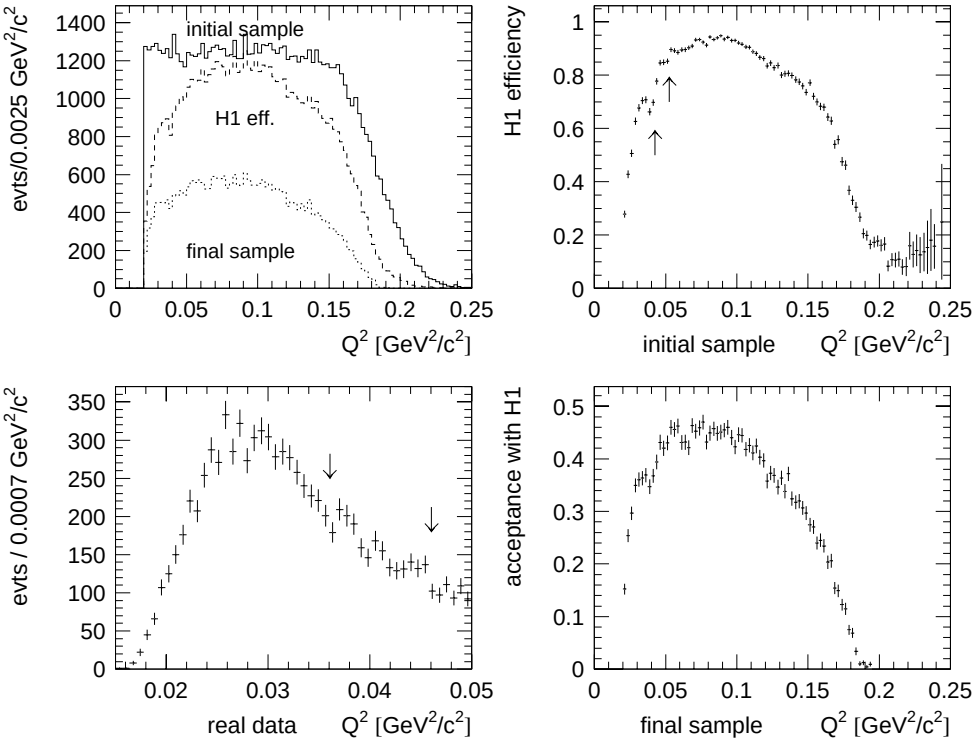

Figure 5.15: Monte Carlo study of trigger efficiency and its effect on the acceptance. The study was performed using a flat Q^2 distribution and the beam momentum distribution from real events (upper left). The trigger efficiency applied to the initial sample shows a dip between $Q^2 = 0.033 - 0.045$ which is attributed to an inefficient hodoscope counter (upper right, arrows). This effect is visible in the real data (lower left, arrows). The acceptance calculated from the cumulative effects of reconstruction and analysis cuts is mostly limited by the geometric acceptance. Its slope towards high Q^2 is steepened if the `H1` efficiency is included in the calculation (lower right).

low Q^2 is caused by the combined effect of the hodoscope's geometrical acceptance and electron Bremsstrahlung losses. Towards high Q^2 the trigger efficiency has a principal cutoff given by the border between the negative and central subhodoscopes ($\mathtt{H1}^-$ and $\mathtt{H1}^0$, described in section 4.2). Since the trigger did not allow more than one hit in the central subhodoscope, events where both electron and Σ^- passed through $\mathtt{H1}^0$ were suppressed. This effect is expected to be smeared out considerably, though, due to the fact that more than half of the Σ^- decay upstream of H1 and the pion may well have passed through $\mathtt{H1}^-$.

The noise of H1 being at the 20 % level, the simulation of the trigger as performed here can only be used to study the principal dependence of the acceptance on the trigger. Efficiencies calculated in this way reflect only the extreme situations but not the true quantitative effects on the data.

Acceptance corrections

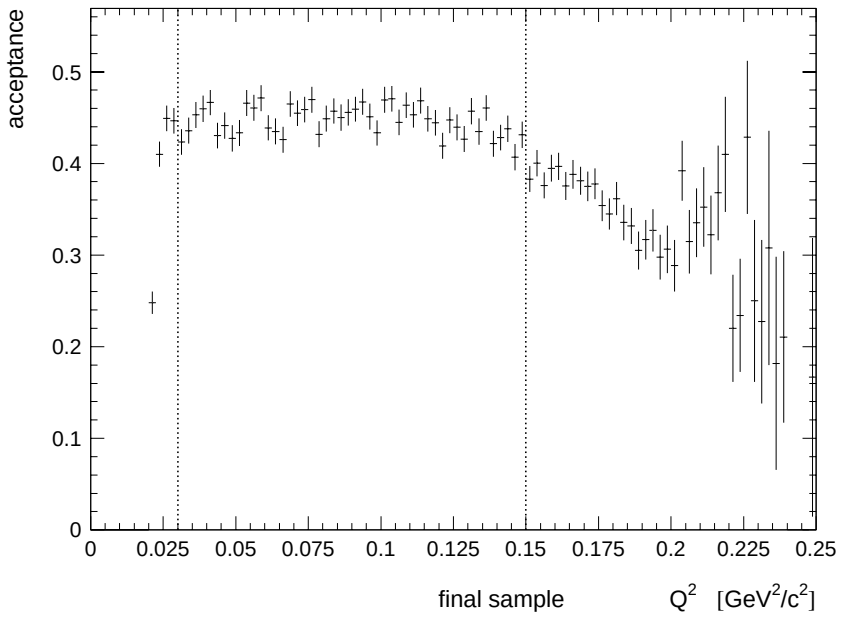

Figure 5.16: The acceptance of the reconstruction and analysis code (not including trigger efficiency). Dotted vertical lines indicate the lower and upper Q^2 limits of the fit range.

The total acceptance function $\epsilon(Q^2)$ in the Q^2 interval from 0.028 to 0.25 GeV$^2/c^2$ neglecting trigger efficiency can be approximated by a polynomial fit:

$$\epsilon(Q^2) = 0.2573 + 1.157\,Q^2 - 7.94\,Q^4 + 5.178\,Q^6. \tag{5.20}$$

The acceptance over the complete Q^2 range cannot be described by one polynomial.

The stability of fit results at varying Q^2 intervals was not improved by applying the correction (5.20) or any other function approximated to the acceptance. In particular, the flat part of the acceptance ($0.03 \leq Q^2 \leq 0.15$) coincides with Q^2 intervals which lead to stable results (Fig. 5.18 on page 88). Applying any function to the data which was not constant in this range worsened the consistency of the results. It must be concluded that the acceptance in this region is indeed independent of Q^2.

5.3.4 Statistical and systematic errors

Statistical significance of the fit

The statistical error of the radius fit as given by the likelihood calculation (Eqn. 5.14) was validated by a Monte Carlo study. A large number of independent samples of the approximate size of the final sample (7864 events) were generated for a constant value of the radius. The distribution of radii fit to these events should reflect only statistical fluctuations without any systematic errors. At the same time this provided a tool to verify the functionality of the software used.

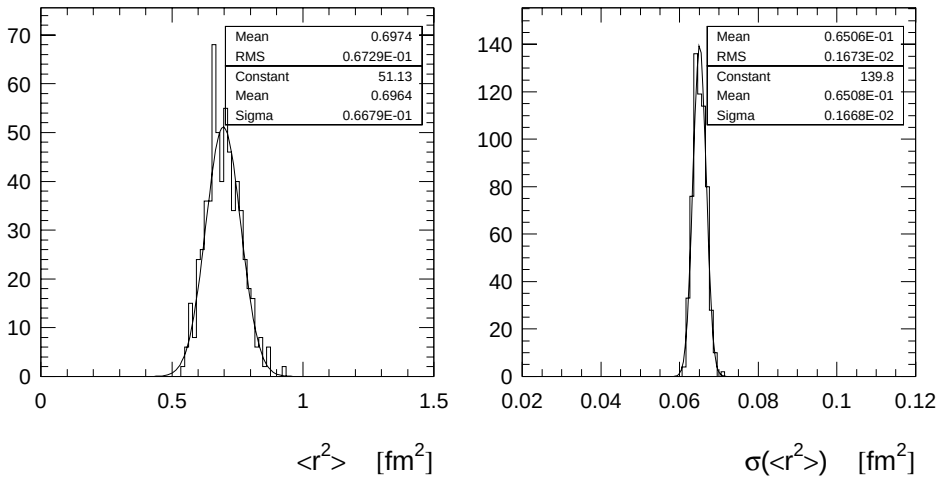

Figure 5.17: Distribution of fit results (left) and statistical errors (right) for 300 Monte Carlo samples generated with $\langle r^2 \rangle = 0.68\,\mathrm{fm}^2$. On average, each fit included 9350 events.

An example is shown in Figure 5.17. As expected, the distribution of radii is of Gaussian shape. Its statistical error agrees with the average of statistical errors calculated for the single fits. Therefore the statistical error of the best fit in (6.1) was determined by averaging the individual errors of each fit.

Systematic errors

The systematic error was evaluated by studying the Q^2 resolution, the acceptance (section 5.3.3), and the dependence of the radius on the lower and upper Q^2 limits used for the fit.

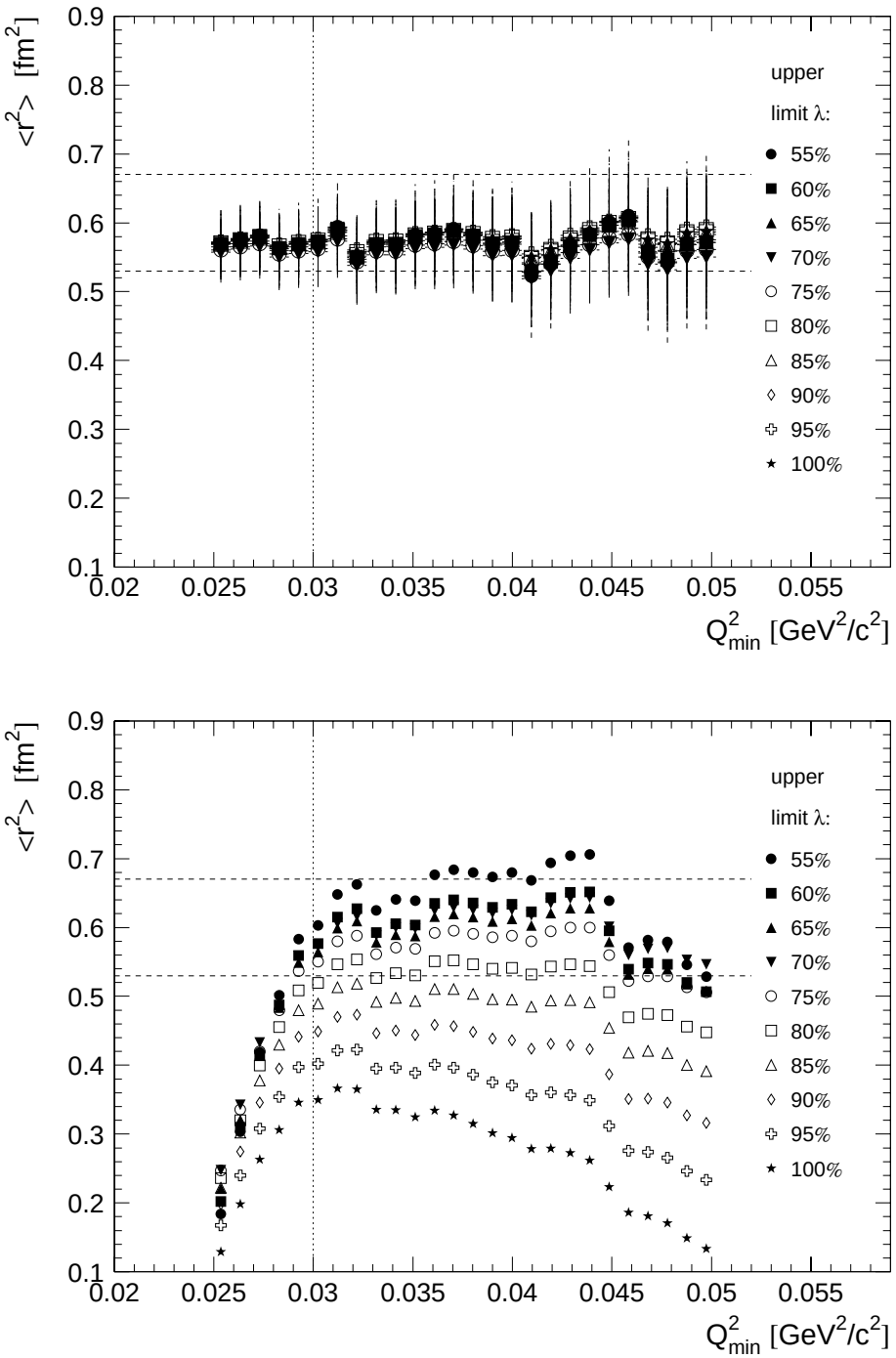

Figure 5.18: Dependence of the fit on the Q^2 range. Top: Monte Carlo events generated for $\langle r^2 \rangle = 0.60\,\mathrm{fm}^2$. Bottom: real data. The systematic error assigned to the result is indicated by horizontal dashed lines. Points to the left of the vertical dotted line ($Q^2_{min} < 0.03\ \mathrm{GeV}^2/c^2$) were not included in the systematic error studies. The lower Q^2 boundary is varied from 0.02 to 0.05 GeV^2/c^2. Distributions are shown for upper Q^2 limits between 50 % and 100 % of Q^2_{max}. No acceptance correction was applied in this plot.

The error in Q^2 is a function of the errors of electron angle and beam momentum. The Q^2 resolution was estimated by Monte Carlo studies (Fig. 5.11):

$$\frac{\Delta Q^2}{Q^2} = 1.5\,\%. \tag{5.21}$$

The effect on the radius was determined by fitting the sample after adjusting all data points by $\pm 1.5\,\%$:

$$(\Delta\langle r^2\rangle)_{angle} = 0.05\,\mathrm{fm}^2 \tag{5.22}$$

However, since Monte Carlo events were embedded in real data using the original beam tracks (cf. section 5.3.3) this does not include the error of the beam momentum measurement. The latter has been studied by reconstructing three-prong events where all three particles have momenta low enough to be correctly determined [57]. The study yielded a possible offset in the beam momentum of the order of 10 GeV/c . Adjusting the beam momentum by ± 10 GeV/c was found to shift the radius by

$$(\Delta\langle r^2\rangle)_{beam} = 0.04\,\mathrm{fm}^2. \tag{5.23}$$

The acceptance was found to be Q^2-independent in the interval $0.03 \leq Q^2 \leq 0.15$ GeV$^2/c^2$ (Fig. 5.16).

The systematic error of the fit was studied by varying the lower and upper Q^2 limits.

For a completely unbiased and backgroundless data sample the fit value for the radius has to be independent of the Q^2 range covered (Fig. 5.18, top). In real data (Fig. 5.18) there are some significant deviations:

(a) The radius decreases rapidly if the lower Q^2 limit is chosen below $0.029\,\mathrm{GeV}^2/c^2$. This effect reflects the limit of the geometrical acceptance.

(b) The radius also decreases steadily as the upper Q^2 limit is extended beyond 75 % of Q^2_{max}. This means the abundance of data at large Q^2 is higher than what would be expected from the distribution at lower Q^2. There are two possible reasons for this behavior:

- The overall efficiency increases towards Q^2_{max}. This is, however, contradicted by acceptance studies which suggest the opposite behavior (section 5.3.3, Fig. 5.16 on page 85).

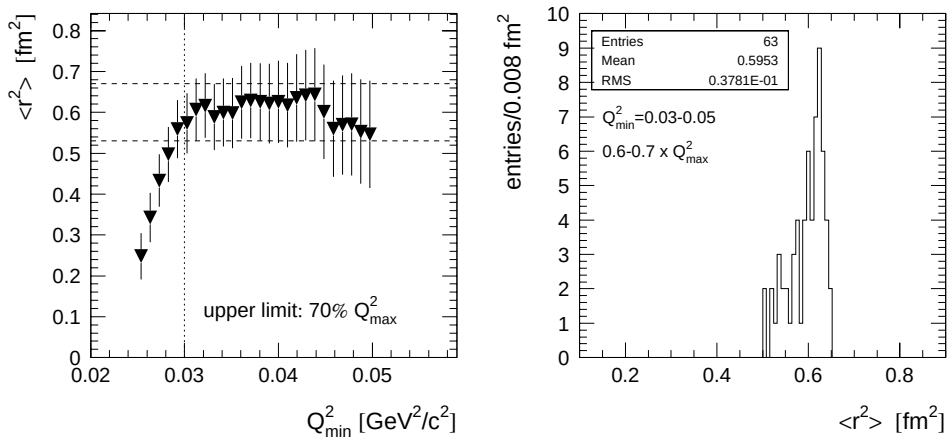

Figure 5.19: Left: Variation of the lower Q^2 limit at constant upper Q^2 limit of 70 % of Q^2_{max}. The systematic error assigned to the result is indicated by dashed horizontal lines. Points to the left of dotted vertical line ($Q^2_{min} < 0.03$) were not included in the systematic error studies. – Right: Fit results of the Q^2 range chosen for estimating the systematic error ($0.03 \leq Q^2_{min} \leq 0.05$ GeV$^2/c^2$ at 60%, 65%, and 70% of Q^2_{max}.

- The high-Q^2 region has a significant admixture of background events. While nothing can be said about the nature of this background or its Q^2 dependence, it is plausible that a constant background which contributes at the 0.1 % level for $Q^2 = 0.03$ GeV$^2/c^2$ will double the differential cross section at 80 % of Q^2_{max}.

The second argument is backed by the comparison of the Q^2 distribution to that of a Monte Carlo generated sample (Fig. 5.7 on page 74). The normalized ratio of real data to Monte Carlo events in a certain interval of Q^2/Q^2_{max} was calculated. The lower limit of this interval was increased while the upper boundary was always fixed at 1. The ratio of real data to simulated data increases dramatically as the lower boundary approaches $Q^2/Q^2_{max} = 1$ (Table below), whereas the acceptance studies suggest that it should actually drop towards zero.

Q^2/Q^2max	$0.2-1$	$0.7-1$	$0.8-1$	$0.9-1$
real/MC	1.1	2.5	3.6	7.6

(c) If the lower Q^2 limit is raised from 0.044 to 0.046 GeV$^2/c^2$ the radius drops by approximately 0.05 fm^2, regardless of the upper Q^2 limit. At this point a slight discontinuity is visible in the data which was reproduced in a trigger

study (fig 5.15 on page 84). It is caused by an inefficient counter in the first hodoscope.

(d) At $0.033 \leq Q^2_{min} \leq 0.036$ GeV$^2/c^2$ the radius is lower by approximately 0.01 fm^2 compared to adjacent values of Q^2_{min}. Again, this is true for all choices of Q^2_{max} and attributed to an inefficient counter of H1 .

(e) In spite of the dip described in (d), the results agree to better than ± 0.02fm^2 for $0.031 \leq Q^2_{min} \leq 0.044$ GeV$^2/c^2$ and an upper fit boundary between 60 % and 70 % of Q^2_{max}.

In conclusion, it can be said that the systematic error clearly depends on the the Q^2 range chosen for the fit. The uncertainties are dominated by the tendency towards small values of $\langle r^2 \rangle$ both at the low-Q^2 limit and as Q^2 approaches Q^2_{max}. While the first effect can be corrected by careful simulations of the acceptance and trigger efficiency, the high-Q^2 effect is caused by background events which are prevalent for $Q^2/Q^2_{max} > 0.7$. The uncertainty of the fit was estimated from the spread for the interval $0.03 \leq Q^2_{min} \leq 0.05$ at 60 %, 65 %, and 70 % of Q^2_{max} to

$$(\Delta \langle r^2 \rangle)_{fit} = 0.04\,\mathrm{fm}^2. \tag{5.24}$$

The Σ^- identification relied exclusively on the BTRD information which has an estimated π^- background of 2.2 to 6 % (page 38).

π^--electron events were suppressed in the analysis by requiring that one and only one of the scattered particles is identified as electron (cut 15, cf. section 5.2.3). High-momentum pions (more than 300 GeV/c) are identified as electrons by the ETRD (page 39). Low-momentum pions would have scattering angles larger than 0.48 mrad which is the maximum angle allowed for Σ^- . In this case the π^- would be tagged as electron. Since the real electron would have high momentum it would definitely be inside the acceptance of the ETRD and properly identified. The π^- contamination of the final sample is therefore only a function of the estimated 5 % ETRD inefficiency. The effect on the radius was tested by adding identified π^--electron elastic scattering events to the final sample. A fit of the combined Σ^-/π^- sample yielded a radius smaller by

$$(\Delta \langle r^2 \rangle)_{\pi} = 0.02\,\mathrm{fm}^2. \tag{5.25}$$

In addition, the BTRD cannot distinguish Σ^- and Ξ^- . The abundance of the latter in the beam is not known exactly, an upper limit of 4 % is assumed. For half of the Ξ^--electron elastic scattering events the decay took place downstream of the M2 chambers. In that case they are expected to have survived all cuts since the

kinematics are similar to Σ^--electron scattering. The maximum contamination of the final sample by Ξ^- events is therefore 2 %. As a first approximation the contribution to the systematic error was estimated by assuming the Ξ^- contamination to have an effect similar to a π^- contamination. This yielded a difference of less than

$$(\Delta\langle r^2\rangle)_\Xi = 0.01\,\mathrm{fm}^2 \tag{5.26}$$

in the radius.

The contributions from electron angle, beam momentum, fit systematics, and beam contamination were assumed to be uncorrelated. Added in quadrature they yield a total systematic error of

$$(\Delta\langle r^2\rangle)_{syst} = 0.08\,\mathrm{fm}^2. \tag{5.27}$$

6

Results and Discussion

6.1 The Σ^- charge radius

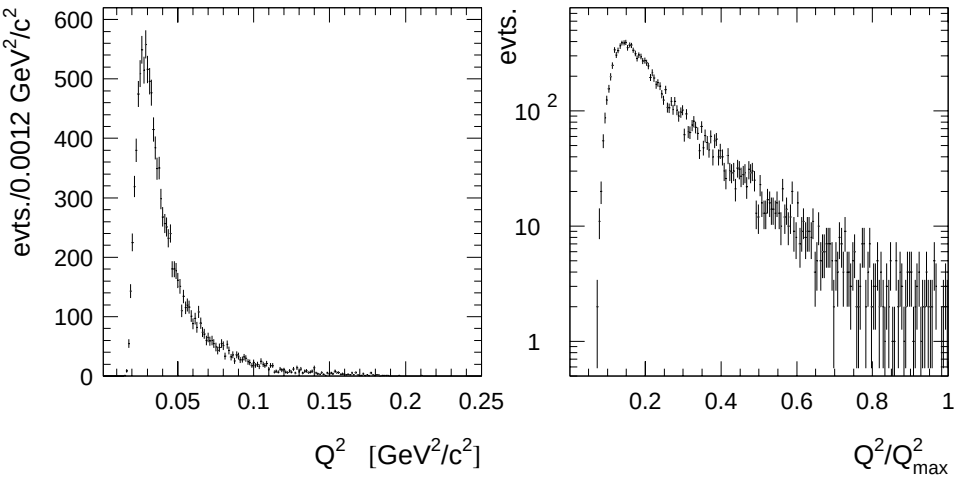

Figure 6.1: Q^2 distribution of the final sample (left) and the corresponding Q^2/Q^2_{max} distribution (right).

From the final sample described in section 5.3 (Fig. 6.1) the Q^2 range from 0.03 GeV$^2/c^2$ to $0.7 \cdot Q^2_{max}$ was chosen. Within this interval the acceptance is independent of Q^2 (Fig. 5.16 on page 85), and the fit results are independent of upper and lower Q^2 limits (section 5.3.4). Therefore, no acceptance correction was applied.

Inside this range the lower Q^2 limits were varied in steps of 0.001 GeV$^2/c^2$ and the upper limits in steps of 5 % of Q^2_{max} (Table 6.1). For each combination the radius was computed from a dipole fit (Eqn. (2.34)) to the Q^2 distribution using

an unbinned maximum likelihood method (section 5.3.2). The dipole fit included both electric and magnetic form factors (Eqn. (2.32)) which were assumed to be related to the mean squared radius as described in Eqn. (2.40). A magnetic moment of $\mu = -1.16\,\mu_N$ was assumed.

Out of this sample the average weighted by statistical error was considered the best estimate for the Σ^- charge radius:

$$\langle r^2 \rangle = 0.60 \pm 0.08\,(stat.) \pm 0.08\,(syst.)\,\mathrm{fm}^2. \tag{6.1}$$

The sample size for each combination of upper and lower boundaries varied between 7864 and 2746 events. The systematic error was evaluated from the distribution of fit results in this sample (cf. section 5.3.4) and the propagation of the Q^2 resolution as determined from Monte Carlo calculations (section 5.3.3).

The impact of magnetic contributions was studied by repeating the fit with the anomalous magnetic moment set to zero, i.e. $\mu = -1.0\,\mu_N$:

$$\langle r^2 \rangle_{\mu=\mu_N} = 0.59 \pm 0.08\,(stat.) \pm 0.08\,(syst.)\,\mathrm{fm}^2. \tag{6.2}$$

If the Dirac and Pauli form factors $F_1(Q^2), F_2(Q^2)$ (Eqn. (2.26)) are used instead of the dipole form, one obtains a radius $\langle r_1^2 \rangle$ related to the charge radius $\langle r^2 \rangle$ (Eqn. (2.42)) by

$$\begin{aligned} \langle r_1^2 \rangle &= \langle r^2 \rangle - \frac{3\kappa(\hbar c)^2}{2m_\Sigma^2} \\ &= 0.59 \pm 0.08\,(stat.) \pm 0.08\,(syst.)\,\mathrm{fm}^2. \end{aligned} \tag{6.3}$$

Table 6.1: Fit results for the Σ^- mean squared charge radius for different combinations of the lower (rows) and upper Q^2 limits (columns). Only statistical errors are shown. The weighted average of these fits agrees with the final result (6.1) which was computed from the combinations with the lowest statistical errors (top five rows of this table).

	$\langle r^2 \rangle$ [fm^2]		
Q^2_{min}	upper limits (in % of Q^2_{max}):		
[GeV$^2/c^2$]	60	65	70
0.030	0.576 ± 0.082	0.564 ± 0.077	0.573 ± 0.073
0.031	0.615 ± 0.086	0.599 ± 0.080	0.606 ± 0.076
0.032	0.627 ± 0.089	0.610 ± 0.083	0.617 ± 0.079
0.033	0.593 ± 0.092	0.579 ± 0.085	0.588 ± 0.081
0.034	0.606 ± 0.095	0.590 ± 0.088	0.600 ± 0.083
0.035	0.604 ± 0.098	0.588 ± 0.091	0.598 ± 0.086
0.036	0.635 ± 0.102	0.615 ± 0.094	0.625 ± 0.089
0.037	0.640 ± 0.106	0.619 ± 0.098	0.629 ± 0.092
0.038	0.635 ± 0.110	0.615 ± 0.101	0.626 ± 0.095
0.039	0.629 ± 0.113	0.609 ± 0.104	0.621 ± 0.097
0.040	0.633 ± 0.117	0.613 ± 0.107	0.625 ± 0.101
0.041	0.623 ± 0.121	0.603 ± 0.110	0.618 ± 0.103
0.042	0.643 ± 0.126	0.621 ± 0.114	0.635 ± 0.107
0.043	0.651 ± 0.131	0.628 ± 0.118	0.642 ± 0.111
0.044	0.651 ± 0.135	0.628 ± 0.122	0.643 ± 0.114
0.045	0.595 ± 0.138	0.579 ± 0.124	0.601 ± 0.116
0.046	0.539 ± 0.140	0.531 ± 0.126	0.560 ± 0.118
0.047	0.548 ± 0.145	0.540 ± 0.130	0.569 ± 0.121
0.048	0.547 ± 0.150	0.539 ± 0.135	0.570 ± 0.125
0.049	0.520 ± 0.154	0.518 ± 0.138	0.553 ± 0.128
0.050	0.507 ± 0.159	0.508 ± 0.142	0.546 ± 0.132

6.2 Discussion

6.2.1 Comparison to other hadrons and theoretical predictions

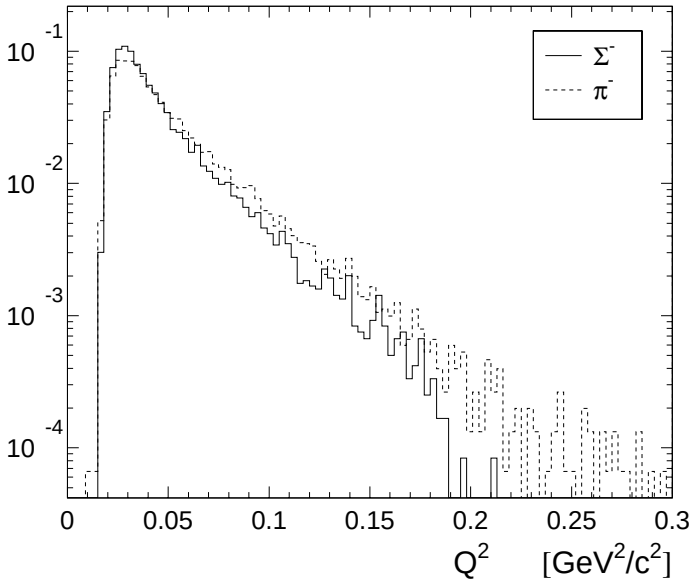

Figure 6.2: Q^2 distribution (normalized to the integral) of the final Σ^- sample (solid line) compared to the final π^- sample (dashed line) from [79].

The π^- charge radius extracted from SELEX hadron–electron elastic scattering data [79] in an analysis similar to the one described here equals

$$\langle r^2 \rangle_\pi^{\mathrm{SELEX}} = 0.45 \pm 0.03\,(stat.) \pm 0.07\,(syst.)\,\mathrm{fm}^2 \tag{6.4}$$

which is in agreement with the most accurate measurement so far [19] of

$$\langle r^2 \rangle_\pi = 0.44 \pm 0.01\,\mathrm{fm}^2. \tag{6.5}$$

This result indicates that there is no significant systematic offset of SELEX data to other experiments.

The statistical and systematic errors do not allow a definitive answer to the question whether the Σ^- has a smaller or larger charge radius than the proton. Since the results from different analyses of the proton radius are not in very good

Table 6.2: Mean squared radii for the proton from different experiments and analysis methods compared to the Σ^- radius.

$\langle r^2 \rangle$ [fm^2]	approach
0.67 ± 0.02	*ep* scattering, dipole fit [16]
0.74 ± 0.02	*ep* scattering, low-Q^2 fit[14]
0.72 ± 0.01	*ep* scattering, dispersion analysis [80]
0.79 ± 0.03	from Lamb shift [17]
0.60 ± 0.11	Σ^- (stat. and syst. errors combined)

agreement with each other (6.2), this issue would be best decided by a determination of the proton radius from SELEX data.

Out of the theoretical models listed in Table 2.1 on page 7, significant deviations from the SELEX result are found for the Skyrme model prediction of $\langle r^2 \rangle = 1.21\,\mathrm{fm}^2$ (5σ) and the vector dominance model prediction of $\langle r^2 \rangle = 0.34\,\mathrm{fm}^2$ (2.5σ). All other predictions are within the 2σ range (Fig. 6.3).

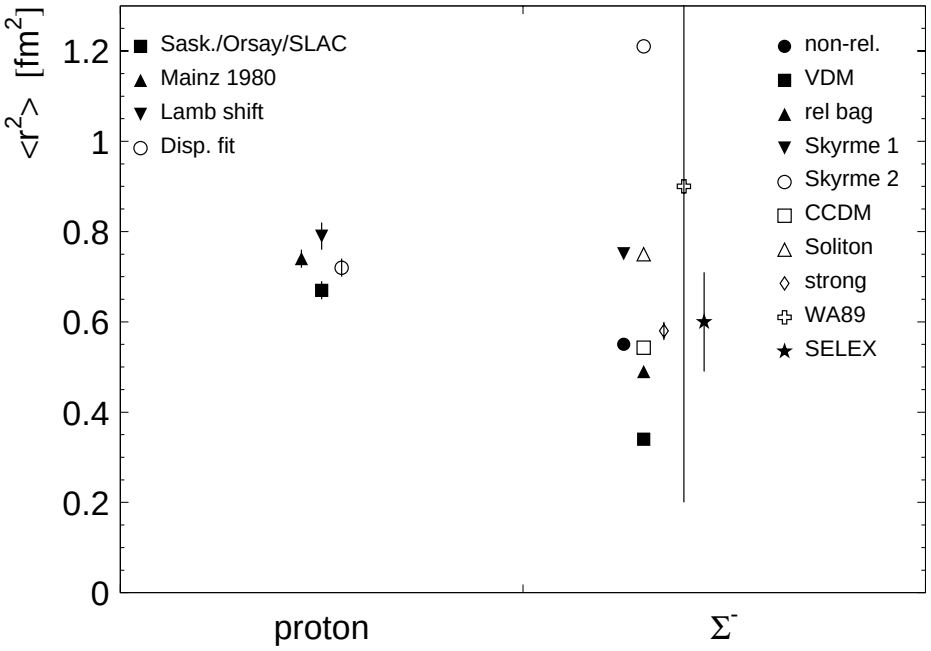

Figure 6.3: The Σ^- charge radius compared to various results for the proton radius as listed in Table 6.2 and theoretical predictions for the Σ^- charge radius. The predictions for Σ^- refer to the models listed in Table 2.1 on page 7: *non-rel.*: non-relativistic quark model, *VDM*: vector dominance model, *rel bag*: relativistic bag model (all three values from [1]), *Skyrme 1*: Skyrme model [10], *Skyrme 2*: Skyrme model [11], *CCDM*: Chiral color dielectric model [12], *Soliton*: Soliton model [13]. – *strong*: strong interaction radius [1], *WA89*: result of the WA89 measurement. *SELEX*: this measurement.

6.2.2 Possibilities for improvement

Out of the 11,967 events in the final sample, only 7864 were actually used for the fit. Further acceptance studies may lead to a realistic modeling of the correction for $Q^2 < 0.03$ GeV$^2/c^2$ so that the fit can cover the complete sample.

The final sample itself can be enhanced by a combination of various improvements of the reconstruction and analysis software as listed below. A sample size of 18,000 seems realistic; correct identification of Σ^- decays upstream of M2 could alredy enhance the sample by a factor of 1.5.

All improvements taken together, a statistical error of 0.05 fm^2 could be achieved.

Beam particle identification

The systematic error due to BTRD inefficiency can be reduced in part by requiring the Σ^- to be identified by its decay. A substantial fraction of misidentified Σ^- are expected to be Ξ^-, which can be distinguished from Σ^- by means of the kink angle distribution [81]

$$\Xi^- \rightarrow \Lambda\pi^-$$

or by recontructing the full decay of the Ξ^-: the Λ decays to 64 % to

$$\Lambda \rightarrow p\pi^-$$

in which case the decay vertex needs to be reconstructed. This requires a larger effective decay volume, i.e. the downstream part of the M2 spectrometer and the M3 spectrometer. The vector drift chambers and M3 chambers are essential in this case.

Electron identification

The fraction of π^- which are identified as electrons in the ETRD becomes significant at momenta above 120 GeV/c (Fig. 3.15 on page 40). All electrons from Σ^--electron scattering which pass through the ETRD should hit one of the lead glass calorimeters Photon 2 or 3. The ratio of energy deposited in the calorimeter to the momentum measured in the magnets can be used to distinguish electrons from other charged particles. The corresponding calorimeter elements have to be identified by tracing the particle trajectory into the detector. Again, this requires the M2 and M3 drift chambers.

Low-momentum electrons which pass only through a fraction of the ETRD planes are likely to be misidentified (cf. section 5.3.3). This class of events could be recovered by scaling the number of ETRD clusters required for electron identification with the number of planes traversed by the particle in question.

Momentum resolution

Poor momentum resolution for high-momentum tracks was the most serious constraint for this analysis. The trajectory of a scattered Σ^-, which usually has more than 450 GeV/c momentum before it decays, is bent by less than 4 mrad in the M1 and M2 magnets. The resolution of the M2 PWCs which have 2mm wire spacing is not sufficient in this case. The LASD system with 15 μm resolution per plane which provides the necessary information was not yet included in the momentum calculation due to a combination of problems related to alignment and track linking in the M1/M2 spectrometers.

Q^2 determination

Given adequate momentum resolution for the scattered Σ^-, Q^2 can be determined using all five measured variables $\vec{p}_\Sigma, \vec{p}_e{}', \vec{p}_\Sigma{}', \theta_e, \theta_\Sigma$ and equations (2.14), (2.15), (2.16) , and (2.17) (page 12) simultaneously.

The radiative losses of the electron can be accounted for by fitting Q^2 to the process

$$\Sigma^- e \to \Sigma^{-\prime} e' \gamma$$

where γ stands for the the combination of all radiative losses.

7

Conclusion

The objective of this investigation is the measurement of the Σ^- charge radius.

The SELEX (E781) experiment generated a 600 GeV/c Σ^-/π^- beam from the 800 GeV/c proton beam delivered by the Fermilab Tevatron. The main purpose of the experiment being charm physics, a special trigger for hadron-electron scattering was developed and implemented in the framework of the SELEX trigger. The trigger decision was based on an event topology given by two negative-charge particles which was determined by the combination of an interaction counter directly downstream of the target and a hodoscope downstream of two analyzing magnets. The interaction counter was tested at CERN and integrated into the SELEX trigger setup. It consisted of a fast logic capable of delivering a multiplicity estimate calculated from the pulse heights of two scintillation counters in less than 100 nanoseconds. This was necessary to achieve a substantial rejection factor at an early stage in the SELEX trigger. At a typical beam rate of 0.5 MHz the hadron-electron trigger had an average rate of 150 Hz.

Out of 215 million candidates recorded until September 1997, a sample of 12,000 Σ^--electron elastic scattering events was extracted after various stages of background reduction. The selection criteria included reconstruction of the vertex and identification of both Σ^- and electron. Σ^- which decayed upstream of the tracking detectors used for this analysis were rejected. Beam and scattered Σ^- and electron tracks were required to be coplanar and match the appropriate relations of two-body kinematics.

The four-momentum transfer squared Q^2 was calculated from the beam momentum and the electron scattering angle. Acceptance and resolutions were studied with Monte Carlo calculations and led to an estimated Q^2 resolution of 1.5 %.

A one-parameter maximum likelihood fit of the differential cross section $d\sigma/dQ^2$ to a selected part of the Q^2 distribution was performed to obtain the mean squared

charge radius:

$$\langle r^2 \rangle = 0.60 \pm 0.08\,(stat.) \pm 0.08\,(syst.)\,\mathrm{fm}^2.$$

The Q^2 range of the fit contained 7864 events and was selected by requiring the acceptance function to be independent of Q^2. Therefore no corrections were applied to this data sample. The total systematic error was evaluated by varying the upper and lower Q^2 limits of the fit. Those Q^2 intervals which showed no significant dependence on their boundaries coincided with the Q^2-independent part of the acceptance function.

The result of the analysis acts as proof that the Σ^- charge radius can be determined from the data taken with the SELEX experiment. Further analysis efforts using improved reconstruction code and a detailed acceptance correction will be able to achieve a measurement at the 10 % error level.

List of Tables

2.1 Charge and strong interaction radii and theoretical predictions . . 7
2.2 Experimental values of hadronic charge radii. 8
2.3 SELEX beam particles and their Q^2_{max} at 650 GeV/c 13

3.1 The SELEX targets 28
3.2 Average composition of lead glass in Photon detectors 43
3.3 Specifications of the SELEX lead glass calorimeters. 43
3.4 Specifications of the hodoscopes 44

4.1 Strip1 and final cut yields for different trigger versions 52
4.2 Technical specifications of the interaction counter. 61

5.1 Effective target parameters 64
5.2 The different stages of data reduction 66

6.1 Fit results for the Σ^- mean squared charge radius 95
6.2 Mean squared radii for the proton 97

List of Figures

2.1 Kinematics of Σ^--electron elastic scattering 10
2.2 Kinematic relations for Σ^--electron scattering 11
2.3 Σ^--electron scattering in the center of mass system. 12
2.4 Differential cross section for Σ^--electron elastic scattering 14
2.5 The total form factor squared 16
2.6 The differential cross section for different radii 17

3.1 The SU(4) multiplets of baryons 20
3.2 Schematic diagram of the SELEX layout 26
3.3 Schematic drawing of the main detector groups 26
3.4 The SELEX beam and vertex spectrometer 27
3.5 M1 spectrometer and upstream part of M2 spectrometer. 29
3.6 Downstream part of the M2 spectrometer 30
3.7 The M3 spectrometer 30
3.8 The hyperon channel 31
3.9 Schematic drawing of a silicon microstrip detector 33
3.10 Beam momentum and multiplicity distributions. 34
3.11 Vertex spectrometer layout 35
3.12 Schematic view of a double-sided silicon detector 36
3.13 The Vector Drift Chambers 37
3.14 BTRD discrimination of π^- against heavier beam particles 39
3.15 ETRD efficiency 40
3.16 ETRD cluster sum for electrons and pions 40
3.17 Čerenkov angle vs. momentum 41
3.18 Principal idea of a RICH 42

4.1 SELEX trigger and DAQ 46
4.2 Event topology of the h-e trigger 47
4.3 M2 total PWC hits vs. M2 track segments 49
4.4 A typical event 51
4.5 Average h-e trigger rate vs. run number 54

4.6 Trigger efficiency evaluation for different versions 55
4.7 Example background event 56
4.8 Counting multiplicity with a scintillator 57
4.9 Multiplicity separation efficiencies for the interaction counter . . . 59
4.10 Interaction Counter logic diagram 60

5.1 Material in the target region 64
5.2 Coplanarity check for two-prong vertices 68
5.3 Momentum and elasticity distributions of the final data sample . . 69
5.4 Bremsstrahlung losses 71
5.5 Electron scattering angle versus momentum 72
5.6 Angular correlation before and after kinematics cut 73
5.7 Effect of the final cuts on the Q^2/Q^2_{max} distribution 74
5.8 Angular correlation for π^-- and Σ^--electron scattering 75
5.9 Effect of selected cuts on the vertex resolution. 75
5.10 Ambiguity of the differential cross section when both mean squared radius and beam momentum are free parameters 77
5.11 Momentum, angular, and Q^2 resolutions 80
5.12 Errors of electron momentum determination 81
5.13 Monte Carlo study of the error assigned to the electron momentum 81
5.14 Q^2 dependence of various cuts 83
5.15 Monte Carlo study of trigger efficiency 84
5.16 The acceptance function 85
5.17 Statistical spread of fit results 87
5.18 Dependence of fit results on the Q^2 range 88
5.19 Dependence of fit results on the lower Q^2 limit 90

6.1 Q^2 and Q^2/Q^2_{max} distribution of the final sample 93
6.2 Q^2 distributions of the final Σ^- and π^- samples 96
6.3 The Σ^- charge radius compared to theoretical predictions 98

Bibliography

[1] B. Povh and J. Hüfner, Phys Lett B **245**, 653 (1990).

[2] R. Hofstadter, Rev Mod Phys **28** (1956).

[3] Y. Alexandrov et al., The high-intensity hyperon beam at CERN, preprint CERN-SL-97-60 EA, submitted to Nucl Inst and Meth A, CERN, 1997.

[4] J. Lach, Hyperons: insights into baryon structures, preprint FERMILAB-CONF-91/200, Fermilab, 1991.

[5] M. Adamovich et al., First observation of Σ^--e scattering in the hyperon beam experiment WA89 at CERN, preprint in preparation, CERN, 1998.

[6] Povh, Rith, Scholz, and Zetsche, *Teilchen und Kerne*, Springer Verlag, fourth edition, 1996.

[7] B. Povh, Nucl Phys A **532**, 133c (1991).

[8] M. Buenérd, The hyperon charge and matter form factors, preprint PPE-92-016, CERN, 1992.

[9] B. Povh and J. Hüfner, Phys Rev Lett **58**, 1612 (1987).

[10] J. Kunz, P. Mulders, and G. Miller, Phys Lett B **255**, 11 (1991).

[11] N. Park and H. Weigel, Nucl Phys A **541**, 453 (1992).

[12] S. Sahu, Mod. Phys. Lett. A **10**, 2103 (1995).

[13] H. Kim, A. Blotz, M. Polyakov, and K. Goeke, Phys Rev D **53** (1996), 4013-4029.

[14] G. Simon, C. Schmitt, F. Borkowski, and V. Walther, Nucl Phys A **333**, 381 (1980).

[15] L. Hand, D. Miller, and R. Wilson, Rev Mod Phys **35**, 335 (1963).

[16] J. Murphy, Y. Shin, and D. Skopik, Phys Rev C **9**, 2125 (1974).

[17] T. Udem et al., Phys Rev Lett **79**, 2646 (1997).

[18] S. Kopecky, P. Riehs, J. Harvey, and N. Hill, Phys Rev Lett **74**, 2427 (1995).

[19] S. Amendolia et al., Nucl Phys B **277**, 186 (1986).

[20] S. Amendolia et al., Phys Lett B **178** (1986).

[21] W. Molzon et al., Phys Rev Lett **41**, 1213 (1978).

[22] F. Borkowski, G. Simon, V. Walther, and R. Wendling, Nucl Phys B **93**, 461 (1975).

[23] L. Koester, W. Nistler, and W. Waschkowski, Phys Rev Lett **36**, 1021 (1976).

[24] G. Adylov et al., Nucl Phys B **128**, 461 (1977).

[25] E. Dally et al., Phys Rev Lett **39**, 1176 (1977).

[26] E. Dally et al., Phys Rev Lett **45**, 232 (1980).

[27] E. Dally et al., Phys Rev Lett **48**, 375 (1982).

[28] M. Heidrich, *Entwicklung eines Übergangsstrahlungszählers basierend auf Gasmikrostreifendetektoren zur ersten Untersuchung von $\Sigma^- - e^-$ Streuung am Hyperonenstrahl des CERN*, Dissertation, MPI f. Kernphysik / Univ. Heidelberg, 1996.

[29] M. Rosenbluth, Phys Rev **79**, 615 (1950).

[30] K. Königsmann, S. Paul, and B. Povh, Electromagnetic radii of hyperons using SELEX, H-Note 574, SELEX Internal Report, 1994.

[31] G. Källén, *Elementary Particle Physics*, chapter 8, Addison-Wesley, 1964.

[32] R. Sachs, Phys Rev **126**, 2256 (1962).

[33] J. Russ et al., A proposal to construct SELEX, Proposal P781, Fermilab, 1987.

[34] S. Biagi et al., Phys. Lett B **122**, 455 (1983).

[35] M. Adamovich et al., Phys Lett B **358**, 151 (1995).

[36] Particle Data Group, Phys Rev D **54** (1996).

[37] J. Russ, Charm baryon physics – present and future, H-Note 695, SELEX Internal Report, 1994, Invited talk at Charm2000 Meeting at Fermilab.

[38] P. Cooper, J. Grunhaus, and J. Russ, Search for doubly charmed baryons using 600 GeV/c hyperon and pion beams, H-Note 718, SELEX Internal Report, 1994.

[39] A. Donnachie and P. Landshoff, Phys Lett B **296**, 227 (1992).

[40] U. Dersch, Memorandum for the measurement of total Σ^--nucleon cross sections at SELEX, 1997, *(unpublished)*.

[41] S. Biagi et al., Nucl Phys B **186**, 1 (1981).

[42] H. Primakoff, Phys Rev **81**, 899 (1951).

[43] SELEX Beam Physics Group, Status of E781 beam physics, H-Note 784, SELEX Internal Report, 1997.

[44] Y. Antipov et al., Phys Lett B **121**, 445 (1983).

[45] M. Moinester and V. Steiner, Pion and kaon polarizabilities and radiative transistions, in *Chiral Dynamics Workshop: Theory and Experiment, Mainz, Sept. 1997*, edited by A. Bernstein and T. Walcher, Springer Verlag, 1998, hep-ex/9801008.

[46] M. Moinester, Chiral anomaly tests, in *Proceedings of the Conference on Physics with GeV-Particle Beams, Jülich, Germany*, edited by H. Machner and K. Sistemich, World Scientific, 1994.

[47] Y. Antipov et al., Phys Rev D **36**, 21 (1987).

[48] M. Adamovich et al., Z. Phys A **350**, 379 (1995).

[49] H. Siebert, Nucl Phys B **21**, 183 (1991).

[50] H. Siebert, Nucl Phys B **21**, 270 (1991).

[51] S. Paul, Nucl Phys B **21** (1991).

[52] M. Moinester, D. Ashery, L. Landsberg, and H. Lipkin, Pentaquark search with energetic hadron beams, H-Note 708, SELEX Internal Report, 1994, presented at CHARM2000 Workshop, Fermilab / hep-ph/9407319.

[53] P. Mathew and J. Russ, Hyperon mass resolution studies, H-Note 795, SELEX Internal Report, 1997.

[54] A. Atamantchuk et al., Design and performance of the Fermilab E781 (SELEX) Hardware Scattering Trigger, preprint submitted to Elsevier Preprint, 1997.

[55] P. Mathew, *Construction and evaluation of a high resolution silicon microstrip tracking detector and utilization to determine interaction vertices*, PhD thesis, Dept. of Physics, Carnegie Mellon University, 1997.

[56] U. Dersch et al., The mechanical design of the large angle silicon detectors, H-Note 804, SELEX Internal Report, 1998.

[57] J. Simon, private communications.

[58] W. Leo, *Techniques for Nuclear and Particle Physics Experiments*, Springer Verlag, second edition, 1994.

[59] T. Lungov and L. Emediato, Vector drift chambers database, H-Note 779, SELEX Internal Report, 1997.

[60] P. Pogodin et al., Drift chambers of the M1 spectrometer: the detector, electronics, and software, H-Note 788, SELEX Internal Report, 1997.

[61] N. Bondar et al., E781 beam transition radiation detector, H-Note 746, SELEX Internal Report, 1995.

[62] V. Maleev et al., Description and test results for DPWC and TRD in E781, H-Note 747, SELEX Internal Report, 1995.

[63] N. Terentiev, private communications.

[64] J. Engelfried et al., The E781 (SELEX) RICH detector, Presented Paper from the 7th Pisa Meeting on Advanced Detectors, May 1997 FERMILAB-Conf-97/210-E E781, Fermilab, 1997.

[65] E. Segrè, *Nuclei and Particles*, Addison-Wesley Publishing Co., 2nd edition, 1977.

[66] A. Antonov, G. Dzyubenko, and M. Kubantsev, Geometry of the assembled E781 PHOTON 1,2 detectors, H-Note 748, SELEX Internal Report, 1995.

[67] G. Davidenko, M. Kubantsev, and V. Verebryusov, E781 Photon DBase, H-Note 767, SELEX Internal Report, 1996.

[68] J. Engelfried et al., The E781 trigger and data aquisition system, H-Note 643, SELEX Internal Report, 1995.

[69] A. Kulyavtsev et al., E781 hardware trigger preliminary design, H-Note 676, SELEX Internal Report, 1994.

[70] I. Eschrich et al., The hadron-electron elastic scattering trigger, H-Note 803, SELEX Internal Report, 1997.

[71] H. Krüger, *Multiplizitätstrennung mit dem Wechselwirkungszähler im* SELEX-*Experiment*, Diplomarbeit, MPI f. Kernphysik / Univ. Heidelberg, 1996.

[72] D. Meier, *Bau eines Wechselwirkungszählers für* SELEX, Diplomarbeit, MPI f. Kernphysik / Univ. Heidelberg, 1995.

[73] *Bicron Product Catalog*, Newbury, OH 44065-9677, U.S.A., 1990.

[74] *Technical Data Sheet, Hamamatsu R1450 Photomultiplier Tube*, San Jose, CA 95128, U.S.A.

[75] CAEN S.p.A., 55049 Viareggio, Italy, *CAEN C207 Technical Information Manual.*

[76] LeCroy Research Systems, *LeCroy 1996 LRS Catalog*, 1996.

[77] P. Mathew and J. Russ, Primary vertexing in the online filter, H-Note 796, SELEX Internal Report, 1997.

[78] L. Lyons, *Statistics for nuclear and particle physicists*, chapter 4, Cambridge University Press, 1986.

[79] K. Vorwalter, *Determination of the Pion Charge Radius with a Silicon Microstrip Detector System*, Dissertation, MPI f. Kernphysik / Univ. Heidelberg, 1998.

[80] P. Mergell, U. Meissner, and D. Drechsel, Nucl Phys A **596**, 367 (1996).

[81] S. Biagi et al., Z. Phys C **17**, 113 (1983).

Contributions to the experiment

I participated in the installation, commissioning, operation, and the analysis phase of SELEX .

Within the SELEX silicon group I was responsible for installation, operation, and maintenance of the remote-controlled power supply system for the large area silicon detectors (LASD). I wrote a software package which operated and monitored this system automatically throughout the operational period of the experiment. Prior to the installation at Fermilab, I took part in three test beam periods at CERN to debug various parts of the LASD system. I was involved in writing the online software package for the complete system of SELEX silicon detectors.

My second project was the design and implementation of a trigger for elastic hadron–electron scattering.

In the course of this project I took part in design, assembly, and test of the SELEX interaction counter. The interaction counter was developed by the MPI group and played a central role for all of the experiment's interaction triggers. I conducted a test beam period at CERN dedicated to tuning the setup for operation at SELEX conditions.

The implementation of the hadron–electron scattering trigger was completed at the end of the commissioning phase and the trigger ran successfully to the last day of data-taking. During this time I fulfilled shift duties and coordinated the continuous improvement of the trigger.

Managing the first stage processing of hadron–electron scattering data at Fermilab and the subsequent passes of processing in Heidelberg was my next project. I implemented the SELEX computing environment in Heidelberg and was in charge of code and data management. I developed software for the analysis of hadron–electron scattering data.

-SELEX-
Segmented Large-x Baryon Spectrometer

R.Edelstein, E.Gottschalk, S.Y.Jun, A.Kushnirenko, Dongning Mao, P.Mathew, M.Mattson, M.Procario, J.Russ, J.You
Carnegie-Mellon University, Pittsburgh, PA 15213

P. S. Cooper, J. Engelfried, J. Kilmer, S. Kwan, J. Lach, G. Oleynik, E. Ramberg, D. Skow, L. Stutte
Fermilab, Batavia, Illinois 60510

N.Akchurin, M.Aykac, M.Kaya, D.Magarrel, E.McCliment, K.Nelson, C.Newsom, Y.Onel, E.Ozel, S.Ozkorucuklu, P.Pogodin
University of Iowa, Iowa City, IA 52242

T. Ferbel, G. Ginther, C. Hammer, P. Slattery, M. Zielinski
University of Rochester, Rochester, NY 14627

C. Kenney, S. Parker
University of Hawaii, Honolulu, HI 96822

L.J.Dauwe
University of Michigan-Flint, Flint, MI 48502

V.Andreev, A.G.Atamantchouk, N.F.Bondar, V.L.Golovtsov, V.T.Grachev, A.V.Khanzadeev, V.T.Kim, L.M.Kochenda, A.G.Krivshich, N.P.Kuropatkin, V.P.Maleev, P.V.Neoustroev, S.Patrichev, B.Razmyslovich, V.M.Samsonov, V.Stepanov, M.Svoiski, N.K.Terentyev, L.N.Uvarov, A.A.Vorobyov
Petersburg Nuclear Physics Institute, St. Petersburg, Russia

M.Ya.Balatz, G.V.Davidenko, A.G.Dolgolenko, G.B.Dzyubenko, A.V.Evdokimov, A.D.Kamenskii, M.A.Kubantsev, V.S.Lakaev, V.Matveev, A.P.Nilov, V.A.Prutskoi, V.K.Semyatchkin, A.I.Sitnikov, V.S.Verebryusov, V.E.Vishnyakov
Institute of Theoretical and Experimental Physics, Moscow, Russia

Yu.M.Goncharenko, O.A.Grachev, V.P.Kubarovsky, A.I.Kulyavtzev, V.F.Kurshetsov, A.A.Kozhevnikov, L.G.Landsberg, V.V.Molchanov, V.A.Mukhin, S.B.Nurushev, A.N.Vasiliev, D.V.Vavilov, V.A.Victorov
Institute For High Energy Physics, Protvino, Russia

I. S. Filimonov, E. M. Leikin, A. V. Nemitkin, V. I. Rud
Moscow State University, Moscow, Russia

L. Emediato, C. Escobar, F. Garcia, P. Gouffon, T. Lungov, M. Srivastava, R. F. Zukanovich
University of São Paulo, Brazil

A.M.F.Endler
Centro Brasileiro de Pesquisas Fisicas, Rio de Janeiro, Brazil

M. Luksys
Universidade Federal da Paraiba, Paraiba, Brazil

Li Yunshan, Li Zhigang, Mao Chensheng, Zhao Wenheng, He Kangling, Zheng Shuchen, Mao Zhenlin
Institute of High Energy Physics, Beijing, PRC

S.L.McKenna, V.J.Smith
H. H. Wills Physics Laboratory, University of Bristol, BS8 1TL, United Kingdom

I.Giller, M.A.Moinester, A.Ocherashvili, V.Steiner
Tel Aviv University , Ramat Aviv, Israel

U.Dersch, I.Eschrich, I.Konorov, H.Krüger, S.Masciocchi, B.Povh, J.Simon, K.Vorwalter
Max-Planck-Institute for Nuclear Physics, Heidelberg, Germany

A.Bravar, D.Dreossi, A.Lamberto, A.Penzo, G.F.Rappazzo, P.Schiavon
University of Trieste and INFN, Trieste, Italy

M.Gaspero, M.Iori
University of Rome "La Sapienza" and INFN , Rome, Italy

A.Morelos
Instituto de Fisica, Universidad Autonoma de San Luis Potosi, San Luis Potosi, Mexico

Erhan Gülmez
Bogazici University, Istanbul, Turkey

Spokesperson: **J. Russ**

Acknowledgements

I am indebted to Prof. Bogdan Povh for providing me with the opportunity to work on this exciting project, for his patience being my supervisor, and for solving both major and minor problems in an uncomplicated manner.

For their support and the magnificent times we have shared at Fermilab, CERN, Heidelberg, and elsewhere in the world I want to thank the living proof that good teamwork means both fun and success – the MPI SELEX group members of then and now: Dirk Meier, Emrullah Durucan, Gala Konorova, Henning Krüger, Igor Konorov, Jürgen Simon, Jürgen Zimmer, Klaus Vorwalter, Roland Werding, Silvia Masciocchi, and Uwe Dersch.

I would like to thank all members of the SELEX collaboration for their efforts. For many fruitful discussions I am especially grateful to Alex Kulyavtsev, Prof. Antonio Morelos, Prof. Charles Newsom, Eric Ramberg, Prof. James Russ, Jianming You, Joe Lach, Jürgen Engelfried, Mark Mattson, Prof. Mike Procario, Prof. Murray Moinester, Prof. Nikolai Terentiev, Peter Cooper, Prakash Mathew, Sasha Kushnirenko, Valery Kubarovsky, Victor Molchanov, Victor Steiner, and Vincent Smith. Frank Pearsall and Dave Northacker provided invaluable technical support.

I want to express my appreciation for maintaining the productive and friendly atmosphere at the Max Planck Institute in Heidelberg to Andreas Mücklich, Antje Brüll, Prof. Boris Kopeliovich, Christian Busch, Christian Büscher, Claudia Schröder, Douglas Jansen, Erik Volk, Eva Wittmann, Fabio Metlica, Frank Dropmann, Heiko Neeb, Irina Potashnikova, Priv.-Doz. Josef Pochodzalla, Prof. Kay Königsmann, Michael Zavertyaev, Nicolas Keller, Oliver Thilmann, Peter Fauland, Philipp Geiger, Ralf Todenhagen, Thomas Nunnemann, Thomas Wilhelm, Tina Schati, and Wieland Hoprich.

I am obliged to the WA89 group at CERN for sharing their facilities and making me feel welcome. I especially enjoyed the cooperation with Prof. Hans-Wolfgang Siebert, Lars Schmitt, Matthias Heidrich, Prof. Stephan Paul, Walter Brückner, Thomas Haller, and Ulrich Müller.

A very special thank-you for their unconditional support at all times goes to my parents and my friends, especially Karen.